SANDIA REPORT

SAND2013-10063
Unlimited Release
Printed November 2013

Computational Mechanics for Heterogeneous Materials

Jeremy B. Lechman, Andrew Baczewski, Stephen Bond, William Erikson, Richard Lehoucq, Lisa Mondy, David Noble, Flint Pierce, Christine Roberts, Frank van Swol, Cole Yarrington

Prepared by
Sandia National Laboratories
Albuquerque, New Mexico 87185 and Livermore, California 94550

Sandia National Laboratories is a multi-program laboratory managed and operated by Sandia Corporation, a wholly owned subsidiary of Lockheed Martin Corporation, for the U.S. Department of Energy's National Nuclear Security Administration under contract DE-AC04-94AL85000.

Sandia National Laboratories

Issued by Sandia National Laboratories, operated for the United States Department of Energy by Sandia Corporation.

Available to DOE and DOE contractors from
U.S. Department of Energy
Office of Scientific and Technical Information
P.O. Box 62
Oak Ridge, TN 37831

Telephone: (865) 576-8401
Facsimile: (865) 576-5728
E-Mail: reports@adonis.osti.gov
Online ordering: http://www.osti.gov/bridge

Available to the public from
U.S. Department of Commerce
National Technical Information Service
5285 Port Royal Rd
Springfield, VA 22161

Telephone: (800) 553-6847
Facsimile: (703) 605-6900
E-Mail: orders@ntis.fedworld.gov
Online ordering: http://www.ntis.gov/help/ordermethods.asp?loc=7-4-0#online

SAND2013-10063
Unlimited Release
Printed November 2013

Computational Mechanics for Heterogeneous Materials

Jeremy B. Lechman, Andrew Baczewski, Stephen Bond, William Erikson,
Richard Lehoucq, Lisa Mondy, David Noble, Flint Pierce,
Christine Roberts, Frank van Swol, Cole Yarrington

Abstract

The subject of this work is the development of models for the numerical simulation of matter, momentum, and energy balance in heterogeneous materials. These are materials that consist of multiple phases or species or that are structured on some (perhaps many) scale(s). By computational mechanics we mean to refer generally to the standard type of modeling that is done at the level of macroscopic balance laws (mass, momentum, energy). We will refer to the flow or flux of these quantities in a generalized sense as transport. At issue here are the forms of the governing equations in these complex materials which are potentially strongly inhomogeneous below some correlation length scale and are yet homogeneous on larger length scales. The question then becomes one of how to model this behavior and what are the proper multi-scale equations to capture the transport mechanisms across scales. To address this we look to the area of generalized stochastic process that underlie the transport processes in homogeneous materials. The archetypal example being the relationship between a random walk or Brownian motion stochastic processes and the associated Fokker-Planck or diffusion equation. Here we are interested in how this classical setting changes when inhomogeneities or correlations in structure are introduced into the problem. Aspects of non-classical behavior need to be addressed, such as non-Fickian behavior of the mean-squared-displacement (MSD) and non-Gaussian behavior of the underlying probability distribution of jumps. We present an experimental technique and apparatus built to investigate some of these issues. We also discuss diffusive processes in inhomogeneous systems, and the role of the chemical potential in diffusion of hard spheres is considered. Also, the relevance to liquid metal solutions is considered. Finally we present an example of how inhomogeneities in material microstructure introduce fluctuations at the meso-scale for a thermal conduction problem. These fluctuations due to random microstructures also provide a means of characterizing the aleatory uncertainty in material properties at the mesoscale.

Contents

Appendix

List of Figures

List of Tables

Chapter 1

Introduction

A homogeneous system is uniform in composition and kind (genus) which, in the case of the distribution of matter, implies a constant density $\rho(x,t) = \rho$; there is no spatial or temporal variation in the density. Under appropriate boundary and initial conditions for momentum and energy balance we can have no flow or heat flux (on average, $u(x,t) = 0$, $T(x,t) = T$) into (or within) the system along with the constant density profile, in which case the system can be described in terms of equilibrium thermodynamics. Yet, even in this case, a constant density is achieved only in the thermodynamic limit, $V \to \infty$. Below this limit, the density can be seen to fluctuate consistent with the macroscopic boundary conditions. The Law of Large Numbers (ignoring any correlations within the system) would give an approximate size of the density fluctuations as $V^{-1/2}$, where V is the volume. When the system is large the fluctuations can be ignored. However, when V is small, or V_{el} is small, where V_{el} is the volume of a typical element in a discretization of the governing equations, fluctuations can be significant. In fact, it is these fluctuations that can be expected to lead to fluxes which drive diffusive mixing of matter in simple fluids even in the case of no average (macroscopic) flow or composition gradient.

These thermodynamic fluctuations [1, 115] point to a role for mathematical models based on stochastic processes in the description of transport in materials [3, **?**]. Diffusion is the archetypal example. These classical models have been hugely successful in simple materials and in well defined limits where complexities in the material structure (e.g., correlations) can be ignored, since classical models are based on assumptions of statistical independence and Gaussian probability distributions. In fact, diffusion-like models have, in turn, been proposed as models of how fluctuations in macroscopic thermodynamic variables in simple systems converge to the homogeneous thermodynamic limit. For complex (inhomogeneous, heterogeneous) systems the question of homogenization is an open challenge.

One source of difficulty in complex-structured materials is what effect correlations in the material have on the approach to an asymptotic homogeneous limit. Conversely, it can be asked what effect inhomogeneities have on the local value of the field of interest relative to the macroscopic, homogeneous response. If correlations are long-range and inhomogeneities associated with them are significant then assumptions of "smoothly" varying fields and scale separation can breakdown on the scale of the discretization of the governing equations, or the form of the equations to be solved may not be appropriate to the size of the system simulated. In other words, we want to explore fluctuations inherent in the so-called stochastic volume

element (finite-sized volume element) to discern a theoretical structure that is amenable to mathematical models and experimental measurements to inform the models. In addition, for multi-scale models, it is expected that propagation of the correlations across scales is critical to physical fidelity. Finally, we note that stability of fluctuations is also relevant to emergent phenomena [4].

The subject of this work is the development of models for the numerical simulation of matter, momentum, and energy balance in heterogeneous materials. These are materials that consist of multiple phases or species or that are structured on some (perhaps many) scale(s). By computational mechanics we mean to refer generally to the standard type of modeling that is done at the level of macroscopic balance laws (mass, momentum, energy). We will refer to the flow or flux of these quantities in a generalized sense as transport. At issue here are the forms of the governing equations in these complex materials which are potentially strongly inhomogeneous below some correlation length scale and are yet homogeneous on larger length scales. The question then becomes one of how to model this behavior and what are the proper multi-scale equations to capture the transport mechanisms across scales. To address this we look to the area of generalized stochastic process that underlie the transport processes in homogeneous materials. The archetypal example being the relationship between and random walk or Brownian motion stochastic processes and the associated Fokker-Planck or diffusion equation. Here we are interested in how this classical setting changes when inhomogeneities or correlations in structure are introduced into the problem. At first sight we need to address non-classical behavior such as non-Fickian behavior of the mean-squared-displacement (MSD) and non-Gaussian behavior of the underlying probability distribution of jumps. In general, it appears we would like a theory of fluctuations in nonequilibrium systems that takes into account correlations on across various scales as well as instabilities.

Further background and discussion of related issues is found in the following sections.

Background on Diffusion and Stochastic Processes

Here we summarize a number of issues related to models for diffusion and anomalous diffusion. The concept of diffusion is based upon the observation that "stuff" spreads from higher to lower concentrations even when no average flow is present; examples include mass and energy. The hallmark of a classical diffusive process $X(t)$ is the linear scaling of the mean squared displacement with time, or so-called Fickian diffusion. Anomalous diffusion occurs when the scaling is not linear with time. More precisely, $X(t)$ is *asymptotically*

$$\left\{ \begin{array}{c} \text{subdiffusive} \\ \text{diffusive} \\ \text{superdiffusive} \end{array} \right\} \quad \text{if} \quad \lim_{t\to\infty} \frac{\mathbb{E}\big(X^2(t)\big)}{t} = \left\{ \begin{array}{c} 0 \\ D \\ \infty \end{array} \right\}$$

where D defines the diffusion coefficient and $\mathbb{E}\big(\,\cdot\,\big)$ denotes the expectation, or mean. The statistical physics literature denotes expectation and variance by using the notation $\langle X(t)\rangle$ and $\langle X^2(t)\rangle$, respectively. Here we emphasize that many discussions in the literature (e.g.,

??) focus on the asymptotic behavior to assess the potentially anomalous nature of the process and spend relatively little effort characterizing the approach to the asymptotic limit. The approach to the asymptotic limit turns out to be relevant to our work.

Somewhat less formally, $X(t)$ is

$$\left\{ \begin{array}{c} \text{subdiffusive} \\ \text{diffusive} \\ \text{superdiffusive} \end{array} \right\} \quad \text{when} \quad \mathbb{E}\big(X^2(t)\big) \propto t^\sigma \quad \text{where} \quad \sigma \left\{ \begin{array}{c} < \\ = \\ > \end{array} \right\} 1.$$

The remainder of this Chapter reviews classical diffusion and its departure to anomalous diffusion. Our presentation is pedagogical, attempting an informal unification, via random walks and its generalizations. An excellent textbook, from an applied probabilistic perspective is due to Gardiner [5]. An excellent introduction to random walks, from a statistical physics perspective is due to Klafter and Sokolov [6]. A concise, well-written book serving as an introduction to a modern mathematical approach to random walks is due to Lawler [7]. An excellent bridge between the statistical physics and classical probabilistic approaches to random walks is given by Meerschaert and Sikorskii [8]. Both books [6] and [8] also introduce and develop the notion of fractional derivatives, at the heart of many anomalous diffusion approaches. The book by Applebaum [9] is a well-regarded introduction to a modern approach for Lévy process. These five books cover nearly every topic, except on Markov chains, considered in this short overview. An excellent book on Markov chains is that by Norris [10].

Diffusion

The canonical diffusive process ($\sigma = 1$) is Brownian motion, an example of a Wiener process. A physical perspective associates Brownian motion with two fundamental models, the first supposes randomness whereas the second is deterministic. A bit more precisely, we have

- **microscopic**: Brownian motion

$$X_t = \sqrt{2D}\, W_t, \qquad X_0 \in \mathbb{R}^n$$

  where W_t is a Wiener stochastic process, and the

- **macroscopic**: Expectation of the process X_t conditioned upon $X_0 = x \in \mathbb{R}^n$ evolves according to

$$\left\{ \begin{array}{l} \dfrac{\partial}{\partial t}\mathbb{E}^x\big(u_0(X_t)\big) = \nabla \cdot 2D \nabla\, \mathbb{E}^x\big(u_0(X_t)\big) \\ \quad \mathbb{E}^x\big(u_0(X_0)\big) = u_0(x), \end{array} \right.$$

  where u_0 is a probability density, representing the initial condition, and $\mathbb{E}^x\big(u_0(X_t)\big) = \mathbb{E}\big(u_0(X_t)|X_0 = x\big)$.

The distinction between the two models is crucial. The former model represents what occurs, or data, assumed to fluctuate in a random fashion. The latter model explains that the mean of the process satisfies a partial differential equation—the diffusion equation, i.e.,

$$\frac{\partial}{\partial t}u(x,t) = \nabla \cdot 2D\nabla\, u(x,t),$$

where

$$u(x,t) = \frac{1}{\sqrt{2D\pi t}}\int_{\mathbb{R}^n} e^{-\frac{(x-y)\cdot(x-y)}{2Dt}}\, u_0(y)\, dy = \mathbb{E}^x\big(u_0(X_t)\big).$$

In words, the function u is the probability density for the evolution of the initial condition u_0. This evolution represents the expectation for the process $u_0(X_t)$ when starting at the point x. The special choice of $u_0(x) = \delta(x)$, the Dirac measure or delta function, grants that

$$u(x,t) = \frac{1}{\sqrt{2D\pi t}} e^{-\frac{x\cdot x}{2Dt}} = \mathbb{E}^x\big(\delta(X_t)\big)$$

so that the probability that $X_t \in \Omega$ is given by

$$\mathbb{P}\big(X_t \in \Omega\big) = \frac{1}{\sqrt{2D\pi t}}\int_\Omega e^{-\frac{x\cdot x}{2Dt}}\, dx$$

or a normal random variable with mean 0 and variance $2Dt$. Again, it is emphasized that this canonical model is "scale-free" in that sense that the Brownian motion applies for arbitrary temporal resolution. In complex, heterogeneous materials there are potentially many length and time scales over which the stochastic processes related to transport may have anomalous forms. This issue will present itself in following Chapters.

Random walk

A Wiener process $W(t)$ satisfies the following three technical conditions:

1. $W(0) = 0$, the sample-path (the trajectory as a function of time t) is continuous
2. $W(t)$ is of mean and variance 0 and t, respectively.
3. independent increments, i.e., $W(t_2) - W(t_1)$ is independent of $W(t_4) - W(t_3)$ for $t_4 \geq t_3$, $t_2 \geq t_1$.

Intuitively, we can think of a Wiener process as the limit of a simple random walk on a lattice. For instance, in one-dimension, a walker jumps from a point on the lattice to either its leftmost or rightmost neighbor with probability $\frac{1}{2}$. More formally, denote the discrete random process specifying the distance of the walk by X such that

$$X(n) = X(n-1) + S \in \{-n\Delta x, (-n+1)\Delta x, \ldots, n\Delta x\} \tag{1.0.1}$$

where S is a discrete random variable that assumes the values $\pm\Delta x$ with probability

$$\mathbb{P}(S = \Delta x) = \mathbb{P}(S = -\Delta x) = 1/2$$

with mean and variance

$$\mathbb{E}(S) = 0 \quad \text{and} \quad \mathbb{E}(S^2) - \big(\mathbb{E}(S)\big)^2 = \mathbb{E}(S^2) = (\Delta x)^2.$$

The mean and variance of $X(n)$ are then

$$\begin{aligned} \mathbb{E}\big(X(n)\big) &= n\mathbb{E}(S) = 0 \\ \mathbb{E}\big(X^2(n)\big) &= (\Delta x)^2 n = \frac{(\Delta x)^2}{\Delta t} t \end{aligned}$$

where we assume that $n\Delta t = t$.

If the (fixed) distance Δx between lattice points and (fixed) time Δt between steps satisfies the scaling relationship

$$\big(\Delta x\big)^2 = D\,\Delta t, \tag{1.0.2}$$

then the central limit theorem implies that the probability at time $t = n\,\Delta t$ for the location of the walker is approximately given by a normally distributed random variable with zero mean and variance $\sqrt{n/2}$. In particular, since a simple random walk represents a binomial distribution, application of the Laplace–De Moivre theorem grants that

$$P(a \le X(n) \le b) \to \frac{1}{\sqrt{2\pi D t}} \int_a^b e^{-\frac{x^2}{2Dt}}\, dx \qquad n \to \infty,$$

where the scaling relationship (1.0.2) is assumed. A Wiener process is then this limiting random walk, e.g., when $n \to \infty$, or equivalently, $\Delta t \to 0$ so that discrete time is replaced by time over an interval. This limiting walk is continuous but not differentiable, an important analytical distinction. Loosely, if the trajectory $X(0), X(\Delta x), \cdots, X(n\Delta x)$ consisting of jumps of size $\pm\Delta x$ is connected by linear segments, then as $\Delta x \to 0$ there are an increasing number of points of continuity where the derivative is not defined.

The random walk model provides a powerful way to understand the transition from a discretely defined process (fixed step-lengths at fixed times) to a process where the step-length can take on a continuum of values. The central limit theorem then provides a rigorous basis for the transition from a discrete time to a continuum process.

In the above simple random walk, the fixed step-length of $\pm\Delta x$ represents a discrete random variable given by S. A more general random walk is realized by replacing S with a random variable taking on a continuum of values with the restriction that its variance is finite, e.g., a uniform or normal random variable. Because the variance is assumed finite, we may still invoke the central limit theorem for the limiting walk, a Wiener process. However, the sequence of random walks can differ substantially among all random variables replacing S with finite variance.

Stochastic differential equation

The random walk model is powerful but a continuous time process is only obtained in the limit. An alternate model, continuous in time is given by the Itô stochastic differential equation (SDE)

$$dX(t) = f(X(t))\,dt + g(X(t))\,dW(t),$$

where this is notation for

$$X(t) = X(0) + \int_0^t f(X(s))\,ds + \int_0^t g(X(t))\,dW(t),$$

where $W(t)$ is a Wiener process. The subtlety is understanding the stochastic differential dW. Let $0 = t_0 < t_1 < \cdots < t_{m+1} = t$; then

$$\int_0^t g\big(X(t)\big)\,dW := \lim_{m\to\infty} \sum_{i=0}^{m} g\big(X(t_i)\big)\big(W(t_{i+1}) - W(t_i)\big)$$

defines a stochastic integral so that we may think of dW as the increments $W(t_{i+1}) - W(t_i)$. The link with a random walk is obtained when the SDE is discretized, $f = 0, g = 1$ and (1.0.1) is rewritten as

$$X(n) = X(0) + \sum_{i=1}^{n} \big(X(i) - X(i-1)\big).$$

Markov jump process

In contrast to the random walk $X(n)$, a discrete-time process, consider the continuous-time process governed by the integro-differential equation

$$u_t(x,t) = \int_{\mathbb{R}^n} \gamma(y,x)\,u(y,t)\,\mathrm{d}y - \int_{\mathbb{R}^n} \gamma(x,y)\,u(x,t)\,\mathrm{d}y, \tag{1.0.3}$$

a nonlocal analogue of the diffusion equation, also known as a chemical or Markov master equation. The first integral gives the jump rate $\gamma(y,x)\,dx$ into dx from y given probability $u(y,t)\,dy$, the second integral gives the jump rate $\gamma(x,y)\,dy$ into dy from x given the probability $u(x,t)\,dx$. The difference in these two rates gives the rate of change for the probability $u(x,t)\,dx$. If the jump-rate is asymmetric, i.e., $\gamma(x,y) \neq \gamma(y,x)$, then the probability of the process jumping to x from y is distinct from the probability of the process jumping to y from x. If γ is symmetric, then we may rewrite (1.0.3) as

$$u_t(x,t) = \int_{\mathbb{R}^n} \big(u(y,t) - u(x,t)\big)\,\gamma(y,x)\,\mathrm{d}y.$$

The continuous-time process corresponding to (1.0.3) is a Markov jump process, a generalization of a continuous-time Markov chain over an uncountable (continuum) state-space. Loosely, replacing the integrals above with summations leads to a continuous-time Markov chain. This generalization explains the origin of the "jump" designation since a continuous-time Markov chain transitions from state to state by jumping.

CTRW

A continuous-time random walk (CTRW) generalizes the discrete time random walk. A CTRW can also be understood as continuous-time Markov chain where the wait-times between jumps, or steps, are no longer restricted to be exponentially distributed. Of particular relevance to transport in heterogeneous materials are CTRW models of diffusion in disordered materials [11, 12] and their relationship to generalized master equations [13] and so-called effective medium theories [14, 15].

Superdiffusion

A superdiffusive process can now be understood in one of three ways. The first is as the limit of a random walk where the random variable specifying the step-length is not of finite variance or even of finite mean. For example, consider when the random variable S is given by the Cauchy distribution.

The second way is to replace the Wiener increment for the SDE with one where the variance is not finite. This leads to a jump diffusion stochastic differential equation.

The third way in which to understand a superdiffusive process occurs when the jump measure behaves in an asymptotic fashion as

$$\gamma(x,y) \propto \frac{1}{|x-y|^{n+\alpha}}, \qquad 0 < \alpha < 2.$$

The jump measure is not integrable so that (1.0.3) is replaced by

$$u_t(x,t) = \int_{\mathbb{R}^n} \big(\gamma(y,x)\, u(y,t) - \gamma(x,y)\, u(x,t)\big)\, \mathrm{d}y \tag{1.0.4}$$

where, loosely, the density u must be sufficiently well-behaved to offset the non-integrability of γ.

Subdiffusion

A superdiffusive process can be understood as a CTRW where the wait-times between jumps are not of finite mean. The associated master equation generalizes (1.0.3) to

$$\int_0^\infty u(x,\tau)\phi(\tau - t)\, \mathrm{d}\tau = \int_{\mathbb{R}^n} \gamma(y,x)\, u(y,t)\, \mathrm{d}y - \int_{\mathbb{R}^n} \gamma(x,y)\, u(x,t)\, \mathrm{d}y \tag{1.0.5}$$

and when the mean of the wait-time density ϕ is undefined, the corresponding stochastic process is not Markovian. In words, the future of the process depends upon the current state and the history of the process. A Markov process is defined to have no dependence upon the

past. A stochastic differential equation approach is based upon fractional Brownian motion, however this approach is distinct from a CTRW perspective.

Our first attempt at this concerns introducing a time scale into the equations of motion for the stochastic process (the so-called Langevin equation) and revisiting what has been shown regarding the form of the diffusion equation for this case.

Overview of Chapters

In the following Chapters we will have opportunity to refer back to some of these standard notions in order to highlight areas in need to generalization.

In Chapter 2 we introduce equilibrium colloidal dynamics as the model system for considering generalizations (non-Fickian, non-Gaussian – anomalous) to standard macroscale models of transport in complex systems and the connections to underlying stochastic processes. We consider thermodynamic equilibrium and in a macroscopically homogeneous systems. However, the role of transient inhomogeneities in the structure is highlighted as relevant to the nonstationary (non-Fickian) and and correlated (non-Gaussian) nature of the processes. In Chapter 4 we examine an experimental technique built and tested to gain physical insight into these systems. Specifically, diffusing-wave spectroscopy is discussed.

In Chapter 3 we consider diffusive processes in inhomogeneous systems and the role of the chemical potential in diffusion of hard spheres is considered. Also, the relevance of this line of thought to liquid metal solutions is considered.

In Chapter 5 we show how inhomogeneities in material microstructure introduce fluctuations at the meso-scale that in some limits are reminiscent of thermodynamic fluctuations within otherwise macroscopically homogeneous thermodynamic systems. These fluctuations due to random microstructures also provide a means of characterizing the aleatory uncertainty in material properties at the mesoscale. Finally, Chapter 6 contains a summary and outlook for future work.

Chapter 2

Diffusion of Colloids

In this chapter we introduce equilibrium colloidal dynamics as the model system for considering generalizations of standard macroscale models of transport in complex systems and the connections to underlying stochastic processes. To begin, we discuss some aspects on non-interacting colloids (infinitely dilute limit) where the inertia of the colloids is not neglected. This introduces a time scale into the stochastic process – the momentum relaxation time. We will see that time scales can be bridged in the macroscopic equations of colloidal self-diffusion by recognizing the non-stationary nature of the microscopic stochastic process. In the dilute limit the "microscopic" equations of motion are uncoupled; the colloids uncorrelated. Going beyond self-diffusion in this limit we consider finite volume fractions of mono-disperse hard-spheres with a view toward the role correlations and transient inhomogeneities in structure play in an otherwise macroscopically homogeneous system. Of interest is the effect of correlations on the form of the macroscopic diffusion equation.

Dilute Limit and the Langevin Equation

As a model of the dynamics of dilute colloids, consider a system of N identical, interactionless particles of mass, m, following classical Langevin dynamics according to

$$\begin{aligned} \frac{d\mathbf{r}_i}{dt} &= \mathbf{v}_i \\ \frac{d\mathbf{v}_i}{dt} &= -\gamma\mathbf{v}_i + \frac{1}{m}\mathbf{E}_i(t), \end{aligned} \tag{2.0.1}$$

where $\gamma = \tau_B^{-1}$ with τ_B the momentum relaxation time, and $\mathbf{E}(t)$ is a random force with $\langle\mathbf{E}(t)\rangle = 0$ and $\langle\mathbf{E}(t)\mathbf{E}(t')\rangle = 2kTm\gamma\delta(t-t')$. A formal solution to this equation is well know (see, e.g., Risken [20] or Zwanzig [21]) to be given by

$$\mathbf{v}(t) = \mathbf{v}_0 e^{-t/\tau_B} + \frac{1}{m}\int_0^t e^{-(t-t')/\tau_B}\mathbf{E}(t')dt'. \tag{2.0.2}$$

Using this an analytic expression the velocity autocorrelation function can be obtained and integrated twice to get an expression for the mean-squared displacement (MSD) [20]

$$\langle \Delta\mathbf{r}^2\rangle(\Delta t) = 6\frac{kT}{m}\tau_B(\Delta t - \tau_B(1 - e^{-\Delta t/\tau_B})). \tag{2.0.3}$$

It should be noted that we have averaged over the initial distribution of velocities assuming a Maxwell-Boltzmann distribution to obtain Equation 2.0.3. This is because we want to focus on the non-stationarity of the process while considering the case of stationary increments, that is, Δr is a function of $\Delta t = t - t_0$ but not t. Hence, in the discussion to follow we will always consider the system to be well equilibrated or in the asymptotic stationary regime of the velocity distribution; that is, we consider the process to have run long enough to reach stationary velocity distribution – the Maxwell-Boltzmann distribution (also assumed to be the initial velocity distribution).

Although this result has been well known, it is worth pausing and reflecting on it at this point to see what it may have to tell us about developing multi-scale models of transport. Note, for short times we get MSD $\sim \Delta t^2$, or ballistic motion, while in the long-time limit MSD $\sim \Delta t$, as expected. It is convenient to characterize this behavior through the so-called Hurst parameter, H. Typically considered a constant, H has been used to characterize generalized stochastic process (e.g., fractional Brownian motion) [22, 23]. In contrast to previous uses, here H is a function of time (i.e., MSD $\sim t^{2H(\Delta t)}$), and $H = 1/2$, classical Brownian motion, only in the limit $\Delta t \to \infty$ (i.e., $\Delta t >> \tau_B$). This is an indication of nonstationarity of the process. We will return to this below. At this point we note that the Fokker-Planck equation in position space [24] corresponding to equations 2.0.1 admits scaling solutions through a change of time variable that allow one to obtain the standard $H = 1/2$ of classical diffusion in terms of the new time, τ_D (i.e., $\langle \Delta\mathbf{r}^2\rangle(\Delta t) \sim \tau_D^{2H}$ for $\tau_D \geq 0$ with $H = 1/2$). Note, the suggestion of a change of variables has also arisen in other contexts [25, 26].

To make the last point clear, we make specific the change of time variable. Define the new time variable τ_D as

$$\tau_D(\Delta t) = \frac{\langle \Delta\mathbf{r}^2\rangle(\Delta t)}{6\tau_B LT/m} = \tau_B(\Delta t/\tau_B - (1 - e^{-\Delta t/\tau_B})), \tag{2.0.4}$$

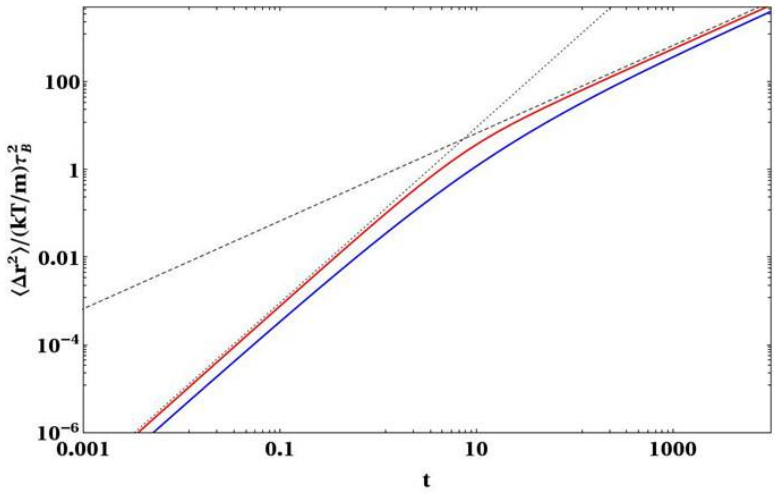

Figure 2.1. Plot of MSD as a function of time for system following Equations 2.0.3 (red line) and 2.0.39(blue line). Dashed line $\sim t^2$, dotted $\sim t$.

where, again, we have made explicit the dependence on $\Delta t = t - t_0$; t_0 is an arbitrary time origin assumed to be much larger than the time at which the process began, $t_0 >> t_{-\infty}$. We can take $t_{-\infty} = -\infty$. Then, we are free to choose $t_0 = 0$. As noted above, this is so since the jump process (Δr) is non-stationary with stationary increments, i.e., $r(t + \Delta t) - r(t)$ depends only on Δt and not t [26] after it has forgotten it's initial velocity, or if we began and remain the the stationary velocity distribution. That is, the moments of the distribution that characterize this process, in the well equilibrated limit, depend on elapsed time, or the time increment of an observation of the process, Δt and not the "absolute" time. This is the first indication of the role that "resolution" (i.e., Δt) plays in the transport of multi-scale systems (cf. [27]). The new time acts like a "metric" which tells us how to measure time. In real time, t, the MSD or average kinematics of the system, goes as the complicated function given in Equation 2.0.3. However, in "diffusive time" as measured by τ_D the MSD follows

$$\langle \Delta \mathbf{r}^2 \rangle(t) = 6 \left(\frac{kT}{m} \tau_B \right) \tau_D. \tag{2.0.5}$$

Hence, we can rewrite the complicated real-time dependence of the MSD as a function which is linear in our new time variable τ_D. This means that even ballistic motion, whose MSD is $\sim t^2$, or superdiffusive, can be thought of as $\sim \tau$ if time, τ, is measured as $\tau = t^2$. We also point out that the velocity autocorrelation function (VACF) can be found by $\langle \mathbf{v}(t)\mathbf{v}(t') \rangle = \frac{kT}{m} \frac{d^2 \tau_D(t-t')}{dt^2}$, and $D(t) = \frac{kT}{m} \tau_B \frac{d\tau_D(t)}{dt}$.

The convenience of this line of thought can be seen in a natural question to ask. What kind of distribution gives rise to the MSD of Equation 2.0.5? The simplest is the standard Gaussian propagator, which in one-dimensional form is

$$\rho(x,\tau_D) = \frac{1}{\sqrt{4\pi\frac{kT}{m}\tau_B\tau_D}}\exp\left(-\frac{x^2}{4\frac{kT}{m}\tau_B\tau_D}\right). \tag{2.0.6}$$

This "Gaussian" assumption has been discussed previously in other contexts [28] and will be the assessed in a later section. More generally, scaling forms of the probability density and their relation to nonstationary process with stationary or nonstationary increments have been discussed [26]. In [26] it was found that anomalous values of the Hurst parameter, $H \neq 1/2$, could be associated with uncorrelated processes with nonstationary increments; however, a change of time variable allows one to formally transform the process from nonstationary increments to stationary increments. Here there are no correlations (interactions) between walkers, but there is a correlation in the velocity of a given walker due the time it takes for a particle to "forget" its earlier velocity (inertia). This leads to a Hurst parameter, $H = f(\Delta t)$.

Now, $\rho(x,\tau_D)$ is the Green's function of

$$\frac{\partial\rho(x,\tau_D)}{\partial\tau_D} = \frac{kT}{m}\tau_B\nabla^2\rho(x,\tau_D), \tag{2.0.7}$$

for $\rho(x,0) = \delta(x)$ in an infinite domain. Using the chain rule we can re-write this as

$$\frac{\partial\rho(x,t)}{\partial t} = \frac{kT}{m}\tau_B(1-e^{-t/\tau_B})\nabla^2\rho(x,t), \tag{2.0.8}$$

We claim that this is an example of a type of "multi-scale" equation. This is the equation to solve, if one wants to account for the self-diffusion of dilute colloids containing the full effects of the microscopic dynamics. We note that this equation has been arrived at from more rigorous routes (see below and [24]). The preceding discussion has been merely heuristic and is illustrative of a broader set of issues. Indeed, most often the ballistic motion of colloids is at such a small time scale that it can be safely ignored and the classical diffusion equation can be used as a model of colloidal self-diffusion for times well above the momentum relaxation time scale. However, not all systems have a single time scale that is so conveniently ignored.

The question then arises as to when the classical diffusion equation is a good model for these multiple, competing or overlapping time/length scale systems.

To see how the previous considerations can be helpful one can consider what happens when one attempts to solve the diffusion equation on ever smaller length and time scales. This can be illustrated by referring to Figure 2.1. The dashed line of slope 1 on the log-log scale represents the MSD of classical Fickian diffusion. As Δt is decreased it can be seen to deviate from the actual MSD of the colloids whose dynamics follow the Langevin equation (red line). Again, this is well known, but what is not often recognized is that one can capture the full behavior of the colloids at the macroscopic level of description by writing Equation 2.0.6. Writing this equation allows one to "bridge" from the classical, ballistic motion scale below the momentum relaxation timescale to the macroscopic diffusive motion scale in one equation. We will discuss this further in the following. But first we show the relationship between Equation 2.0.6 and the telegrapher equation, which has been proposed as a model to capture small scale ballistic motion.

Connection to Telegrapher's Equation

An interesting connection arises between the above and the Telegrapher's or Cattaneo Equation and a diffusion equation with memory, which to our knowledge hasn't been pointed out explicitly in the literature. We start by integrating Equation 2.0.8 to obtain

$$\rho(x,t) = \rho(x,0) + 2\frac{kT}{m}\tau_B \int_0^t (1 - e^{-t'/\tau_B})\nabla^2\rho(x,t')dt'. \tag{2.0.9}$$

Now we make a subtle change to the first term in the integrand on the right-hand-side. We make the integral a convolution integral by making the change $e^{-t'/\tau_B} \rightarrow e^{-(t-t')/\tau_B}$. And we write

$$\rho(x,t) = \rho(x,0) + 2\frac{kT}{m}\tau_B \int_0^t (1 - e^{-(t-t')/\tau_B})\nabla^2\rho(x,t')dt'. \tag{2.0.10}$$

Taking the time derivative of 2.0.10, we have

$$\frac{\partial\rho(x,t)}{\partial t} = \frac{\partial\rho(x,0)}{\partial t} + 2\frac{kT}{m} \int_0^t (e^{-(t-t')/\tau_B})\nabla^2\rho(x,t')dt'. \tag{2.0.11}$$

If we take $\frac{\partial \rho(x,0)}{\partial t} = 0$ we obtain a diffusion equation with memory. In this case the memory kernel is a simple exponential decay. Equation 2.0.14 is well known [29] to be equivalent to

$$\tau_B \frac{\partial^2 \rho(x,t)}{\partial t^2} + \frac{\partial \rho(x,t)}{\partial t} = 2\frac{kT}{m}\tau_B \nabla^2 \rho(x,t'). \tag{2.0.12}$$

So, the telegrapher equation can be seen to be a special case of Equation 2.0.10 with initial condition $\frac{\partial \rho(x,0)}{\partial t} = 0$, which we emphasize is to be distinguished from Equation 2.0.9. One area of application where this has relevance is in nano-scale thermal transport [30] (see also [31]). Again, the issue in these systems is that the nature of thermal transport changes on "small enough" scales where both Equations 2.0.9 and 2.0.10 have been proposed [30] and [25]. Also, the telegrapher equation has been proposed as a model of diffusion which satisfies special relativity and the constancy of the speed of light [32].

In general, considering a general time convolution kernel $K(t-t')$, we can also write

$$\rho(x,t) = \rho(x,0) + D\int_0^t K(t-t')\nabla^2 \rho(x,t')dt', \tag{2.0.13}$$

which might be considered a diffusion relaxation equation, or the diffusion equation with memory

$$\frac{\partial \rho(x,t)}{\partial t} = D\int_0^t \frac{dK(t-t')}{dt}\nabla^2 \rho(x,t')dt'. \tag{2.0.14}$$

Again we have assumed $\frac{\partial \rho(x,0)}{\partial t} = 0$ and $K(0) = 0$. Finally, we note that if $K(t-t') \sim (t-t')^{\alpha-1}$, where $0 < \alpha \leq 1$, Equation 2.0.13 reduces to a Liouville-Riemann fractional integral equation. Care needs to be taken with Equation 2.0.14; however applying a fractional differential operator to both sides of the fractional relaxation equation will yield a fractional differential equation (cf. the fractional Fokker-Planck equation, e.g., [33]).

General Multi-scale Diffusion Equations

In previous sections we focused on a particular form of the history function, τ_D, and introduced a time or resolution (Δt) dependent Hurst parameter to characterize the Δt

dependence of the $MSD \sim \Delta t^{2H(\Delta t)}$. Specifically, the history function, derived from the (well equilibrated) Langevin dynamics of the colloids, lead to the analytic form given in Equation 2.0.4. In this section we consider more generic forms of the history function. In general we have

$$\frac{\partial \rho(x,t)}{\partial t} = \frac{kT}{m}\tau_B \frac{d\tau_D(t)}{dt}\nabla^2 \rho(x,t), \tag{2.0.15}$$

Again, the key constitutive relation being $\tau_D(t)$, which must have well defined $\frac{d\tau_D}{dt}$. Let's consider a few forms for τ_D to make explicit the general time dependence (recall time translation invariance allows us to choose $t_0 = 0$ so that $\Delta t = t$, but this should not obscure the fact that we are actually talking about an elapsed time from an arbitrary initial time) of the Hurst parameter, $H(t) = \frac{d\ln(\tau_D)}{d\ln(t)}$. For the system defined by Equations 2.0.1, $H(t) = \frac{t}{2\tau_D}\frac{d\tau_D}{dt} = (1 - e^{-t/\tau_B})t/2(t - \tau_B(1 - e^{-t/\tau_B}))$. Obviously, $H \to 1/2$ for $t \gg \tau_B$ as seen in Figure 2.2.

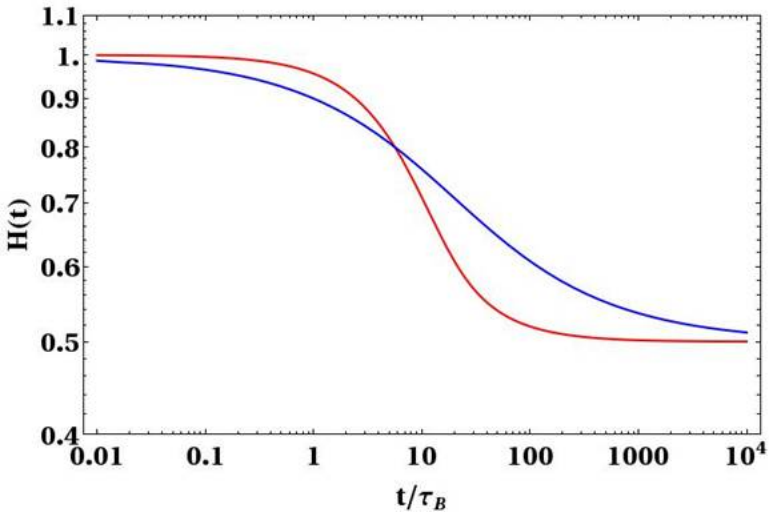

Figure 2.2. Plot of Hurst parameter as a function of time for system following Equations 2.0.1.

If $\tau_D = t$, Equation 2.0.18 reduces to the standard diffusion equation and we have classical, Fickian diffusion on all time scales; $H = 1/2$. There is however, another possibility. Note, if $\frac{d\tau_D}{dt} = \kappa = const.$ with κ a constant for all t, then we could have an (apparently) nonlinear Fokker-Planck Equation (nFPE) [34, 35]

$$\frac{\partial}{\partial t}\left[\rho(x,t)\right]^{\mu} = \frac{kT}{m}\tau_B \nabla^2 \left[\rho(x,t)\right]^{\nu}, \tag{2.0.16}$$

where $MSD \sim \tau_D^{2\mu/(\mu+\nu)}$. In general, we could have [**?**]

$$\frac{1}{\kappa} = \begin{cases} \frac{1}{2}\left[\left(\frac{1-q}{2\pi}\right)^{1/2} \frac{\Gamma((5-3q)/2(1-q))}{\Gamma((2-q)/(1-q))}\right]^{2(q-1)/(3-q)} & \text{if } q < 1, \\ \frac{1}{2} & \text{if } q = 1, \\ \frac{1}{2}\left[\left(\frac{q-1}{2\pi}\right)^{1/2} \frac{\Gamma(1/(1-q))}{\Gamma((3-q)/2(1-q))}\right]^{2(q-1)/(3-q)} & \text{if } 1 < q \leq 3, \end{cases} \tag{2.0.17}$$

where, $q = 1 + \mu - \nu$, in previous sections $q = 1$ since $\mu = \nu$. This allows us to make contact with nonlinear Fokker-Plank equations [**?**].

Lastly, if $\frac{d\tau_D}{dt} = Ht^{2H-1}$ we have the equation

$$\frac{\partial \rho(x,t)}{\partial t} = \frac{kT}{m}\tau_B (Ht^{2H-1}) \nabla^2 \rho(x,t), \tag{2.0.18}$$

In this case connection can be made to Fokker-Planck equations derived from fractional Brownian motion (fBm) [36]. But also note in [26] an explanation of a number of these models (particularly Equation 2.0.16) with scaling solutions is given in terms of non-stationary stochastic process with stationary or non-stationary increments [26]. The relationship between the analysis of [26] and [36] is unclear at this point.

In all the above cases, $\tau_D(t)$ is interpreted as the history function of the system, which describes the temporal structure of events/interactions in a random system in terms of the average kinematics or MSD. It describes the Fickian or non-Fickian (anomalous) nature of the system

Routes to the Dilute Multi-scale Diffusion Equation

Our first approach follows [37] and is related to the derivation of dynamic density functional theory relevant to inhomogeneous systems (see Chapter 3). Most approaches to this derivation now start with the Kramers-Klein equation [**?**] to account for colloid inertia, but a modified approach using a contracted description in configuration space (see below) is also possible within the context of the earlier derivation. We start with the continuity equation

$$\frac{\partial}{\partial t}P(\mathbf{r}^N,t) = -\sum_{i=1}^{N}\nabla_i\cdot\left[\mathbf{v}_i P(\mathbf{r}^N,t)\right]. \tag{2.0.19}$$

Recall, for a colloid under a time dependent force $\mathbf{F}_i(t)$ the velocity of the colloid is

$$\mathbf{v}_i(t) = \mathbf{v}_{0,i}e^{-t/\tau_B} + \frac{1}{m}\int_0^t e^{-(t-t')/\tau_B}\mathbf{F}_i(t')dt'. \tag{2.0.20}$$

Following [**?**] we take the force to be the equilibrium force driving the colloids $\mathbf{F}_i = -kT\nabla_i \ln\left[P(\mathbf{r}^N)\right] - \nabla_i V(\mathbf{r}^N)$, where $V(\mathbf{r}^N)$ is the potential energy due to particle interactions and external potentials. Plugging this into Equation 2.0.20 and taking $\mathbf{v}_0 = 0$ we obtain

$$\mathbf{v}_i(t) = \frac{\tau_B}{m}(1-e^{-t/\tau_B})\mathbf{F}_i. \tag{2.0.21}$$

We now insert this into Equation 2.0.19 make replacing the equilibrium probability density $P(\mathbf{r}^N)$ with the nonequilibrium one $P(\mathbf{r}^N,t)$ and $V(\mathbf{r}^N)$ by $V(\mathbf{r}^N,t)$ [**?**] to give

$$\frac{\partial}{\partial t}P(\mathbf{r}^N,t) = \frac{\tau_B}{m}(1-e^{-t/\tau_B})\sum_{i=1}^{N}\nabla_i\cdot\left[kT\nabla_i\ln\left[P(\mathbf{r}^N)\right] + \nabla_i V(\mathbf{r}^N)P(\mathbf{r}^N,t)\right]. \tag{2.0.22}$$

Averaging over $\mathbf{r}^{N-1}$ degrees of freedom gives the one-body probability density

$$\begin{aligned}\frac{\partial\rho(\mathbf{r},t)}{\partial t} &= \frac{\tau_B}{m}(1-e^{-t/\tau_B})\nabla\cdot[\rho(\mathbf{r},t)\nabla\mu(\mathbf{r},t)] &(2.0.23)\\ &= \frac{\tau_B}{m}(1-e^{-t/\tau_B})\left[kT\nabla^2\rho(\mathbf{r},t) + \nabla\cdot(\rho(\mathbf{r},t)\nabla\mu^{ex}(\mathbf{r},t))\right], &(2.0.24)\end{aligned}$$

where the chemical potential $\mu = \mu^{id} + \mu^{ex}$ is separated into ideal and excess parts (cf. Equation 2.0.8 where interactions are absent $\mu^{ex} = 0$). This result is relevant particularly in inhomogeneous systems (see Chapter 3).

Following [24] it is also possible to show more rigorously in the limit of dilute, non-interacting or independent colloids that the diffusion equation we arrived at in Equation **??** is correct. First, we "contract" the description of the dynamics from phase space (position and velocity) to configuration space (position only) by writing the first of Equation 2.0.1 in terms of the formal solution of the second Equation in 2.0.1 (i.e., plug Equation 2.0.2 into the first of 2.0.1). In doing so we arrive at another linear Langevin equation for position.

$$\frac{d\mathbf{r}}{dt} = \mathbf{v}_0 e^{-t/\tau_B} + \frac{1}{m}\int_0^t e^{-(t-t')/\tau_B}\mathbf{E}(t')dt'. \tag{2.0.25}$$

It can be shown [24] that this equation has the corresponding Fokker-Planck equation

$$\frac{\partial\rho(x,t)}{\partial t} = (1 - e^{-t/\tau_B})\frac{kT}{m}\tau_B\nabla^2\rho(x,t), \tag{2.0.26}$$

where we have averaged over the Maxwell-Boltzmann distribution of initial velocities with $\langle\mathbf{v}_0\rangle = 0$. This can be rewritten as in Equation 2.0.7 by defining τ_D as in Equation 2.0.4. In the non-interacting limit the same approach can be taken for general $\tau_D(t)$ (e.g., see discussion of Generalized Langevin Equation below). And in that general case we have

$$\frac{\partial\rho(x,t)}{\partial t} = D(t)\nabla^2\rho(x,t), \tag{2.0.27}$$

where,

$$D(t) = \int_0^t \Gamma(t,t')dt', \tag{2.0.28}$$

and $\Gamma(t,t')$ is the modified force-force autocorrelation function with the initial velocity dependence incorporated into the regular force-force autocorrelation function [24]. Equation **??** is averaged over the distribution in initial Maxwell-Boltzmann velocities with zero average. Comparing Equations 2.0.7 with 2.0.27 and 2.0.28 suggests two ways of interpreting the complicated nonstationarity of the underlying processes. One is through a nonlinear time transformation as in 2.0.6 and the other by defining a time dependent diffusion coefficient as in Equation 2.0.28. The discussion to this point has relied implicitly on the Gaussian assumption of Equation 2.0.6. Before addressing this issue at the end of the next section we first relate the discuss how the preceding discussion relates to non-Markovian processes, in particle the so-called Generalized Langevin Equation.

Generalized Langevin Equation: Non-Markovian Processes

We can extend the discussion of the previous sections to encompass the broader class of non-Markovian or so-called Generalized Langevin Equations (GLE). A main contribution of this project is the addition of a package in the LAMMPS code that simulates these processes. Details on this have been reported elsewhere [38] and are contained in Appendix A for reference. For now, consider the case of a colloid in a solvent with a frequency or time-dependent viscosity. For example, the equation of motion of a sphere in an incompressible, Newtonian fluid has been shown by Basset and Boussinesq to be

$$(m_p + \frac{1}{2}m_f)\frac{d\mathbf{U}}{dt} + 6\pi\eta a \int_{-\infty}^{t} \frac{(t-t')^{-1/2}}{\Gamma(1/2)} \frac{d\mathbf{U}}{dt'} dt' + 6\pi\eta a \mathbf{U} = \mathbf{E}(t), \tag{2.0.29}$$

where $\mathbf{E}(t)$ is a time dependent force (e.g., fluctuating force due to thermal fluctuations of the fluid).

Equation 2.0.29 may also be written as

$$m^* \frac{d\mathbf{U}}{dt} + 6\pi\eta a \int_{-\infty}^{t} \frac{(t-t')^{-3/2}}{2\Gamma(1/2)} \mathbf{U} dt' + 6\pi\eta a \mathbf{U} = \mathbf{E}(t), \tag{2.0.30}$$

where $m^* = (m_p + \frac{1}{2}m_f)$. Equation 2.0.2 can be derived by inverse Laplace transform of the impulsive response of the sphere in a viscous fluid to find the memory kernel (see Felderhof [39] and Kupferman [40], also [41, 42]. Equation 2.0.2 can also be written as

$$m^* \frac{d\mathbf{U}}{dt} + 6\pi\eta a \int_{-\infty}^{t} \left(\frac{(t-t')^{-3/2}}{2\Gamma(1/2)} + \delta(t-t') \right) \mathbf{U}(t') dt' = \mathbf{E}(t), \tag{2.0.31}$$

where the memory kernel, $M(t)$, in the convolution integral of eqn. 2.0.31 is

$$M(t-t') = 6\pi\eta a \left(\frac{(t-t')^{-3/2}}{2\Gamma(1/2)} - \delta(t-t') \right) \tag{2.0.32}$$

If $\mathbf{E}(t)$ is to be a model for random force due to thermal fluctuations in the fluid we will need to define it. Ignoring the steady-state drag (second term in the memory kernel in Equation 2.0.32), assuming the random force to be (i) Gaussian; (ii) stationary; and (iii) self-similar, then we have a fractional Brownian motion (fBm) process, $dB_H(t)$, with Hurst parameter $H = 1/4$ (see Mandelbrot and van Ness [22], Kou [43], etc.). In this case, the force takes the form

$$\begin{aligned} \text{“}E(t) &= \sqrt{2\eta k_B T} dB_H/dt\text{”}, && (2.0.33)\\ < E(t) > &= 0, && (2.0.34)\\ < E(t)E(t') > &= 2\eta k_B T M(t-t'), && (2.0.35) \end{aligned}$$

where the double quotes imply an informal physics notation. Note in the model given in Equation 2.0.31 there is also the Dirac delta term in the memory kernel. From fluctuation dissipation this requires two random forces - one for the Stokes drag term ($6\pi\eta a\mathbf{U}$ acquired after integrating the second term of the memory kernel over the delta function) leading to a standard Wiener process or Brownian motion and one for the first term in the convolution integral giving an fBm.

The solution to Equation. 2.0.31 for $\mathbf{E}(t) = \mathbf{S}\delta(t)$, where $\mathbf{S}$ is the total momentum transferred to the fluid, is [39]

$$\mathbf{U}(t) = \frac{\mathbf{S}}{m^*}\frac{1}{2(q_1 - q_2)}\left[q_1 E_{1/2}\left(-t/\tau_1\right) - q_2 E_{1/2}\left(-t/\tau_2\right)\right], \tag{2.0.36}$$

where $q_{1,2} = \frac{1}{2Za}(1 \pm \sqrt{1-4Z})$, $Z = \frac{2m_p + m_f}{9m_f}$, $\tau_{1,2} = q_{1,2}\nu$, and

$$E_{\alpha,\beta}(y) = \sum_{k=0}^{\infty} \frac{y^k}{\Gamma(\beta + \alpha k)} \tag{2.0.37}$$

is the Mittag-Leffler function. We use the common, simplified notation $E_{1,\beta}(y) = E_\beta(y)$. In general we have for $U_0 = 0$

$$\mathbf{U}(t) = \int_0^t \mathbf{E}(t)\frac{1}{2(q_1 - q_2)}\left[q_1 E_{1/2}\left(-(t-t')/\tau_1\right) - q_2 E_{1/2}\left(-(t-t')/\tau_2\right)\right] dt'. \tag{2.0.38}$$

From Equation 2.0.36 we can form the velocity autocorrelation function and integrate twice to get the MSD. Which is

$$\langle \Delta \mathbf{r}^2 \rangle(t) = 6\frac{kT}{m}\tau_B^2 \left(\frac{1}{2(q_1 - q_2)} \left[q_1 E_{1/2}^{(2)}\left(-t/\tau_1\right) - q_2 E_{1/2}^{(2)}\left(-t/\tau_2\right) \right] \right), \tag{2.0.39}$$

where $E_{\alpha,\beta}^{(k)}(y) = \frac{d^k}{dy^k} E_{\alpha,\beta}(y)$. Which gives a history function

$$\tau_{D_{tBd}} = \tau_B \left(\frac{1}{2(q_1 - q_2)} \left[q_1 E_{1/2}^{(2)}\left(-t/\tau_1\right) - q_2 E_{1/2}^{(2)}\left(-t/\tau_2\right) \right] \right), \tag{2.0.40}$$

Equations 2.0.3 and 2.0.39 are compared in Figure 2.1. Note, again, at long times Equation 2.0.40 gives $\tau_{D_{tBd}} \sim t$ and at short times $\tau_{D_{tBd}} \sim t^2$ but the relaxation occurs over a longer time range.

Finally, we write

$$\frac{d\tau_{D_{tBd}}}{dt} = D(t)/(kT/m) = \tau_B \left(\frac{1}{2(q_1 - q_2)} \left[q_1 E_{1/2}^{(3)}\left(-t/\tau_1\right) - q_2 E_{1/2}^{(3)}\left(-t/\tau_2\right) \right] \right), \tag{2.0.41}$$

In addition to the incompressible Newtonian solvent an analytical form for a compressible Newtonian solvent can be found in the literature [44]. This is plotted with the previous two in Figure 2.3. While the previous two cases were examples of a single time scale but differing forms of relaxation, the addition of compressibility introduces a second (finite) time scale for sound propagation. Note for the parameters chosen in this plot the effect of the compressibility occurs at several orders of magnitude above the momentum relaxation time. A number of other memory kernels can be found in the literature for various kinds of visco-elastic solvents and even for high Reynolds and Mach number flow [**?**].

Simulation Hard-sphere Colloids at Finite Volume Fraction: Interactions and Correlations

In this section we report on the simulation of hard-sphere-like colloids. We use the colloid package in LAMMPS with the integrated Lennard-Jones potential for colloid-colloid

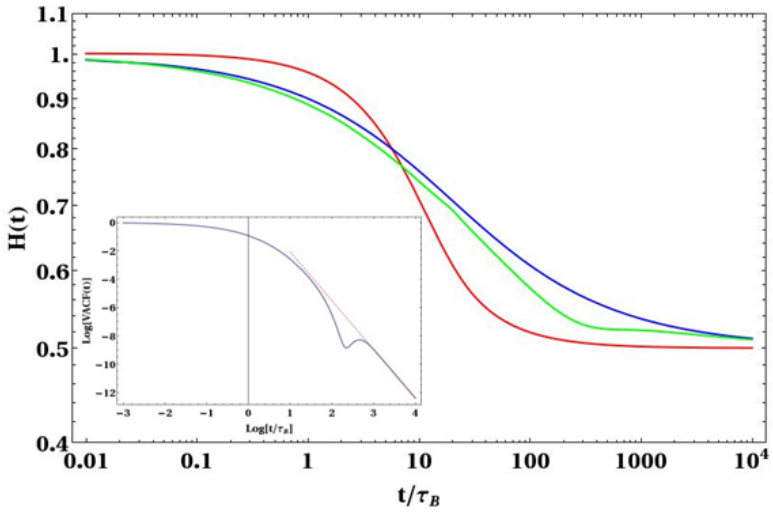

Figure 2.3. Hurst parameter for steady-state and transient incompressible Newtonian fluid as well as transient, compressible Newtonian fluid (red, blue, and green lines, respectively).

interactions and a volume fraction dependent, mean-field correction to Stokes drag to model the hydrodynamic forces on the colloids (note, we ignore lubrication forces here). The details of the model a reported elsewhere [46, 47, 48]. We compare results with inertia both included (as in previous section) and excluded (as in traditional Brownian Dynamics). The equations of motion solved (for the inertial case) are

$$\begin{aligned} \frac{d\mathbf{r}_i}{dt} &= \mathbf{v}_i \\ \frac{d\mathbf{v}_i}{dt} &= -\gamma(1+2.16\phi)\mathbf{v}_i + \sum_{i\neq j}\mathbf{F}_{ij}(r_{ij}) + \frac{1}{m}\mathbf{E}_i(t), \end{aligned} \tag{2.0.42}$$

where, again, $\langle E_i(t)\rangle = 0$ and $\langle E_i(t)E_j(t')\rangle = 2kTm\gamma(1+2.16\phi)\delta(t-t')$. In Equation 2.0.42, ϕ is the volume fraction and the factor $(1+2.16\phi)$ is the volume fraction dependent, mean-field correction to Stokes drag on particle i due to the many-body, long-range hydrodynamic forces on i from all the other colloids. Also, $\mathbf{F}_{ij}(r_ij)$ is the relative position dependent force on colloid i due to all other particles. This is modeled as an integrated Lennard-Jones potential cut off as the minimum [47] leading to effective hard-sphere interactions. This term is responsible for the interactions, transient inhomogeneity and associated correlations that develop and decay during the equilibrium simulation. We initialize the particle positions randomly at a low volume fraction and initial velocities drawn from a Maxwell-Boltzmann distribution; subsequently, shrink the simulation domain until the desired volume fraction is

obtained while advancing the dynamics according to Equations 2.0.42, etc.. Once the desired volume fraction is obtained, we then equilibrated further until the asymptotic, stationary increment limit is reached (we relax any effects or memory of the box shrinking), and then we collect data.

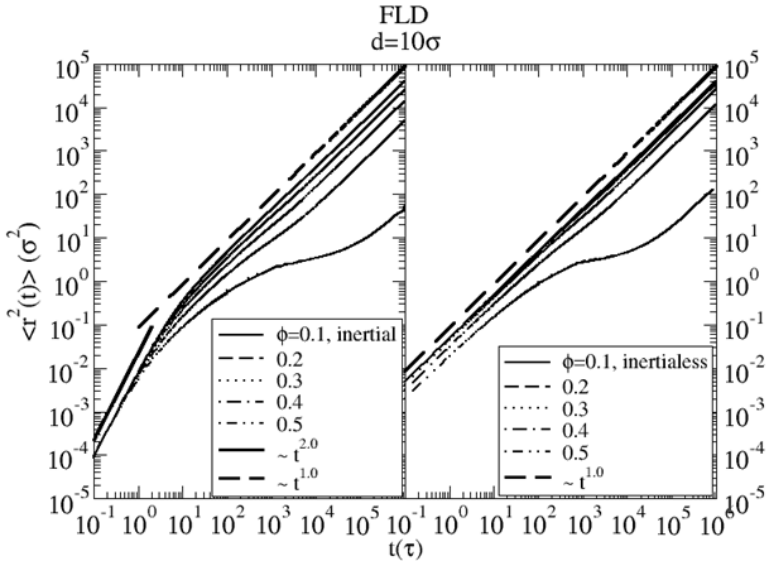

Figure 2.4. MSD as a function of time for various volume fractions of colloids following Equations 2.0.42. Left panel for simulation including inertia; right panel ignoring inertia.

Examples of the MSD data for various volume fractions are presented in Figure 2.4. Both inertial and inertialess simulation data are presented. In the inertial case, which will be the focus of the remainder, two timescales can be seen in the data. The first is the momentum relaxation time scale discussed in preceding section. The second is a correlation time scale related to the colloid-colloid interactions. At a given volume fraction there is a characteristic average spacing between particles roughly uniformly distributed in the simulation domain. Depending on the physical parameters (viscosity of solvent, mass of colloid, temperature) the colloids explore their local environment independent of one another. However, after some time they begin to interact and become correlated (in fact, anticorrelated as they bounce way from each other) during that time. After a longer time they move away from and become decorrelated again. This transient inhomogeneity and relaxation is sometimes referred to as the "caging" effect of the local structure.

From the MSD data, an effective, time-dependent diffusion coefficient can be obtained by taking the time derivative of the MSD data at various times. This is plotted in Figure 2.5. Again, in this Figure, both the inertial and inertialess data are shown; the main difference being at early time where the inertial data falls off as t^{-1}.

From Figure 2.7 the early-time and late-time diffusion coefficients can be found. Due to the relatively low viscosity of this fluid, we do not see a very pronounced early-time plateau in

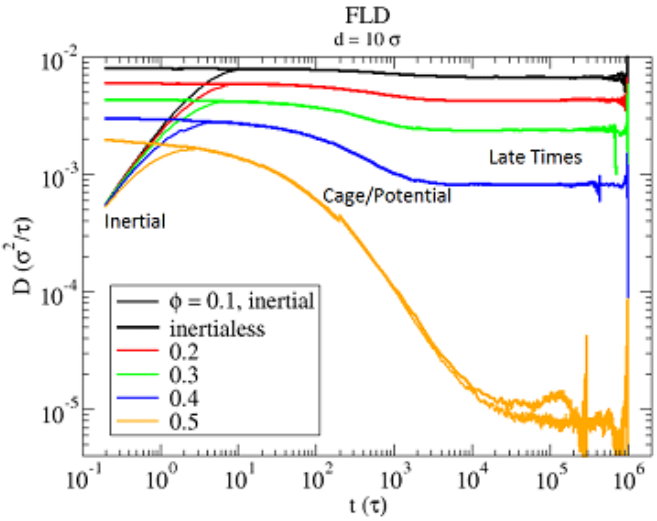

Figure 2.5. Diffusion coefficient as a function of time for hard sphere colloids at various volume fractions.

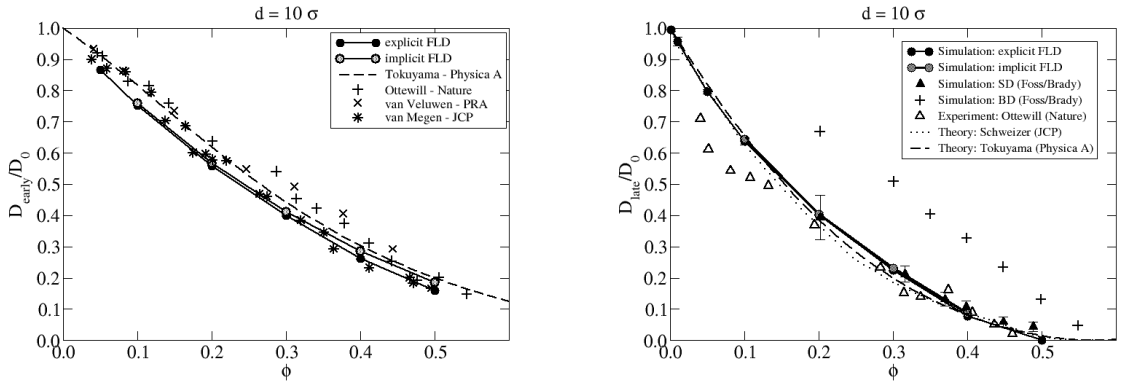

(a) **(b)**

Figure 2.6. Early (left) and late (right) time diffusion coefficients as a function of volume fraction from Figure 2.5 also compared to other simulation and experimental results.

the diffusion as a function of time. Hence, we define the maximum of $D(t)$ as the early-time diffusion coefficient and the value of $D(t)$ at the late-time plateau as the late-time diffusion coefficient. These are plotted in Figure 2.8. Also, shown in Figure 2.8 are results from other simulation, theory, and experimental work on hard-sphere colloids that demonstrate verification and validation of these simulations in terms of the relevant diffusion coefficients.

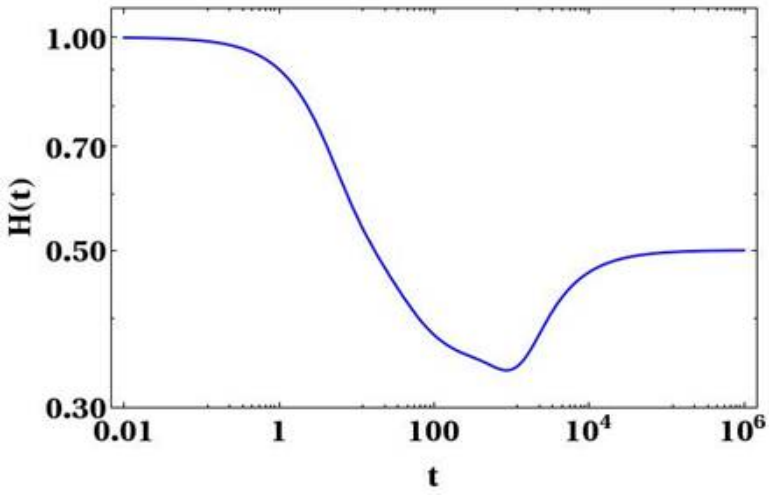

Figure 2.7. Hurst parameter as a function of time for colloids at 40% volume fraction.

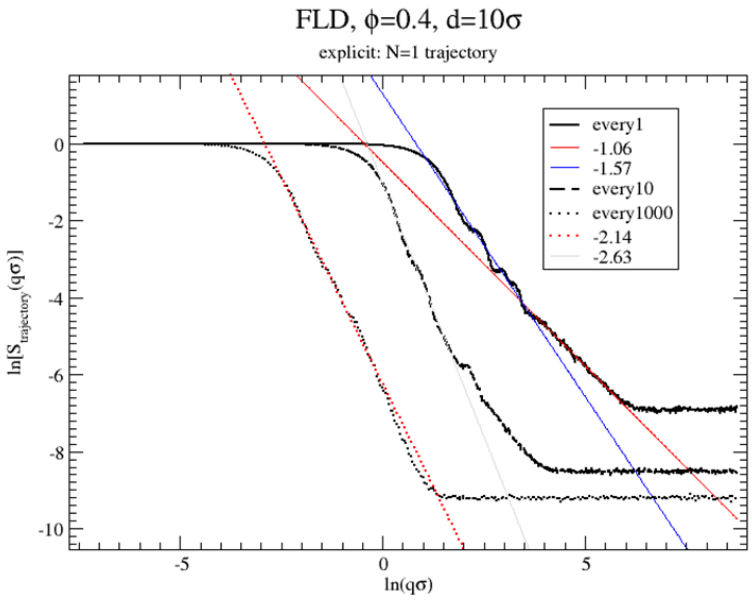

Figure 2.8. Simulated light scattering of a colloid trajectory at 40% volume fraction (averaged over several trajectories).

In addition to $D(t)$, one can also find the Hurst parameter $H(t)$ from these systems by taking the logarithmic derivative with respect to logarithm of time. This is plotted in Figure 2.9. In this instance, $MSD\ t^{2H(t)}$ so we can write $\tau_D(t) = t^{2H(t)}$. Here, we see the ballistic

early time ($H = 1$) and diffusive late time ($H = 1/2$). In between, a subdiffusive ($H < 1/2$) regime can be seen where correlations are relevant.

It is interesting to note that there is a relationship between the Hurst parameter and the fractal dimension of a trajectory $d_f = 1/H$ [23]. Again, in this case, we see a Hurst parameter and fractal dimension which are resolution or scale dependent. Figure 2.8 shows the results of numerical "light scattering" on colloidal trajectories. To make this plot a cluster of points was created based on the location of a colloid at various times (particle positions are taken every 1, 10, or 1000 time steps to create the cloud/cluster of points), then a scattering simulation is performed. This is analogous to a light scattering experiment where the static structure factor, $S(q)$, is determined. This is the quantity plotted in Figure 2.8 which gives an indication the spatial structure of the cluster of points created from the position of a colloid as a function of time (averaged over several colloids to improve the statistics). Several time ranges of the trajectory are plotted separately. On log-scale, the slope of $S(q)$ is the exponent of a power law or fractal dimension associated with the spatial structure of the trajectory on a given time range. At short times (data taken every 1 time steps) $S(q)$ has a power law shape with exponent 1 while at long times (data taken every 1000 time steps, near the late time plateau in the diffusion coefficient – see Figure 2.5) the slope of $S(q)$ is 2 (known to be the fractal dimension of a random walk). This corresponds to $1/H = 1$ and $1/H = 2$ at short and long times, respectively, in Figure 2.7.

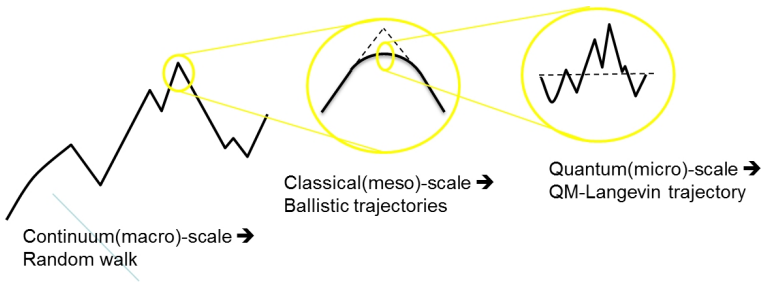

Figure 2.9. Schematic of structure of trajectory.

This behavior underscores the multi-scale aspect of the dynamics given by Equations 2.0.42. In fact, extending to the quantum-like case discussed in a previous section a schematic picture of the trajectory or flux in a multi-scale transport processes arises. This is depicted in Figure 2.9. At large resolution on observes the classical random walk type behavior with fractal dimension of the data (time trace of the trajectory or flux) $d_f = 2$. Also, the trajectory is continuous, but nowhere differentiable, almost surely. At a finer resolution the trajectory looks classical with linear fractal dimension and a well defined derivative in a finite difference sense. At still finer resolution one again recovers a fractal trajectory with $d_f = 2$, but this time due not to macroscopic thermodynamic effects, but due to quantum mechanical processes.

In addition to the multiscale aspect of this system, we can also assess the role of correlations in the Langevin dynamics. The Gaussian assumption for the propagator in dilute

systems seems very reasonable. Here we would again expect Gaussian type distribution of the probability density of finding a colloid at a particle point in time at long times. This is the late-time diffusive regime. Also, at early times when correlations are not relevant, we would expect again, Gaussian type probability distribution, but on that spreads as t^2 not t as for late times. However, what happens when correlations are significant? To examine this we plot the jump distribution, or self-part of the van Hove function (probability of a particle being at a given location having started at x_0). For all the colloids we determine the displacement at a given time $\Delta x(t) = x(t) - x_0$ and then histogram the displacements. For various times these are shown in Figure 2.10. It should be noted that in the main panel we have normalized the various jump distributions by the second moment which should have the effect of collapsing all the distributions onto a normalized Gaussian curve (the inset shows the time dependent data – curves spreading in time). For early and late times, the data do fall nicely onto a parabola in log-linear scale. However, at intermediate times, during the sub-diffusive, correlated regime, we see a broadening of the tails in the distribution which is not well fit by a Gaussian. In fact, it is well fit by a so-called q-Gaussian which is a generalization of the Gaussian function due to Tsallis [34] and is given by

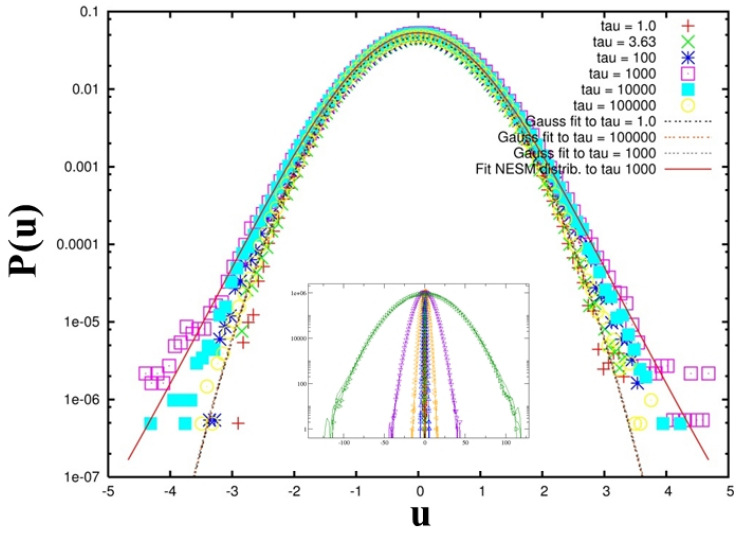

Figure 2.10. Jump distributions at various times for colloids at 40% volume fraction.

$$f(u) = \left[1 + (1-q)\left(\frac{u^2}{5-3q}\right)\right]^{\frac{1}{1-q}}, \tag{2.0.43}$$

where $u = \Delta x(t)/\sqrt{\langle \Delta x^2(t) \rangle}$. Once again we find a subtle difference with what has been discussed in the literature in that here, $q = q(\Delta t)$. At long time we recover the standard

$q(t \to \infty) = 1$, which is the Gaussian distribution. There analysis is also somewhat different from others based on CTRW type models [49], but the underlying math statistics may be similar in that the explanation of Tsallis statistics in terms of physical processes also relies on convolutions of probability densities [50]. This is a result of fluctuations within fluctuations, or a stochastic processes in a noisy environment.

Chapter 3

Diffusion in Inhomogeneous Systems

The previous chapter considered self-diffusion of colloids in equilibrium and macroscopically homogeneous systems. The analytical and numerical results helped to shed light on anomalous (non-Fickian and non-Gaussian) types of diffusive (mass) transport. Here we consider diffusive processes in inhomogeneous systems.

Hard sphere Color Diffusion

In this section we consider diffusion in hard sphere fluids and in particular the diffusion of inhomogeneous fluids, such as fluids at a planar hard wall. We study a problem of "color" diffusion, whereby hard spheres are labeled A or B but are otherwise identical in all respects, between planar hard walls. In the inhomogeneous fluid we consider a surface reaction. At the left wall a particle of species A is converted to one of species B upon a wall collision. At the opposing wall the reverse reaction takes place: $B \to A$. Using molecular dynamics simulation we study the steady state of this system. We demonstrate that in the inhomogeneous region (near the walls) a diffusing particle is subject to an equilibrium oscillatory force, the solvation force, that is due to the interfacial structuring of the fluid at the wall. For the particular case at hand, the solvation force can be determined in various ways, from a direct measurement of momentum transfer, from the pure hard sphere density profile, or from the potential distribution theorem. We use the solvation force to solve the continuum diffusion equation for the color diffusion. For the inhomogeneous fluid in the absence of any additional external fields, we do this using a constant diffusion coefficient, and demonstrate that this provides an adequate and accurate description of the reaction-diffusion problem. The simplicity of the analysis presented here can be contrasted with attempts that have required the introduction of a density dependent diffusion coefficient, $D(\rho)$. Given that the density variations in an inhomogeneous hard sphere fluid are on the length scale of a particle diameter, introducing a density dependence in that context would neither be physical or provide insight into diffusion processes in inhomogeneous regions. Finally, in Appendix B, we consider the more complex case of color diffusion in the presence of a slowly varying field such as gravity. This creates a gradual density variation on which the wall-induced inhomogeneities are superimposed. The analysis of this case shows that the steady-state flux still consists of the same contributions, a color density gradient term and a solvation force term. However, the latter is the solvation force of a pure hard sphere fluid in the same external field, and thus embodies the external

field contribution.

Background

The treatment of the problem of coupled reaction-diffusion has a long history, dating back to M. v. Smoluchowski who published the equation that carries his name in 1915. With the advent of molecular simulation there have been several attempts to refine the original treatment, and treat the effects of molecular aspects, including intermolecular interactions and external fields. Recently, De Michele and co-workers have performed molecular dynamics (MD) and event-driven Brownian dynamics (EDBD) simulations to determine the effects of density and intermolecular interactions on the encounter rate between hard spheres in a fluid and a spherical reactive sink. The EDBD simulations addressed three aspects that influence the encounter rate. These are: 1) the effect of density and intermolecular interactions, together referred to as "crowding" or "caging", 2) the variation of the diffusion coefficient with fluid thermodynamic conditions, and 3) the role of the velocity distribution.

This chapter seeks to address the first two aspects, using a setting that differs in two significant respects. First, we consider the large (more precisely, the infinite) radius limit of a spherical reactive sink: a planar wall reactive sink. Secondly, we consider a simple mass conserving reaction, i.e. $A \rightleftharpoons B$, that takes place at the planar wall. Using planar symmetry improves the statistics of the fluid particle reactive sink rate. In the traditional treatment the particle reacting with the sink is simply removed upon its arrival. At low reactant densities this is not a serious issue. However, in the simulations of De Michele et al. pure (hard sphere) fluids where employed at densities ranging up to typical liquid densities. At the latter conditions the complete removal creates an instantaneous change that is unphysical. That is, the sudden causes lack of mechanical equilibrium. In this paper we consider color diffusion in hard sphere fluids. In color diffusion, the diffusing and reacting particles are distinguished by the labels they carry, here A or B. Apart from these labels there are no other differences between the two species, both are interacting as hard spheres of identical diameters. This arrangement chosen guarantees that the diffusion and reaction phenomena take place in a system that is always at thermal and mechanical equilibrium. This simplifies the analysis, and allows equilibrium quantities to be used to analyze the diffusion in a inhomogeneous fluid.

We consider two kinds of color diffusion systems. Both consist of a hard sphere fluid confined by two parallel walls at which a surface reaction takes place (i.e., $A \rightarrow B$ at one wall, and the reverse reaction at the other). In the first arrangement only the walls act on the fluid. In the second scenario the fluid is also subject to a slowly varying one-body external field that acts over the entire range of the simulation box. The case we consider results in a constant force, and corresponds to the case of gravity. A main focus of the study is the treatment of the inhomogeneous region near the reactive wall, where large density oscillations present a challenge in the description of diffusion.

We demonstrate that by using the Smoluchowski diffusion equation, which describes the

diffusion in the presence of an external field, one can produce an accurate description of the reactive flux, provided the external field is identified as the equilibrium solvation force (between a diffusion particle and the planar wall). The solvation force is the appropriate representation of all the *equilibrium* solvent effects in the inhomogeneous region. The Smoluchowski-solvation force approach applies to both cases introduced above: with and without a slowly varying field such was gravity.

To derive the specific equations that underpin our approach we will use the potential distribution theorem approach, due to Widom. This provides a convenient and transparent formalism for the description of inhomogeneous fluids. We will use it to derive the Smoluchowski diffusion equation for inhomogeneous fluids. The paper describes the results of molecular dynamics as well as EDBD simulations to validate the proposed analysis, and how to apply in specific situations of relevance to important reaction-diffusion phenomena.

The Potential Distribution Theorem (PDT)

We will start by considering the operational definition for the chemical potential in a single component inhomogeneous fluid, such as a hard sphere fluid in an external field. Widom showed that the local chemical potential, $\mu(\mathbf{r})$, can be obtained through the so-called potential distribution theorem, which provides a description of the configurational contribution to the chemical potential. The PDT links the chemical potential at a position $\mathbf{r}$ to the local number density, $\rho(\mathbf{r})$, and the local potential energy of a test particle, $U_t(\mathbf{r}) + V_{ext}(\mathbf{r})$

$$\begin{aligned} \beta\mu(\mathbf{r}) &= ln\rho(\mathbf{r}) - ln < e^{-\beta(U_t(\mathbf{r})+V_{ext}(\mathbf{r}))} > \\ &= ln\rho(\mathbf{r}) - ln < e^{-\beta(U_t(\mathbf{r}))} > +\beta V_{ext}(\mathbf{r}), \end{aligned} \tag{3.0.1}$$

where $\beta = (kT)^{-1}$, with T the temperature and k the Boltzmann constant. The angled brackets denote an ensemble average of the test particle insertion at $\mathbf{r}$. Note that the test-particle is identical to the actual fluid particles, interacting through the same interaction potential. The difference lies in the fact that the test particle is a spectator that can probe the local energy, but does not in any way affect the fluid particles. In practical terms, say one performs a Monte Carlo or molecular dynamics simulation, then periodically one stops the simulation and inserts a test particle at position $\mathbf{r}$ and measures its potential energy. The latter comes in two contributions. One is simply the local value of a one-body external field, $V_{ext}(\mathbf{r})$. This contribution does not depend on the position of the fluid particles but solely on the test-particle's location and hence can be taken outside the ensemble average. The other is due to the interactions with the particles that make up the actual fluid.

At equilibrium the chemical potential is constant throughout the volume, independent of position. For inhomogeneous fluids, each term on the right hand side varies with position, but the PDT states that the sum of the two terms must be a constant, independent of position.

For a fluid between two planar hard walls we rewrite the above equation as

$$\beta\mu(z) = ln\rho(z) - ln < e^{-\beta U_t(z)} > +\beta V_{ext}(z). \tag{3.0.2}$$

Specializing to a fluid between hard walls located at $z = 0$ and $z = L$ we have $V_{ext}(z) = 0$ for $0 < z < L$ and the writing of the PDT simplifies to

$$\beta\mu(z) = ln\rho(z) - ln < e^{-\beta U_t(z)} >; \quad 0 < z < L \tag{3.0.3}$$

$$\equiv ln\rho(z) + \beta\mu^{ex}(z), \tag{3.0.4}$$

where the second line defines the local excess chemical potential.

Further specializing to a hard sphere fluid leads to a simple geometrical interpretation of the second term. Namely, for a hard sphere fluid the Boltzmann factor $exp(-\beta U_t(z))$ can only take on two values: unity when the test-particle does not overlap with any of the fluid particles and zero when there is an overlap. In other words, the ensemble average $< exp(-\beta U_t(z)) >$ is simply a probability, namely the probability that a hard sphere can be inserted at a distance z, without overlap. The constancy of the chemical potential implies that when a system is in equilibrium, there is no net drift of matter from one part of the system to another. Rewriting the constancy of the chemical potential in differential terms, we have,

$$\frac{\partial ln\rho(z)}{\partial z} = -\frac{\partial \mu^{ex}(z)}{\partial z} = \frac{\partial ln < e^{-\beta U_t(z)} >}{\partial z}; \quad 0 < z < L. \tag{3.0.5}$$

Now, consider the net force on a particle in the fluid. In a bulk fluid this force is zero, because of symmetry. However, in the inhomogeneous fluid that force is not zero everywhere, but rather depends on position. For a fluid at a planar wall the normal component of the force depends on the distance, z, form the wall. The tangential components are still zero on average.

Coarse-Grained Densities

The local excess chemical potential is a function of position z, not just a function of the local density, $\rho(z)$. Its definition clearly shows that it depends on the averages over configurations of hard spheres in the neighborhood of z. A test-particle inserted at z can directly interact (i.e., exhibit potential overlaps) with fluid hard spheres which have positions ranging from $z - \sigma$ to $z + \sigma$. Fluid particles near z, have the largest potential impact, and particles near $z + / - \sigma$ have the least.

An approximation for the local excess chemical potential could be sought by equating it to the bulk excess chemical potential at a local coarse grained density, $\bar{\rho}(z)$. In other words,

$$\mu^{ex}(z) \quad = \mu^{ex}(\bar{\rho}(z)). \tag{3.0.6}$$

And the nonlocal coarse-grained density may be a weighted density of the form:

$$\bar{\rho}(z)) = \int_{z-a}^{z+a} dz\prime w(|z - z\prime|)\rho(z\prime), \tag{3.0.7}$$

where the weight function, w is normalized to unity, so that in the bulk region, where $\rho(z) = \rho_b$, $\mu_{ex}(z)$ reduces to a bulk expression, i.e., $\mu_{ex}(\rho_b)$.

The Solvation Force

As a sphere of species i diffuses through the inhomogeneous fluid it is subject to a position-dependent force. This is the so-called solvation force between a sphere and the planar wall and it is due to the structuring of the fluid that separates the two objects. In general, the solvation force, $F(z;d)$, can be easily determined in a simulation (see Challa and van Swol [**?**]) by fixing the center of a sphere of diameter d at a distance z from the wall and measuring the net force on the sphere. In a hard sphere simulation we could measure the total force as the sum of all the momentum transfers due to colliding neighboring spheres.

The solvation force experienced by a stationary sphere is an oscillatory function with an oscillation period that is on the order of the fluid particle diameter (σ). It reflects the non-symmetrical nature of the fluid packing around the sphere of diameter d due to the presence of the wall. The solvation force is a potential of mean force, and the associated potential,$V(z;d)$ is the solvation potential. A noninteracting (ideal) gas of bulk density, ρ_b^{id}, in an external field $V(z;d)$ would exhibit a density profile that is identical to that of an interacting inhomogeneous hard sphere fluid of the same bulk density. Thus, the solvation potential and force can be viewed as the collective effect of all the surrounding spheres that make up the fluid on a sphere of interest.

For such an ideal gas in an external field we have a profile given by the barometric law, specializing to $d = \sigma$,

$$\rho(z) \quad = \quad \rho_b(z)e^{-\beta V(z,\sigma)}; \quad 0 < z < L, \tag{3.0.8}$$

or

$$\frac{\partial ln\rho(z)}{\partial z} \quad = \quad -\beta\frac{\partial V(z,\sigma)}{\partial z}. \tag{3.0.9}$$

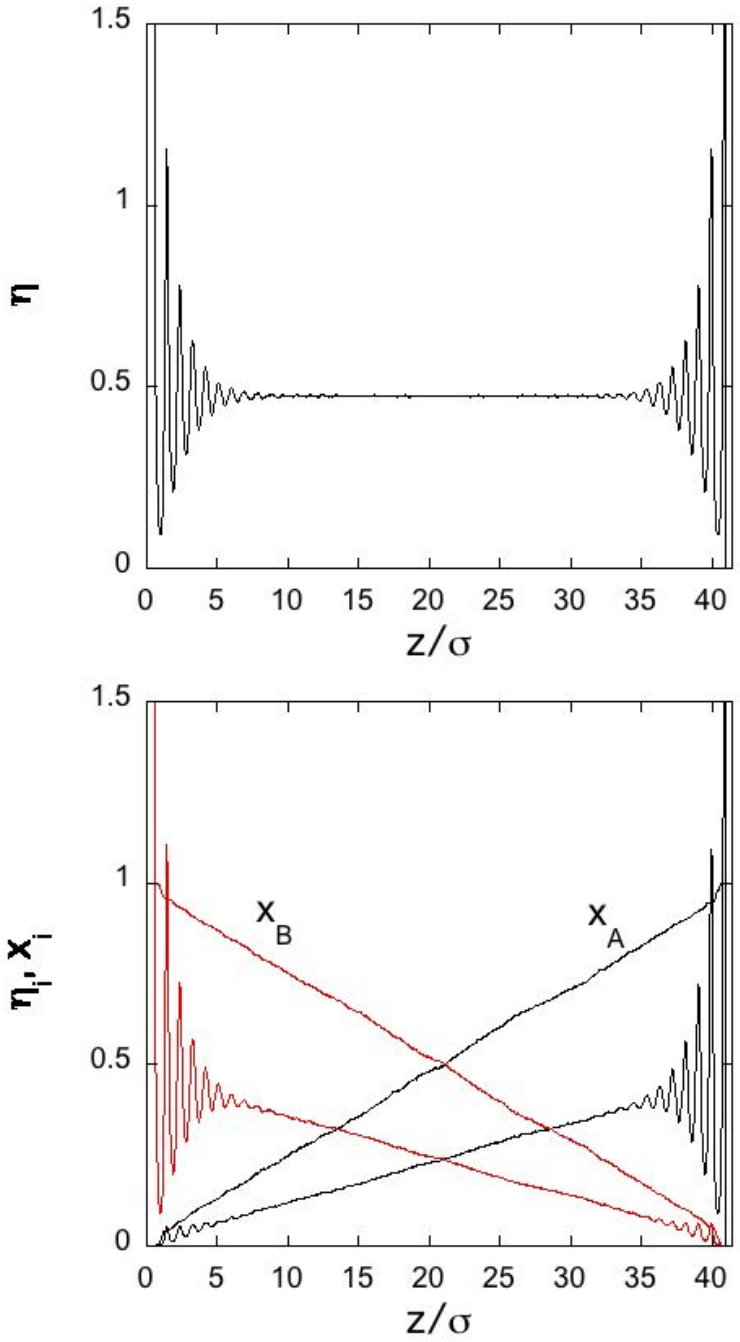

Figure 3.1. Density profiles for the high density fluid between two planar hard walls. The top panel shows the local packing fraction, $\eta = (\pi/6)\rho\sigma^3$, of the equilibrium hard sphere fluid. The bottom panel shows the results for the component profiles, η_i $(i = A, B)$, for the fluid undergoing color diffusion. A surface reaction on the left converts species A into B upon a wall collision. The reverse reaction takes place on the right hand side of the simulation box. The figure shows the steady-state profiles of species A (black) and B(red). The profiles for the separate components show the effects of packing near the wall, the mole fraction profiles, $x_A(z)$(black) and $x_B(z)$(red), for each species are free of oscillations.

A comparison with the inhomogeneous hard sphere fluid, equation 3.0.26, then identifies the effective field as the excess chemical potential.

$$\frac{\partial V(z,\sigma)}{\partial z} = \frac{\partial \mu^{ex}}{\partial z}. \tag{3.0.10}$$

Color Diffusion

In this section we consider a simple diffusion process in an inhomogeneous monodisperse hard sphere fluid. We consider a hard sphere fluid confined between two parallel walls, located at $z = 0$ and $z = L_z$. The walls act as hard walls, preventing any sphere center from penetrating. The system is run under conditions of a constant number of particles (N), constant volume (V), and constant temperature (T).

To set up color diffusion one labels the spheres with a color or tag, say A and B. The labeling has no effect on any of the interactions among the spheres, which continue to interact as hard sphere collisions between spheres and hard walls. Once the spheres have been labeled one can follow the location of the spheres in the fluid; studying a transient diffusion processes for instance.

First, we state the PDT results for the equilibrium binary A, B mixture. For each component we have,

$$\begin{aligned} \beta\mu_i(z) &= ln\rho_i(z) - ln < e^{-\beta U_{t,i}(z)} > + \beta V_{ext}(z); \qquad i = A, B & (3.0.11)\\ &= ln\rho_i(z) + \beta\mu^{ex}. & (3.0.12) \end{aligned}$$

We note that in the second line we dropped the species subscript. This is a direct consequence of the fact that we are considering a color mixture, that is, a binary mixture of two species of equal diameter. Thus, the configurational chemical potential, as the PDT makes clear, equals minus the logarithm of the probability of being able to insert a sphere of diameter σ at a distance z from the wall. The insertion does not depend on the label of the particle, thus the excess chemical potential at a given position z is the same for each species, and equal to the excess chemical potential of the pure hard sphere system that results when all labels are removed.

Using equation 3.0.25 and $\rho = \rho_A + \rho_B$, we can express the chemical potential of species i in terms of the pure hard sphere fluid and the local molefraction, viz.,

$$\beta\mu_i(z) = \beta\mu + lnx_i(z); \qquad i = A, B, \tag{3.0.13}$$

where $x_i = \rho_i/(\rho_A + \rho_B)$. Thus, for an inhomogeneous equilibrium color mixture the local density varies, but the the local mole fraction is constant throughout.

Now, consider the case of diffusion coupled to a surface reaction. A color surface reaction can occur at a wall when a sphere collides with the wall. To be specific, consider an anti-symmetric system, where the left wall will convert spheres of type A to spheres of type B and leave spheres of type B unchanged. Similarly, at the right hand wall we consider the complimentary reaction, $B \to A$, while species A will be unaffected by a wall collision. The precise reaction behavior at the wall is easily generalized to other variants. For instance, upon the colliding with the wall, one can apply a probability $0 \leq q \leq 1$ that the reaction will actually proceed. In addition, one could allow for the reaction to proceed in either direction, i.e., $A \rightleftharpoons B$, with forward and backward rates set by probabilities $0 \leq q_F, q_B \leq 1$. This allows for the study chemical equilibria, but also allows for steady-state behavior when q_F and/or q_B take on different values at the opposing walls.

If a simulation is run with an anti-symmetric set of wall reactions a steady-state concentration profile will develop. At steady-state the concentration of species A will decrease from right to left while the concentration of B will decrease from left to right. This is shown in Figure 3.1. Notice that the concentration profiles are anti-symmetric, as expected, but they are no monotonic. In stead, in the neighborhood of the wall, each species exhibits oscillations in space. These oscillations are manifestations of the oscillatory nature of the density itself.

The Smoluchowski Equation

We will now consider the continuum approach of diffusion and seek to apply it to the color diffusion problem. Our starting point is the Kramers-Klein equation, which is a special case of the Fokker-Planck equation for a Brownian particle in an external field [51]. It describes the behavior of a density distribution in time and space. In the high friction limit, where the velocity distribution rapidly thermalizes, we can limit ourselves to the positional equation. This is known as Smoluchowski's diffusion equation. In the case of one-dimensional diffusion we have,

$$\frac{\partial \rho_i}{\partial t} = D\frac{\partial^2 \rho_i}{\partial z^2} - \frac{1}{\zeta}\frac{\partial K\rho_i}{\partial z} \tag{3.0.14}$$

$$= D\frac{\partial}{\partial z}\left(\frac{\partial \rho_i}{\partial z} - \frac{K\rho_i}{kT}\right) \; ; \qquad i = A, B, \tag{3.0.15}$$

the first term describes pure diffusion, while the second describes the drift under the influence of a position dependent external force, $K(z)$. ζ denotes the drag, and is related to the diffusion coefficient through $D = kT/\zeta$. In the expression formulated here, the diffusion coefficient is considered to be a constant, independent of position.

Introducing the flux of species i in the $z-$direction, j_i, we can also express the diffusion process as

$$\frac{\partial \rho_i}{\partial t} = -D\frac{\partial j_i}{\partial z}\ ; \qquad i = A, B. \tag{3.0.16}$$

At steady-state conditions $\partial \rho_i/\partial t = 0$ and the flux of species i is a constant. Hence, from equation 3.0.15, we obtain,

$$j_i = -D\frac{\partial \rho_i}{\partial z} - D\frac{K(z)\rho_i}{kT}; \qquad i = A, B. \tag{3.0.17}$$

In the case of color diffusion coupled with surface reaction, we can easily measure the steady-state flux j_i at any point in space, including at either wall (i.e., at $z = 0$ or $z = L_z$). In addition, we can readily obtain the density profiles $\rho_i(z)$. This puts us in a position to identify the spatially varying force as:

$$\begin{aligned} \frac{K(z)}{kT} &= \frac{j_i}{D\rho_i} + \frac{1}{\rho_i}\frac{\partial \rho_i}{\partial z}; \qquad i = A, B \\ &= \frac{j_i}{D\rho_i} + \frac{\partial ln\rho_i}{\partial z}. \end{aligned} \tag{3.0.18}$$

The above is all applicable to a *pure* hard sphere fluid. If such a system is at equilibrium this implies that the flux vanishes, and hence we find that

$$\begin{aligned} \frac{K(z)}{kT} &= \frac{\partial ln\rho}{\partial z} \\ &= \frac{\partial \mu^{ex}}{\partial z}. \end{aligned} \tag{3.0.19}$$

In other words, in the color diffusion problem, the external driving force $K(z)$ that represents the influence of all the surrounding spheres on a sphere diffusing (toward or away from a wall) is, in fact, the solvation force acting on the diffusing sphere. In addition, that solvation

force is given in terms of the density profile of the pure hard sphere equilibrium problem. This approach is naturally attractive, since the solvation force, $K(z)$, is indeed the force that can be mechanically measured as a sphere moves through a hard sphere fluid.

This implies that the color diffusion problem can be solved by finding the solution to the diffusion equation 3.0.15, applying as an external force $K(z) = \partial ln\rho/\partial z$, obtained from the equilibrium profile of the pure hard sphere system at the appropriate bulk density, and using for D the bulk diffusion coefficient for the same pure hard sphere system. This approach allows for a complete time and space dependent solution $\rho_i(z,t)$. Setting the left hand side of equation 3.0.15 to zero leads to the steady state solution, $\rho_i(z)$.

The analysis outlined here, whereby the effect of the fluid particles are represented as an external force $K(z)$ and D is considered a constant is to be contrasted with the approach taken by De Michele and co-workers. Those workers have considered a very closely related problem of reaction-diffusion in spherical symmetry. Their system consisted of a pure hard sphere fluid in a spherical container. At the center of the container was placed a fixed reactive sphere of diameter d. Upon colliding with this spherical sink, a hard sphere would be instantaneously removed from the sample, and re-introduced at the spherical boundary. After a transient time, a steady-state develops where the fluid particle density vanishes at the surface of the spherical reactive sink. The system differs slighly from ours in that in the De Michele approach the removal of the sphere forces the density at the sink surface to be zero, and hence the density distribution of the fluid can not be an equilibrium distribution. However, there is in principle no problem with a study of the color diffusion problem in spherical geometry.

In De Michele's system, like in the one we presented, the diffusion takes place through an inhomogeneous structured fluid. Surrounding the spherical reactive sink the radial fluid structure, closely resembling the product $\rho g(r)$ of the bulk density and the radial distribution function. In their treatment, De Michele, treated the diffusion problem through the structured fluid by introducing a diffusion coefficient dependent on the local density $D(\rho(z))$.

A density-dependent diffusion coefficient is an appropriate choice when the density is slowly varying. This situation is familiar in the description of the atmosphere, where the density is indeed very slowly varying, and the gravitational length is of the order of a kilometer. However, in a dense inhomogeneous fluid the fluid structure varies rapidly on very short length scale, of order σ, and the amplitude of the local density can grow well above any reasonable bulk limit. This problem occurs in different guises in different contexts. In density functional theory the free energy is considered a functional of the density, and one often introduces so-called weighted densities $\bar{\rho}(z)$, that are obtained as some form of weighted integrals over a finite range (also of order σ) of the local density $\rho(z)$ (i.e., a "smeared out" density). Such weighted densities are much more gently behaved, although they still exhibit some undulations.

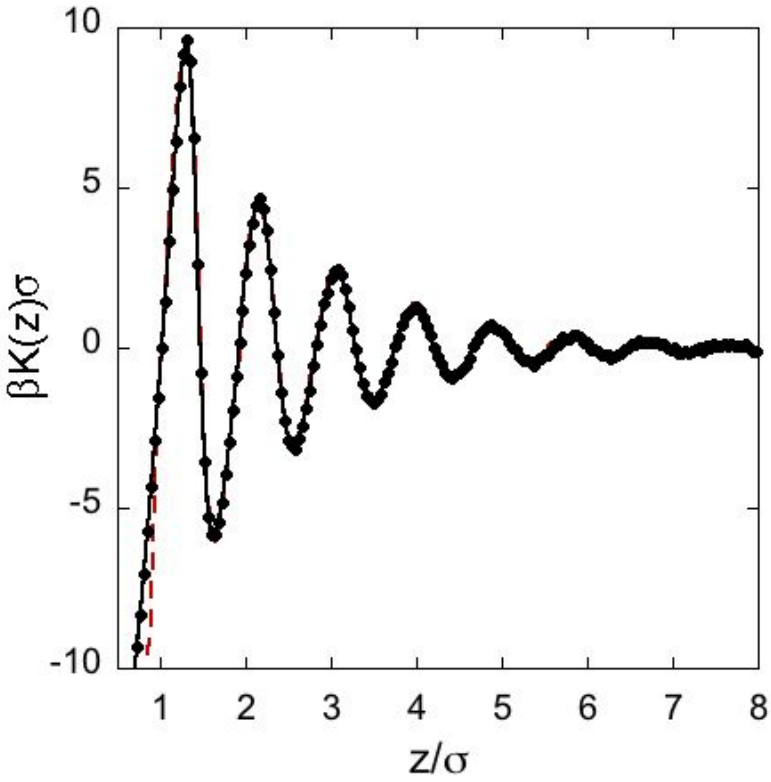

Figure 3.2. A comparison of three routes to the force $K(z)$. The black (species$A$) and red dashed (species B) curves represent the right hand of equation 3.0.18, using the measured fluxes j_A and j_B, in combination with the profiles $\rho_A(z)$ and $\rho_B(z)$, respectively. The solid circles represent the measured average net z-component of the solvation force on a sphere at position z. The noise of the red curve is larger than that of the black curve because the value $\rho_A(z)$ is very small at the left hand side wall. Note that each term on the right hand side of equation 3.0.18 diverges (in opposite directions) as $\rho_A(z) \to 0$.

Simulation Results

In this section we will illustrate the ideas outlined in the introductory sections with the help of some color diffusion molecular dynamics simulations. We performed two simulations on 4000 hard spheres in a rectangularly shaped box, of square cross section. Planar hard walls, placed in the $z-$direction at $z = 0$ and $z = L_z$, do not allow any sphere center to approach closer than $\sigma/2$. Periodic boundary conditions are applied in the remaining directions. Similar simulations were described by Henderson and van Swol [52], and the reader is referred to that study for simulation details. The box dimensions and the thermodynamic data are collected in Table 3.1. The simulation started with randomly labeling 2000 spheres A, and the remainder B. At the left wall, each sphere of species A that collided with the wall was relabeled B, while on the opposing wall colliding B's were converted to species A. After some time a stationary density profile develops, signaling that a steady state whereby two opposing constant fluxes develop. Species A showing net transport from right to left and species B in the opposite direction. The left wall acts as a reactive sink for species A and the opposite wall is a reactive source. The reverse applies to species B.

Table 3.1. Dimensions and thermodynamic results for $N = 4000$ and a rectangular simulation box with square cross section ($L_x = L_y$). We provide the normal pressure p_N and invert the hard-sphere bulk equation of state to obtain the bulk packing fraction, η_b. The diffusion coefficient is the bulk self-diffusion coefficient, which we obtained from the analysis by Heyes et al. [53]. The flux, j, is the average of the conversion at the left wall where $A \to B$ and the right wall where $B \to A$.

L_x/σ	A/σ^2	$\beta p_N \sigma^3$	η_b	$D(m/kT\sigma^2)^{1/2}$	$j\sigma^3(m/kT)^{1/2}$
47.1599	144.9611	2.3335	0.3030	0.19866	0.2241×10^{-2}
40.4661	107.4650	9.8042	0.4728	0.03397	0.6195×10^{-3}

The results are displayed in figure 3.1. Because of the simplicity of the model the density profiles are perfectly anti-symmetric, and the density profile of the entire system, viewed as a pure hard sphere fluid, is at equilibrium at all times. Thus there is thermal and mechanical equilibrium. There is also chemical equilibrium for the unlabeled spheres, as expressed by the PDT, see equation 3.0.26. However, there is a chemical potential gradient for each separate species. The latter results from the reaction conditions at the wall. The reaction $A \rightleftharpoons B$ takes place with probability 1 at each wall, and hence the conversion rate is determined by the contact densities at the wall. That is, $\rho_A(z = \sigma/2)$ and $\rho_B(z = L_z - \sigma/2)$. In the hard sphere system these contact densities are directly related to the system's pressure,p. Namely,

$$\beta p \;=\; \rho_A(\sigma_+/2) + \rho_B(\sigma_+/2), \tag{3.0.20}$$

where the plus sign indicates that we take the limit $z \rightarrow \sigma/2$ from above.

Our simple choice of surface reaction makes it straightforward to measure the fluxes j_A $=j_B$, as the number of conversions N_{AB} of A to B (and N_{BA} for the reverse reaction), per unit area and per unit time. This is because for a one-dimensional diffusion problem the constancy of flux in time implies a constancy of flux in space.

Having determined the fluxes and the density profiles, it is possible to perform a direct assessment of the force $K(z)$ in the Smoluchowski equation 3.0.18. That is, for each species we can determine each term on the right hand side of equation 3.0.18, namely $j_i/(D\rho_i)$ and $\partial ln\rho_i/\partial z$. By adding the terms we obtain estimates for the force $K(z)$. The results are shown in figure 3.2 for the left wall. The two curves (black and red) correspond to species A and B respectively.

Although formally equivalent, the accuracy of the two routes are not the same. As the left wall acts as a reaction sink for species A, $\rho_A(z)$ approaches zero at that wall. That causes both terms of equation 3.0.18 to diverge (in opposite directions), and hence the error in determining $K(z)$ from $\rho_A(z)$ grows large at that wall. In the figure, the deviations become apparent when $z < 0.9\sigma$, where $\rho_A(z)\sigma^3 < 1.5 \times 10^{-3}$. An added source of inaccuracy stems from the central difference approximation used to calculate the slope $\partial ln\rho_i(z)/\partial z$. In contrast, the errors in extracting $K(z)$ from $\rho_B(z)$ are well-behaved. Also shown in the same figure is the result of a direct measurement of the average z-component of the net force on a sphere at position z from the wall, i.e., the solvation force. We conclude that there is excellent agreement between the different routes, demonstrating that the Smoluchowski equation can be successfully used in the description of the diffusion of hard spheres in the inhomogeneous region near a hard wall.

The point of view embodied by the Smoluchowski approach is that of Brownian motion of a particle that is acted on by the external field $K(z)$. In our context, we map a fully interacting system of labeled hard spheres onto a system of independent Brownian particles in a field $K(z)$. The mapping involves replacing the explicit many-body effects of the fluid particles by an average solvation force (a potential of mean force). Our analysis of the molecular dynamics results demonstrate that for the color diffusion problemthe role of $K(z)$ is indeed played by the solvation force (see figure 3.2) .

Given that this external field is oscillatory, the steady-state density profile also appears highly oscillatory. The sequence of barriers presented by $K(z)$ are significant, as can be seen from figure 3.2, which shows that several are larger than the thermal energy, kT.

Relevance to liquid metal solutions

In the previous section, the role of thermodynamic conditions (through the chemical potential) on the diffusion of hard spheres was addressed. Here, the relevance of this line of thought to liquid metal solutions is considered. In the first subsection the relevance of hard

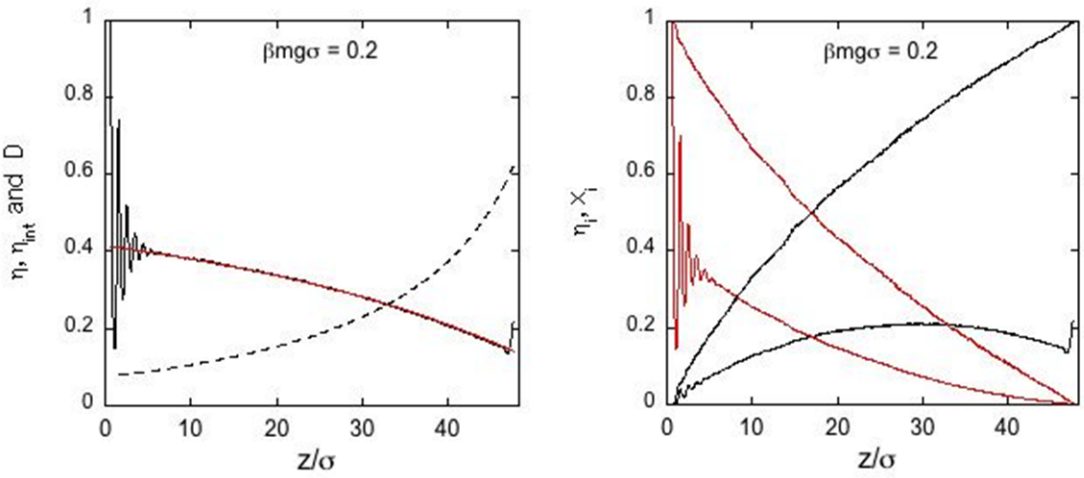

Figure 3.3. Density profiles for the high density fluid between two planar hard walls in the presence of a gravitational field of strength $\beta mg\sigma = 0.2$, and pointed to the left. The top panel shows the local packing fraction, $\eta = (\pi/6)\rho\sigma^3$, of the equilibrium hard sphere fluid (solid black). In addition, we show, in red, the intrinsic packing fraction profile that corresponds to the linear intrinsic chemical potential, μ_{int} (see text). This profile coincides with the local packing fraction profile except close to the wall, where the intrinsic profiley remains monotonic, and free of oscillations. The bottom panel shows the results for the component profiles, η_i $(i = A, B)$, for the fluid undergoing color diffusion. A surface reaction on the left converts species A into B upon a wall collision. The reverse reaction takes place on the right hand side of the simulation box. The figure shows the steady-state profiles of species A (black) and B(red). The profiles for the separate components show the effects of packing near the wall. In addition, the presence of the gravitational field produces a packing fraction profile for species A, that displays a maximum (around $z = 32.6\sigma$). The mole fraction profiles, $x_A(z)$(black) and $x_B(z)$(red), for each species are free of oscillations. Note that in contrast to the $g = 0$ case, the mole fraction profiles are no longer straight lines, and the intersection point of equal composition is to the left of the center of the box, signifying that the overall mole fraction is no longer 0.5. The top figure also shows the position dependent diffusion coefficient, $D(z) = D(\mu_{int}(z))$, based on the fit of Heyes et al.

sphere simulations and theory to the transport coefficients (self diffusion, viscosity) of liquid metals is considered. In the last subsection the role of heterogeneity (i.e., multiple species or components) is considered with a view toward reactive wetting applications (e.g., joining and brazing).

Equilibrium Pure Liquid Metals

The fact that for the problem at hand liquid metals can be considered classical simple liquids helps to make the problem considerably more tractable. That is, liquid metals are atomic fluids, and can be successfully described with interatomic potentials that are spherically symmetric and short-ranged. The classical potential of choice is the embedded-atom method (EAM) potential, which is a multi-body potential with a contribution that depends on the local density surrounding two interacting atoms i and j. However, the potential energy given by the EAM potential can still be written as a function of all the pair distances. As with traditional pair-potentials, the force of a particle i, $\mathbf{F}_i$, can still be written as a sum over central pair forces, $\mathbf{F}_{ij} = -\mathbf{F}_{ji}$, i.e.,

$$\mathbf{F}_i = \sum_{j \neq i} \mathbf{F}_{ij}. \tag{3.0.21}$$

Molecular simulation

As a result of the pair property for the energy, it is straightforward to perform standard molecular simulations (molecular dynamics or Monte Carlo) for metals; and a definition of a local pressure tensor (the negative of the Cauchy tensor) is free of complications, as is the mechanical route to the surface tension.

Perturbation theory

In addition, just like the quintessential simple liquids, the noble gases, the liquid structure of metals is dominated by the short-range (repulsive) part of the interatomic potential. Loosely speaking, a liquid metal can be considered to be a collection of repulsive spheres moving around in a more uniform attractive background. As a result, one can successfully apply WCA (Weeks, Chandler and Andersen) perturbation theory, which starts by writing the interatomic potential as the sum of a repulsive and an attractive term. The repulsive term is so short-ranged that it can be represented by a hard sphere potential (with a suitable hard sphere diameter). Hence the liquid structure, as expressed by the radial pair distribution function, $g(r)$, and thus all the equilibrium thermodynamic properties can be calculated from the knowledge of the free energy of the hard sphere fluid and the application of an attractive perturbation. The attractive contribution is calculated as an integral over the reference fluid's $g(r)$. This produces very accurate thermodynamic properties of the dense

fluid, typically within $1-2\%$ of the values calculated by the 'exact' molecular simulation approach. In a strict mean field theory a further approximation is made: $g(r) \approx 1$. This, of course, simplifies the calculation at the expense of reduced accuracy of the equation of state.

Classical Fluids DFT

The strict mean field equation of state is what underlies classical fluids density functional theory (CF-DFT). This is an important observation since CF-DFT can be viewed as the inhomogeneous analogue of perturbation theory and strict mean field theory. It is a powerful technique that allows one to determine the interfacial properties, that is, density and composition profiles and the surface free energy.

Dynamical Properties of liquid metals

Over the decades there has been much effort devoted to predicting the self-diffusivities of simple liquids. The basic assumption (see the work of Protopapas, Andersen and Parlee [54]) made is that the self-diffusion coefficient of a simple liquid is equal to that of an appropriate hard sphere(HS) fluid. The basic idea for this assumption, contrasting the roles of repulsive and attractive forces, goes back to van der Waals and Boltzmann (see the paper by Ben-Amotz and Herschbach [55]) and it has been embodied in the modern theory of fluids. Since the hard sphere fluid is characterized by just the hard sphere diameter, determining the appropriate hard sphere fluid is equated with specifying a hard sphere diameter for the simple liquid of interest.

Thus, two ingredients are required, 1) the self-diffusivity of the hard sphere fluid as a function of density, and 2) a determination of the equivalent hard sphere diameter.

Hard sphere self-diffusivity: Enskog Theory.

The well-known Enskog theory approximation for the hard sphere self-diffusion coefficient is

$$D_E = \frac{3}{8\rho\sigma^2}\left(\frac{kT}{\pi m}\right)^{1/2}\frac{1}{g(\sigma)} \equiv \frac{D_0}{g(\sigma)}, \tag{3.0.22}$$

where m and σ denote the mass and diameter of the hard sphere, k is Boltzmann's constant and T is the absolute temperature, and ρ is the number density. $g(\sigma)$ is the value of the radial distribution function , $g(r)$ (or rdf), at contact (i.e., at closest approach: $r = \sigma$). The latter is related to the equation of state. In terms of $Z \equiv p/kT$ (the compressibility factor),

we have

$$g(\sigma) = \frac{Z-1}{4\eta} \approx \frac{1-\frac{1}{2}\eta}{(1-\eta)^3}, \tag{3.0.23}$$

where the packing fraction $\eta = (\pi/6)\rho\sigma^3$ characterizes the dimensionless density.

At low densities $\eta < 0.1$ the Enskog expression is accurate. At intermediate $0.1 < \eta \leq 0.4$ it is too small, while for larger values, it rapidly becomes too large. Using MD HS data a better fit has been developed for the HS self-diffusivity (D_{HS}) which covers the entire density range, all the way to random close packing

$$\begin{aligned} D_{HS}(\eta) &= D_E(\eta) f_D(\eta) & (3.0.24)\\ f_D(\eta) &= 1 + 2.4699\ \eta^{3/2} + 9.7682\ \eta^3 - 144.5786\ \eta^5 + 246.7832\ \eta^7. & (3.0.25) \end{aligned}$$

Equivalent hard sphere diameter

There exists several approaches to assign an equivalent hard sphere diameter to a simple fluid atom (or molecule). Experimentally, these can be based on various approaches, including second virial coefficients, equation of state data and molecular refractivities (i.e. polarizabilities). Theoretical routes include Boltzmann's approach and perturbation theory (which comes in slightly varying forms).

Ben-Amotz andd Hersbach [55] present a nice overview of the many ways an effective hard sphere diameter can be obtained. Common to all is that this diameter is temperature dependent, that is $\sigma = \sigma(T)$, and sometimes slightly density dependent as well (e.g., WCA). $\sigma(T)$ is always a decreasing function of temperature. This stems from the fact that a higher temperature, the increased kinetic energy allows atoms to explore close distances.

Several prescriptions and fits are available for $\sigma(T)$, and differ based upon which class of fluids is being studied (e.g., metals, molecular fluids, Lennard-Jones model fluids). For metals, Protopapas et al. [54] first introduced

$$\sigma(T) = \sigma_m \frac{1 - B(T/T_m)^{1/2}}{1-B}; \qquad B = 0.112, \tag{3.0.26}$$

where T_m denotes the melting temperature. Protopapas et al. [54] define σ_m, the diameter at the melting temperature, as follows. They assume that for all liquid metals at T_m, the packing fraction at the melting point is a constant equal to 0.472:

$$\eta_m = \frac{\pi}{6}\rho\sigma_m^3 = 0.472. \tag{3.0.27}$$

This fixes[1] the value of σ_m. Notably, $\sigma(T)$ is based just on the melting temperature and the melting density.

Hard sphere fluid viscosity

Given that the Stokes-Einstein relation

$$D_{HS} = \frac{kT}{c\pi\mu_{HS}\sigma}, \tag{3.0.28}$$

links the diffusion to the viscosity, μ_{HS}, it comes as no surprise that the equivalent hard sphere diameter can also be used to predict the viscosity of a liquid based on the value of an equivalent hard sphere fluid. In equation 3.0.28 the constant c equals 3 for stick BC's and equals 2 for slip BC's.

Protopapas et al. [56] describe this in a second paper. The Enskog theory approximation for the hard sphere viscosity is

$$\mu_E = \frac{5}{16\sigma^2}\left(\frac{mkT}{\pi}\right)^{1/2} 4\eta\left[\frac{1}{4\eta g(\sigma)} + 0.8 + (0.7614)4\eta g(\sigma)\right] \tag{3.0.29}$$

$$\equiv \mu_0 4\eta\left[\frac{1}{4\eta g(\sigma)} + 0.8 + (0.7614)4\eta g(\sigma)\right]. \tag{3.0.30}$$

As was the case for self-diffusion, MD simulations have provided a correction factor to lead to an expression for the viscosity[2]

$$\mu_{HS}(\eta) = \mu_E(\eta) f_\mu(\eta) \tag{3.0.31}$$

$$f_\mu(\eta) = \frac{16\sigma^2}{5}\left(\frac{\pi}{mkT}\right)^{1/2} \frac{2kT}{\pi D_E f_D(\eta)}\ \frac{1}{4.285 - 0.4128\eta}. \tag{3.0.32}$$

Alternatively, an entirely empirical $f_\mu(\eta)$ can be generated by fitting experimental values of μ/μ_E, as was done by Protopapas et al. [56].

Equilibrium Liquid Metals Mixtures

Given that the metals are atomic fluids and given that the pure metals liquids are so-called simple liquids, it is not surprising that liquid mixtures (alloys) of metals are simple

[1] Putting equations 3.0.26 and 3.0.27 together gives $\sigma(T) = 1.288 \times 10^{-8}\rho_m^{-1/3}[1 - 0.112(T/T_m)^{1/2}]$, with ρ_m the number density in cm^{-3} at the melting point

[2] This specific form arises from a fit to the product $\mu_{HS}D_{HS}$, which varies far more slowly than either term. In particular, a good fit to the MD data of Alder et al. [57] is $2kT/\pi\mu_{HS}D_{HS} = 4.2852 - 0.4128\eta$, see reference [56]

liquid mixtures. However, that statement does not imply that all metal mixtures are simply ideal solutions (they are not). Immiscibility, partial miscibility, compound formation, and non-ideality are well within the scope of mixtures of simple liquids.

Molecular simulation of mixtures

To simulate a binary mixture of metals A and B requires an extension of the EAM approach to metals. For mixtures of noble gases, simple pair-potentials such as the well-known two-parameter Lennard-Jones potential can be used, and the two parameters (ϵ and σ) used for the pure fluid are replaced by species dependent ones: ϵ_{AA}, ϵ_{BB} and ϵ_{AB}, and similarly for σ. If the pure fluid parameters, ϵ_{ii} and σ_{ii}, with $i = A, B$ are known, estimates for the parameters, ϵ_{AB} and σ_{AB} can either be simply stipulated or alternatively constructed from the pure species values by the application of a so-called "mixing rule". For noble gases one often uses

$$\begin{aligned} \epsilon_{AB} &= (\epsilon_{AA}\epsilon_{BB})^{1/2} \\ \sigma_{AB} &= (\sigma_{AA} + \sigma_{BB})/2. \end{aligned} \tag{3.0.33}$$

These mixing rules are referred to as the Lorenz-Berthelot rules. They reproduce the exact second virial coefficient of the binary mixture. In practice, when a specific mixture is the focus, the values of ϵ_{AB} and σ_{AB} are fitted to some mixture property.

For metal mixtures where EAM potentials are used, a similar approach is taken. Johnson, and co-workers have provided generalized EAM potentials for 16 metals and their mixtures. The pure metals considered by Zhou et al are Cu, Ag, Au, Ni, Pd, Pt, Al, Pb, Fe, Mo, Ta, W, Mg, Co, Ti, and Zr.

Perturbation theory for mixtures

Perturbation theory for mixtures requires two ingredients. First, of course, one needs the interatomic potential function for the mixture. This was already described in the previous subsection. Second, one needs a reference fluid for the mixture of interest. This reference fluid is the hard sphere mixture. Then for each species a hard sphere diameter is determined using the WCA criterion. The free energy of the N-component hard sphere mixture is obtained from an accurate equation of state due to Mansoori and Leland. The $N(N+1)/2$ distinct radial distribution functions for the hard sphere mixture are usually obtained from the Percus-Yevick approximation, and used in integrals to obtain the attractive part of the energy and pressure. Again, a strict mean field theory results when one sets $g_{ij}(r) = 1$ for all combinations of i and j.

van der Waals one-fluid theory

This is an example of conformal solution theory, an approach that maps the fluid mixture at density ρ and temperature T onto a pure fluid characterized by a size parameter σ_0 and energy parameter ϵ_0, at some corresponding density and temperature. The theory hinges on finding a mapping that works. Van der Waals one-fluid theory has been very successful in this respect. It defines the following size and energy parameters

$$\sigma_0 = \sum_i \sum_j x_i x_j \sigma_{ij} \tag{3.0.34}$$

$$\epsilon_0 = \sigma_0^{-3} \sum_i \sum_j x_i x_j \epsilon_{ij} \sigma_{ij}^3, \tag{3.0.35}$$

where x_i denotes the molefraction of species i, and the cross terms σ_{ij} and ϵ_{ij} obtained using the Lorentz-Berthelot rules. With these in hand one then approximates the $g_{ij}(r)$'s by that of the equivalent pure fluid. The actual approximation consists of

$$g_{ij}(r/\sigma_{ij}; \rho, T, \mathbf{x}) \approx g_0(r/\sigma_0; \rho\sigma_0^3, kT/\epsilon_0), \tag{3.0.36}$$

where $\mathbf{x} \equiv (x_1, x_2, ..., x_{N-1})$ denotes the composition vector of the $N-$component mixture.

CF-DFT of mixtures

The extension of DFT from pure fluids to mixtures contains two aspects. The attractive contribution is straightforward, and simply requires mixed coefficients for the attractive part of the interaction potential. The treatment of the reference fluid, a hard sphere mixture, is challenging, but has been made straightforward by Rosenfeld who developed the so-called fundamental measure theory [58]. Thus, the CF-DFT of liquid mixtures is now as straightforward as that of pure fluids, and can be readily used to generate surface tensions as a function of composition.

Dynamical Properties of liquid metals

Two dynamical properties are required in the description of reactive wetting problems, namely viscosity and diffusion. The viscosity, η, is a scalar quantity (for liquid metals) that depends on temperature, density and composition (T,ρ, and $\mathbf{x}$), and is needed at the continuum level to describe the flow of liquids. To describe multicomponent mass transport requires many Maxwell-Stefan (MS) diffusion coefficients $\mathcal{D}_{ij}$ that are also functions of the state point, i.e., T,ρ, and $\mathbf{x}$.

In this section, we will address how the viscosity and the MS diffusivities can be obtained. We use *equilibrium* techniques, such as the Green Kubo relationships, to calculate Onsager

coefficients and MS diffusivities. Such quantities apply to mass transport problems that involve the dynamic behavior of systems *close* to equilibrium. However, the conditions encountered in metal joining, where rapid heating takes place, and sudden contacts are formed (e.g., between hot liquid metals and cold solid substrates), may in fact constitute *large* deviations from equilibrium. Extending the linear-response approach to situations far from equilibrium is currently the only viable strategy available. At this point there exists no complete theoretical framework that could treat the large deviations, although there is much work in this developing field. However, MD simulations can be used to make an assessment of the limitations of the linear-response regime. That is, within an MD simulation one can study the dynamical behavior of large gradients and large external fields (such as in field-driven nonequilibrium MD (NEMD)) [59] and directly compare the results with the linear-response approach.

The driving force for diffusion of species i is the spatial gradient of its chemical potential[3], i.e. $\nabla\mu_i$. The transport equation is,

$$-\beta\nabla\mu_i = \sum_{j=1,j\neq i}^{m} \frac{x_j(u_i - u_j)}{\mathcal{D}_{ij}}, \tag{3.0.37}$$

where $\beta = 1/kT$ and k is Boltzmann's constant. The velocity of species i is denoted by u_i. We see that $1/\mathcal{D}_{ij}$ acts as a friction coefficient, describing the friction between species i and j. It is immediately clear that for multicomponent mixtures a large number of MS diffusivities $\mathcal{D}_{ij}(\mathbf{x})$ are required, as many as there are distinct pairings of components, i.e. $m(m-1)/2$. Note that $\mathcal{D}_{ij} = \mathcal{D}_{ji}$.

The MS diffusivities are convenient quantities as their values are independent of the reference frame. Experimentally, these quantities are difficult to obtain directly because chemical potential gradients can not be measured directly. In general, the diffusivities are needed as a function of composition, and thus a large data set is required to address mass transport problems. Obtaining diffusivities from molecular dynamics simulations is comparatively straightforward, although sometimes it can be costly in computer time. However, if one seeks to limit the brute force MD approach it is crucial to explore predictive methods for the MS diffusion coefficients. This we will address in the sections below, where we outline a strategy that minimizes the amount of MD simulation to the simpler problem of determining self diffusion constants in multi-component mixtures.

Mutual Diffusion Coefficients of liquid metals mixtures. Enskog Theory

Following the success of Enskog theory of transport coefficients of the pure hard sphere limit first presented in 1922 [60, 61], it took many decades before the extension to the binary and later multicomponent hard sphere fluid was attempted by Thorne and, in 1971, by Tham

[3]There are only $m-1$ independent chemical potential gradients, as they satisfy the Gibbs-Duhem relationship.

and Gubbins [61, 62]. Lopez de Haro et al. [63] subsequently derived explicit expressions for the transport coefficients of heat and matter, based on the so-called revised Enskog theory. Later, Erpenbeck performed MD simulations for an isotopic binary mixture, and provided an excellent review of the subtle underlying issues in 1986 [64].

At this point in time there does not appear to be a generalization available of the work of Protopapas et al [54] that was described earlier, for pure metals. In other words, there exists currently no mapping strategy of the mutual diffusion coefficients of a metal mixture onto an appropriate hard-sphere mixture. Therefore, this would appear to be a worthwhile direction to explore.

A metal mixture could be characterized by the equivalent hard sphere diameters $\sigma_i(T)$ of the pure metals. The cross interactions between species i and j involves an prescription for σ_{ij}. For an additive mixture we expect that $\sigma_{ij} \approx (\sigma_i + \sigma_j)/2$, c.f., equation 3.0.33. In that case the metal mixture can be mapped onto an additive hard-sphere mixture of equivalent density, and the existing Enskog predictions of Lopez de Haro [63] couid be used. If the mixture is nonadditive, one could consider a mapping onto a nonadditive hard-sphere mixture, i.e., $\sigma_{ij} = (1 + \alpha)(\sigma_i + \sigma_j)/2$, with α positive (preferring like neighboring spheres) or negative(preferring unlike neighbors). This would require MD results and Enskog theory to be generalized to nonadditive hard-sphere mixtures. This is straightforward for MD, but might be more involved for the revised Enskog theory.

Mutual Diffusion Coefficients of liquid metals mixtures

Recently Liu, Vlugt and Bardow (LVB)[65] have introduced a robust method for predicting $\mathcal{D}_{ij}$, from self-diffusivities, $D_{i,self}$. The predictive method consists of multicomponent Darken equation derived from linear response theory and Onsager's relations. The result is

$$\mathcal{D}_{ij}(\mathbf{x}) = \frac{D_{i,self}(\mathbf{x}) D_{j,self}(\mathbf{x})}{D_{mix}(\mathbf{x})}, \tag{3.0.38}$$

with

$$D_{mix}(\mathbf{x}) \equiv \sum_{i=1}^{m} \frac{x_i}{D_{i,self}(\mathbf{x})}. \tag{3.0.39}$$

Equation 3.0.38, together with 3.0.39, is referred to as the multicomponent Darken equation, as it generalizes the familiar Darken equation for binary mixtures[4]. .

Equation 3.0.38, requires the self-diffusion coefficients, $D_{i,self}(\mathbf{x})$, of all the components in a multicomponent system of composition $\mathbf{x}$. To avoid this effort LVB introduced the

[4]For m=2, the multicomponent Darken equation reduces to the traditional Darken equation, $\mathcal{D}_{ij}(\mathbf{x}) = x_i D_{j,self}(\mathbf{x}) + x_j D_{i,self}(\mathbf{x})$

following approximation

$$D_{i,self}(\mathbf{x}) \approx \left(\sum_{j=1}^{m} \frac{x_j}{D_{i,self}^{x_j \to 1}} \right)^{-1}, \tag{3.0.40}$$

where $D_{i,self}^{x_j \to 1}$ is the infinite-dilution self-diffusion coefficient of species i in a binary mixture of i and j. When $j = i$, $D_{i,self}^{x_j \to 1}$ becomes te pure component self-diffusion coefficient (note that the summation in equation 3.0.40 includes the term $j = i$.)

The multicomponent Darken equation combined with the approximation 3.0.40 is referred to as the *predictive Darken-LVB* equation.

The approach outlined above is not the only approximate approach in the literature. For instance, the Vignes-LBV equation[65] is also based on pure component data together with binary mixture data

$$\mathcal{D}_{ij} = (D_{j,self}^{x_i \to 1})^{x_i} (D_{i,self}^{x_j \to 1})^{x_j} \prod_{k=1, k \neq i,j}^{N} \left(\frac{D_{i,self}^{x_k \to 1} D_{j,self}^{x_k \to 1}}{D_{k,self}^{x_k \to 1}} \right)^{x_k}. \tag{3.0.41}$$

Here $D_{i,self}^{x_j \to 1}$ is the infinite-dilution self-diffusion coefficient of species i in a binary mixture of i and j, while $D_{k,self}^{x_k \to 1}$ is the pure component self-diffusivity.

Viscosity of liquid metals mixtures

The viscosity of liquid mixtures, $\mu = \mu(T, \rho, \mathbf{x})$, is a scalar quantity that can be calculated using the Green-Kubo expressions, or alternatively from a $NEMD$ simulation. Predictions based on the *pure* metals can be generated using a linear relation of the logarithm of the viscosity, as suggested by Arrhenius in 1887[66],

$$\ln\ \eta_{mix} = \sum_i x_i\ ln\ \eta_i. \tag{3.0.42}$$

Grunberg and Nissan [67] suggested an extension of this expression to account for observed deviations

$$\ln\ \eta_{mix} = \sum_i x_i\ ln\ \eta_i + \sum_i \sum_j x_i x_j d_{ij}, \tag{3.0.43}$$

where the constant d_{ij} can be positive or negative.

Eutectic mixtures

A eutectic system is a mixture (alloy) of a unique composition. It has a lower freezing point than any other composition of the same components. Thus, for the binary alloy of Sn and Pb, the freezing temperature is much below that of both the pure metals, see figure B.1.

In our section on diffusion coefficients of liquid metals, we described the Darken-LVB prediction, which is based on the self diffusivities $D_{i,self}^{x_j \to 1}$ at the infinite-dilution self-diffusion coefficient of species i in a binary mixture of i and j at the same p and T. Its is clear that for a eutectic liquid mixture this approach breaks down in a serious fashion. This is because a mixture at infinite dilution and the *same* T might very well be a solid, or a combination of solid and a specific composition liquid mixture (of non infinite dilution character). Note that the equivalent hard sphere approach that was described in a previous section does not not suffer from this problem, as the temperature only enters through the description of the equivalent hard-sphere diameter $\sigma(T)$, and the hard sphere fluid phase diagram is only a function of density.

Although the eutectic mixture presents a problem for some approximate methods, such as the Darken-LVB prediction, the dynamic information (i.e., diffusivities and viscosity) can always be obtained from an MD simulation.

Lastly, a preliminary study of obtaining nonequilibrium tensions has been performed, and will be discussed elsewhere.

Chapter 4

Experiments: Diffusing Wave Spectroscopy

In previous chapters aspects of the relevance of diffusion, models for diffusion, and obtaining diffusion coefficients in a number of systems (applications) that are inhomogeneous or heterogeneous (mulitcomponent) have be examined. Here a return is made to the archetypal system of colloidal diffusion at high concentration to examine experimental techniques developed to gain physical insight into these systems. Specifically, diffusing-wave spectroscopy is discussed.

Diffusing-wave spectroscopy (DWS) is one of the only experimental methods that exist for measuring diffusion coefficients of particles in highly concentrated, turbid samples. Here, a diffusing wave spectrometer was designed and built. To verify the setup and technique, its ability to measure both the diffusion coefficients of particles in dilute suspensions and also bubble size and rearrangements in Gillette foamy shaving cream were tested. In both of these cases, the expected behavior is known. Finally, this method was used to measure the diffusion coefficients of particles in concentrated suspensions where the particle diffusion was expected to be non-Fickian.

Background

Diffusing wave spectroscopy (DWS) extends the theory utilized in dynamic light scattering (DLS) to multiple scattering samples such as concentrated suspensions [68, 69, 70, 71], foams [72, 73], light scattering surfactant solutions [74, 75], and emulsions [76, 77, 78]. Furthermore, under common experimental conditions particle motions on the order of nanometers, much less than the particle radius, can be detected [79, 80].

Both DLS and DWS detect the intensity fluctuations that arise when coherent light is passed through and scattered by a colloidal sample. In both cases, the temporal fluctuations are due to scattering from moving particles; consequently, the temporal autocorrelation function of the intensity can be related to the diffusion coefficient of the scatterers.

A typical experimental setup is shown in Figure 4.1. Coherent light from a laser is polarized and expanded to impinge on a sample. Within the sample, the light is scattered in

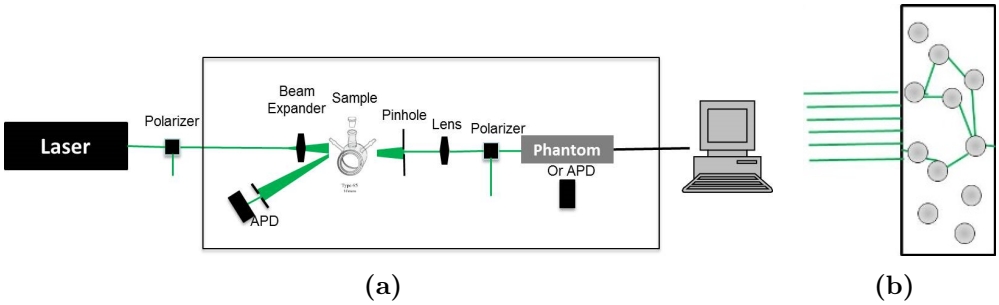

Figure 4.1. (a)Diffusing wave spectrometer experimental setup; (b) Illustration of light paths through a particulate suspension

multiple events before it passes from the cuvette and is collected in both the transmission and backscatter geometries. Any one speckle that is detected on the cuvette surface is produced from many different possible scattering paths scattering from many different particles (Figure 4.1), so the light direction is randomized and the angle of the two detectors does not matter to the measurement. This is one distinguishing feature of DWS as compared to DLS where the light is assumed to only scatter once in a dilute medium and the angle of the detected scatter pattern contains useful information. A change in the scattering intensity is produced when the path of light through the sample changes by at least one light wavelength, λ. Since a photon can scatter $> 10^4$ times in a DWS experiment, this means that each individual scatterer only has to diffuse a small distance for the change to be detectable [80].

Experimentally, the temporal autocorrelation function g_2 of a speckle of scattered light of intensity I is calculated as

$$1 + \beta g_2(t) = \frac{\langle I(t=0)I(t)\rangle}{\langle I(0)\rangle^2}. \tag{4.0.1}$$

The experimental parameter β is defined so that $g_2(0) = 0$.

The speckle intensity autocorrelation function g_2 is related to the scattered electric field autocorrelation function g_1 through the Siegert relation

$$g_2(t) = |g_1(t)|^2. \tag{4.0.2}$$

The speckle intensity measurements are related to the particle diffusion coefficients by fitting the measured g_1 data to the expected functional form of g_1. To determine the expected decay behavior of the autocorrelation function g_1, the light path through the sample is modeled as a random walk through a slab of thickness L. Each step length is known as l^*, the transport mean free path, or the average distance across which the light path direction is randomized. In the case where L is much greater than l^*, meaning that the light scatters many times before leaving the sample, the diffusion approximation can be used to describe the light density U through the slab with a diffusion coefficient for the light D_L

$$\frac{dU}{dt} = D_L \nabla^2 U. \tag{4.0.3}$$

By assuming an initial condition describing an instantaneous light pulse at a distance $z_0$within the sample $U(z, t = 0) = U_0\delta(z - z_0, t = 0)$, and boundary conditions requiring that the net flux of light at both slab faces is zero for $t > 0$, the following expression is obtained for the autocorrelation function of light transmitted through the slab

$$g_{1,t}(t) = \frac{\frac{\frac{L}{l^*}+\frac{4}{3}}{\frac{L}{l^*}+\frac{2}{3}}\{\sinh(\frac{z_0}{l^*}\sqrt{\frac{6t}{\tau}}) + \frac{2}{3}\sqrt{\frac{6t}{\tau}}\cosh(\frac{z_0}{l^*}\sqrt{\frac{6t}{\tau}})\}}{(1+\frac{8t}{3\tau})\sinh(\frac{z_0}{l^*}\sqrt{\frac{6t}{\tau}}) + \frac{4}{3}\sqrt{\frac{6t}{\tau}}\cosh(\frac{z_0}{l^*}\sqrt{\frac{6t}{\tau}})} \tag{4.0.4}$$

For a detailed derivation of this equation, see [81]. The time constant τ describes the time required for a scatterer with diffusion coefficient D to move one optical wavelength λ

$$\tau = \frac{1}{k_0^2 D} = \frac{\lambda^2}{4\pi^2 D}. \tag{4.0.5}$$

This definition is useful only if the diffusion coefficient is constant for all observation time lengths. If not, the time constant can be redefined in terms of the mean square distance that the particles have traveled, $\langle \Delta r^2 \rangle$

$$\tau = \frac{\lambda^2 t}{\langle \Delta r^2(t) \rangle (\frac{L}{l^*}) 4\phi^2}. \tag{4.0.6}$$

A good approximation for the distance z_0 is l^* and t is most often much greater than τ, leading to a simplification of the transmission autocorrelation function

$$g_{1,t}(t) = \frac{\frac{L}{l^*} + \frac{4}{3}\sqrt{\frac{6t}{\tau}}}{(1 + \frac{8t}{3\tau})\sinh(\frac{L}{l^*}\sqrt{\frac{6t}{\tau}}) + \frac{4}{3}\sqrt{\frac{6t}{\tau}}\cosh(\frac{z_0}{l^*}\sqrt{\frac{6t}{\tau}})} \tag{4.0.7}$$

This function is nearly an exponential decay with a decay time of $\tau(l^*/L)^2$. The decay time can be understood by recognizing that (l^*/L) is equal to the number of random walk steps across the width of the cuvette and τ is the time that it takes the light pathlength to change by one laser wavelength.

The two unknowns in this equation are l^* and τ. The transport mean free path l^* can be estimated directly knowing the particle concentration and index of refraction of both particles and solvent using Mie theory in the specialized case of monodisperse particles of very low concentration. In highly scattering media such as those used in DWS applications it must instead be experimentally discovered by a second measurement of the backscattered light.

The backscattering experiment is treated with similar analysis and assumptions as compared to the transmission experiment, leading to an approximation for the backscatter autocorrelation function

$$g_{1,b}(t) = \frac{\exp -\frac{z_0}{l^*}\sqrt{\frac{6t}{\tau}}}{1 + \frac{2}{3}\sqrt{\frac{6t}{\tau}}} \tag{4.0.8}$$

For most experimental setups, this expression can be simplified even further to

$$g_{1,b}(t) = \exp -\gamma\sqrt{\frac{6t}{\tau}} \tag{4.0.9}$$

The parameter γ is found experimentally to vary between 1.5 and 2.7 and is constant for a given polarization state and particle/solvent system.

In summary, DWS experiments obtain $g_{2,b}(t)$ and $g_{2,t}(t)$ by measuring the intensity of a speckle in either transmission or backscatter geometries. Once normalized and transformed to $g_{1b,t}$ using the Siegert relation, the autocorrelation data is compared to expected forms of the autocorrelation functions. By fitting the data in this way, parameters l^* and τ are obtained. Diffusion coefficient information is encapsulated in the parameter τ.

Experimental Apparatus

A diffusing wave spectrometer was constructed using a Coherent Verdi V6 laser (532 nm) as a light source. The laser beam is first expanded to a diameter of approximately 1 cm before it impinges upon the sample. Various cuvettes are available, ranging in thickness from 1 mm-10 mm in thickness. Some are thermally controlled using a water circulator (Jalabo, Allentown, PA). Cuvettes were purchased from Starna Cells (Atascadero, CA). Both backscattered and transmitted light are collected using silicon avalanche photodetectors (APD110A, Thor Labs), and the signals are then collected using either a National Instruments DAQ or an Agilent Oscilloscope (DPO7254). A LabVIEW routine was written to process the photodetector data and calculate the autocorrelation functions for both measurements. For samples that do not change with time, the LabVIEW routine is written to collect and average multiple autocorrelation measurements in order to reduce noise. A schematic of this setup is shown in Figure 4.1.

Typical measurements are obtained using a laser power less than 0.75 W and data collection lag times as low as 10^{-7}s. Each measurement contains up to $500,000$ points.

Scoping Experiments

To verify the efficacy of the home built diffusing wave spectrometer at measuring particle diffusion rates, a series of scoping experiments are performed. Solutions of various viscosities containing monodisperse particles are created. The viscosity of each suspension is predicted from the liquid composition, the sedimentation rate of particles through the liquid, single particle tracking, and finally DWS. The last two measurements are of the diffusion coefficient of particles in the liquid, which is then used to infer the viscosity assuming that the particles move through pure Brownian motion.

The composition of each solution is shown below in Table 4.1, showing that the range of viscosities explored is between 4.2-755 cP. Glycerol and water solution viscosities are estimated at 25°C [82](Segur and Oberstar, 1951) and 50°C [83] based on their composition, although pure glycerol is hydroscopic so the true concentration of water in the glycerol is unknown. UCON polyalkylene glycol oil (Dow Chemical, Midland MI) is also used as a high viscosity fluid. Added to each solution is 1 vol% monodisperse silica (Alfa Aesar, 1μm in diameter).

Table 4.1. Solutions of different viscosities used for scoping experiments

Solution	Composition	Refractive index	μ cP (20°C)	μ cP (50°C)
12	90 wt% glycerol + water	1.458	249	52.4
13	85 wt% glycerol + water	1.450	116	28.8
14	75 wt% glycerol + water	1.435	35.7	11.3
15	60 wt% glycerol + water	1.412	10.2	4.2
16	75-H-1400 UCON oil	1.4655	755	
17	75-H-450 UCON oil	1.4653	213	

Upon adding silica particles to each water/glycerol solution, it is discovered that the silica is hardly visible in the 75 wt% glycerol solution (Figure 4.2). Silica has an expected index of refraction of $n_{silica} = 1.54$, which is significantly different than the expected refractive index of all of the solutions used. It is concluded that the silica particles are porous, which alters their refractive index to 1.43. Because of this, the light scattering of the 75 wt% glycerol solution was insufficient for DWS measurements. Porosity is not unexpected for monodisperse colloidal silica fabricated using certain methods [84].

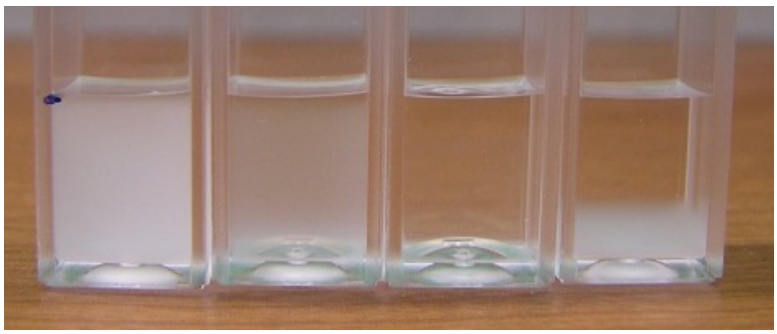

Figure 4.2. Sedimentation experiment for solutions (left to right) 12-15. Silica is hardly visible in Solution 14, the 75 wt% glycerol solution.

Sedimentation

A sedimentation experiment is performed for 1 vol% silica in water (pH = 8.5) to determine the particle density. To quantify the settling velocity, cuvettes are filled with the solution and images of the falling silica/water interface are taken periodically. For dilute monodisperse particles of radius r and density ρ_P settling in a liquid of density ρ_L and viscosity μ the Stokes settling velocity V_s is

$$V_s(t) = \frac{2gr^2(\rho_P - \rho_L)}{9\mu} \tag{4.0.10}$$

Because the particles are known to be dilute, this equation neglects any effects of particle concentration on the sedimentation rate that could arise due to backflow of solvent or particle interactions. To maintain these assumptions, the sedimentation rate is only measured for the initial decrease and not as the particles concentrate at the bottom of the cuvette.

Through this method, the density of the 1μm silica particles is found to be $2.2g/cm^3$, which is 83% of the expected density of $2.65g/cm^3$. This is consistent with the conjecture that the particles are porous. Using the particle density found for the pure water case, the viscosity of the glycerol/water and UCON oil solutions are found. The measured viscosity is slightly higher than the predicted viscosity (Figure 4.5).

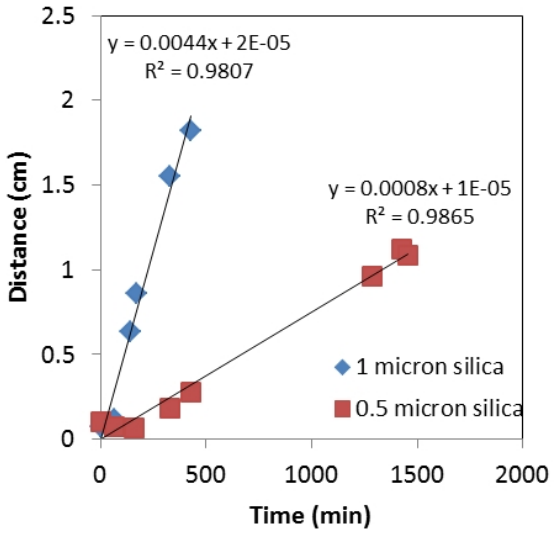

Figure 4.3. Sedimentation data for 1μm and 0.5μm silica particles in pure water

Single Particle Tracking Velocimetry

Single particle tracking velocimetry was also performed to measure the diffusion coefficient of the particles. Particle diffusion is recorded at $20x$ magnification using a Leica inverted microscope at 100 frames per second using a Phantom Miro camera (Vision Research, Wayne NJ). Particle locations are identified and linked into tracks with a modified single particle tracking routine [85] adapted by Blair and Dufresne for MATLAB [86].

Typical data for the average mean squared displacement of particle versus the observation time is shown in Figure 4.1. Overall, the MSD is linear with delay time. At short times, errors result in approximating particle displacements that are smaller than a pixel. Over long observation times, particles tend to drift out of the observation plane and can no longer be imaged. In the example shown, very few particles tracked longer than 10s, and errors in linking particle positions give erroneous estimations for the particle displacements.

Assuming that particle diffusion in dilute samples follows Stokes-Einstein behavior, the best fit line to the data is used to obtain the solvent viscosity

$$\langle \Delta x^2 \rangle = 4D_0 t = 4\frac{k_B T}{12\pi\mu r}t \tag{4.0.11}$$

For the data in Figure 4.1, the solvent was pure water with a known viscosity of 1 cP. Using a diffusion coefficient calculated using the above equation, the pink line was drawn. The data fits this prediction well. Particle tracking of silica particles in glycerol/water solutions gave viscosity values that were slightly higher than were predicted using the solvent composition, but well in line with the viscosity estimated using the sedimentation method (Figure 4.5).

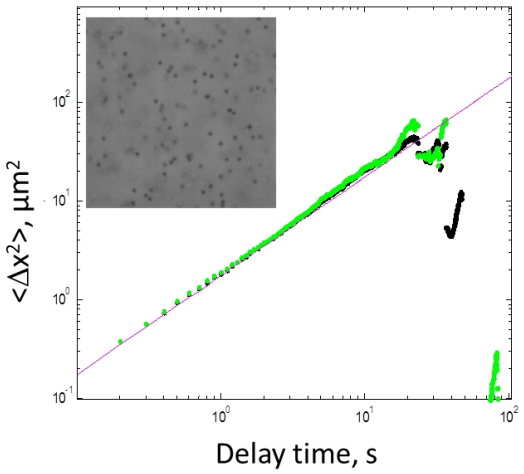

Figure 4.4. Average mean squared displacement of dilute 1μm polystyrene particles in water versus observation time for two separate data sets (green, black). The pink line gives the predicted behavior given the Stokes Einstein diffusion coefficient for the system. Inset: raw image of 1μm particles.

Diffusing Wave Spectroscopy

Diffusing wave spectroscopy measurements were performed using APD photodiodes as a backscatter detectors and a National Instruments data acquisition system. Up to 10^6 samples were collected at up to 10^6 Hz with a laser power of 1W spread over an approximate $1cm^2$ area.

Since this sample was not expected to change in time, multiple autocorrelation functions were calculated and then averaged together to reduce noise further. Backscatter measurements were analyzed using Equation 4.0.9 to obtain the time constant τ and the diffusion coefficient D using Equation 4.0.5. Once again assuming that the solutions were dilute, Equation 4.0.11 was used to find the solvent viscosity.

Initially, samples were contained in a 1 cm thick cuvette with no thermal control. However, glycerol and water solution viscosities are highly dependent on temperature, as shown in Table 4.1. After a typical DWS measurement was taken using a 1 W laser power impinging on a sample contained in a $1cm^2$ square cuvette, the temperature of the solution was 50°C. When the predicted viscosity of the glycerol/water solutions was adjusted for this warmer temperature, the agreement between the DWS measurements and the theoretical predictions is within the same error as the sedimentation and particle tracking methods (Figure 4.5).

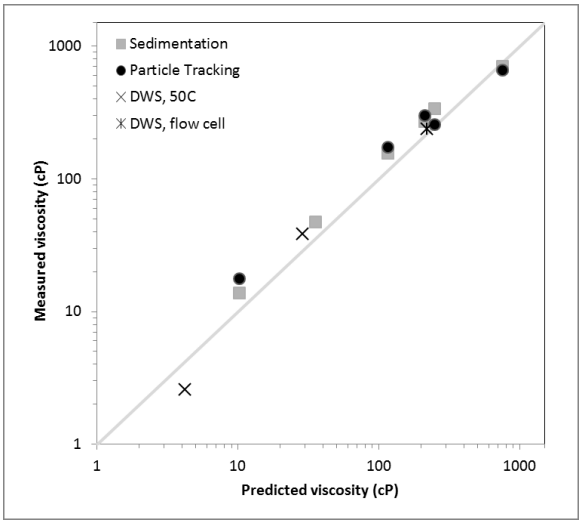

Figure 4.5. Viscosity of glycerol/water and UCON oil solutions as measured by different methods

A water cooled jacketed cuvette was employed to maintain the temperature of the suspension during the DWS measurement. This cuvette also has a transmission path length of 1 cm. Using this cuvette, the sample temperature was maintained at 22°C with a 1 W laser power. Once again, the sample diffusion coefficient was measured accurately (Figure **??**.

In general, the predicted Stokes-Einstein diffusion coefficient was verified for water/glycerol

mixtures and UCON oils ranging over three orders of magnitude of viscosity. In most cases, the predicted water/glycerol viscosity was slightly lower than what was experimentally measured. This may be because the hydrodynamic diameter of the silica particles was larger than the reported 1μm diameter, measured through scanning electron microscopy. The hydrodynamic radius of the silica would be different in the UCON oils, two of the highest viscosity solutions measured. Regardless of the predicted viscosity, the viscosities found through all three experimental methods were very consistent, implying that the DWS apparatus as built is effective at measuring the diffusion coefficient of these particles.

Diffusion of Highly Concentrated Particles

Introduction

One of the attractions of diffusing wave spectroscopy as a technique is the ability to observe particle diffusion in highly turbid samples or across very small distances. Both of these are required for probing highly concentrated particulate suspensions where the diffusion coefficient is likely be non-Fickian. Because very small particle motions can be detected, particle diffusion coefficients can be measured over orders of magnitude in delay time. The technique was demonstrated for various concentrations of silica particles in water.

Methods

Aqueous dispersions of 0.5μm diameter monodisperse silica particles (Alfa Aesar) were created for concentrations ranging from 1 - 40 vol%. Concentrations were calculated based on the cited 0.5μm diameter for the ceramic solid size. The density of the silica was measured through the sedimentation methods previously described to be $2.0 g/cm^3$. Particles were electrostatically stabilized in Milli-Q (Millipure) purified water which was buffered at pH 8.5 using a weak potassium hydrogen phthalate (KHP) and sodium hydroxide buffer. Although silica is more dense than water, the sedimentation speed of these particles was estimated to be 100 times slower than the diffusion time. The Brownian time, τ_B, for these particles is estimated to be $2.7x10^{-11}$ s, which is faster than the capabilities of the current DWS setup.

Backscatter and transmission diffusing wave spectroscopy measurements were made on the samples using 1 mm, 2 mm, and 5 mm cuvette path lengths. Measurements made with 5 mm cuvettes were thermally controlled to 21°C. Sample temperatures were measured at various laser powers to justify the lack of thermal control for thinner cuvettes. Without the laser, the sample temperature was 20.9°C. At 0.5 W of laser power, the temperature was 21.0°C. At 1 W of laser power, the temperature was 25°C. Therefore, each measurement was taken at or below 0.5 W of laser power. Most measurements were recorded at 10^6 Hz for 10^6 samples. Over fifty autocorrelation functions were averaged to reduce noise.

Results and Discussion

Backscatter autocorrelation functions are displayed in Figure 4.6 for 1% - 40% vol% silica solutions. As the concentration increased, more light was scattered backwards from the sample and the noise in the autocorrelation function decreased. In accordance with Equation 4.0.9, the autocorrelation function is approximately linear when plotted on a log scale versus $t^{1/2}$. Deviations from linearity occur at short delay times. These data derive from long path lengths of many scattering events in the sample, and the decay is due to light absorption during this process. At long times, the data becomes noisy. This is due to a lack of resolution in the intensity measurements afforded by the detectors and the oscilloscope. Further nonlinearities exist due to non-Fickian behavior of the particles.

An average diffusion coefficient over the experimental delay times was measured by fitting the backscatter autocorrelation function data to Equation 4.0.9. This average diffusion coefficient was then used to fit the transmission data for the parameter l^*. An example of this fit for a 1 vol% silica solution is shown in Figure 4.7. At low silica concentrations, the particle diffusion is expected to follow Stokes-Einstein behavior with one constant diffusion coefficient. Figure 4.7 is well fit by Equation 4.0.7 with one constant diffusion coefficient.

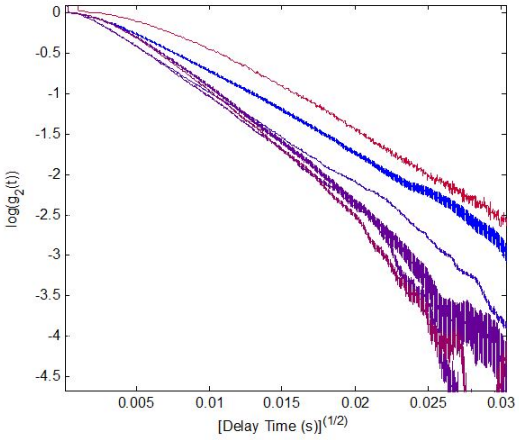

Figure 4.6. Backscatter autocorrelation function raw data for 0.5 ?m silica particles in 1% (red), 5%, 10%, 20% and 40 vol% (blue) concentrations. The slope of this line determines the average diffusion coefficient.

As the concentration of silica increases, the diffusion coefficient is not constant with observation time. To find a mean squared particle displacement for each delay time, the transmission equation was inverted for each autocorrelation measurement to find a value of τ for each delay time. The mean squared particle displacement was then found using Equation 6. These data are shown in Figure 4.8. At low particle concentration, the diffusion coefficient is very close to the Stokes-Einstein Do value of $9x10^{-13}m^2/s$. As the concentration increases and the particles begin to feel effects from their neighbors, the mean squared displacement

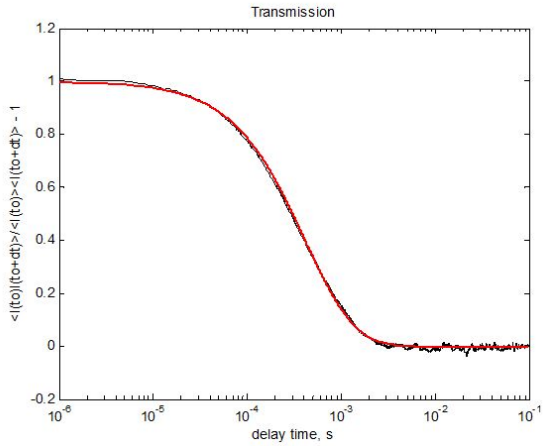

Figure 4.7. Transmission data (black) and fit to transmission data (red) for 1 vol% silica in water, 2 mm cuvette, 0.5 W laser power. $D = 8 * 10^{-13} m^2/s$

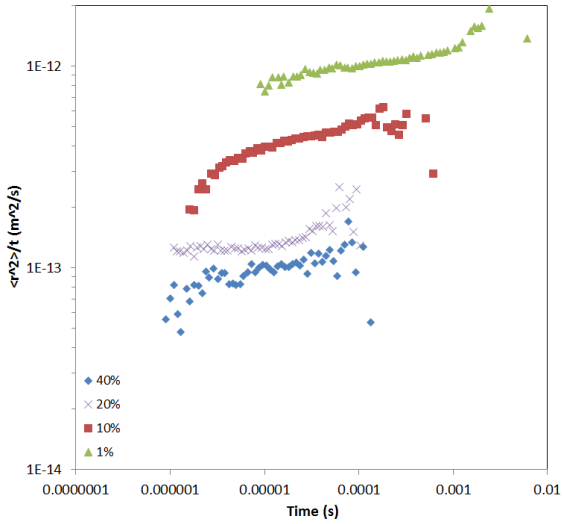

Figure 4.8. Mean squared displacement of various concentrations of silica particles

decreases as expected. According to predictions, the behavior of each of these suspensions should be characteristic of the constant diffusion rate plateau (as described in Chapter 2)). At low concentrations the mean squared displacement seems to increase slightly with time. This behavior is not predicted by hard sphere simulations, but could be caused by the measured mean squared displacement being a combination of both ballistic and diffusive motions.

Errors are introduced in these measurements from many sources. As particle concentrations increase, the intensity of the laser signal passing through the sample decreases and the data become noisier. As discussed earlier, data at fast and slow measurement times are unreliable due to light absorption and intensity resolution issues. Furthermore, this silica and water suspension is not a simple model system. The particles are not expected to act like hard spheres in the dilute buffer, and likely have a larger hydrodynamic radius than 0.5μm. The particles are also known to be porous, so likely scatter light more strongly than pure silica particles. This means that Mie theory cannot be used in this instance to predict l^* as was done in previous studies [81]. Instead, both l^* and the diffusion coefficient must be fit independently from two light scattering measurements, introducing more sources of error.

Foam Bubble Dynamics

Introduction

Wet foam bubble size and bubble dynamics are difficult to experimentally quantify since foams are fragile, mobile, and scatter light very well. Their opacity, derived from efficient light scattering, makes foams inaccessible to techniques such as optical microscopy yet ideal for diffusing wave spectroscopy. In a series of reports, Durian et al. have shown that DWS is an effective tool for determining foam bubble size as it changes with time, and also bubble rearrangement rates as the foam coarsens, cures, or dries [87, 88, 72, 73, 89]. In these studies, Gillette Foamy Regular shaving cream was used as a well-studied and reproducible foam with bubbles that are known to coarsen but not rupture. These observations are reproduced here in order to demonstrate the capability of the DWS apparatus for studying foams.

The theory for analyzing the light back and forward scattered from foams has many similarities to that for scattering through colloidal samples. The static transmission of light, T, through a non-absorbing foam of thickness, L, is roughly proportional to l*, the transport mean free path of light in the material ($T \approx 5l^*/3L$). Studies have shown that l^* is proportional, but not equal to, the bubble size. This implies that the scattering direction of the light is randomized after it passes through a defined number of interfaces (greater than one) [73]. To discover the proportionality constant, a, between T and the bubble diameter d_b, a second experimental technique such as optical microscopy must be used.

Analogous to DWS of particle suspensions, the timescales of the backscatter and transmission autocorrelation functions can be used to gain information about the bubble rearrangement rate. As previously discussed for particulate suspensions, Equation 4.0.7, a nearly exponential function with a decay time of $\tau(l^*/L)$, is used for understanding the transmission autocorrelation function. Equations 4.0.8 or 4.0.9, also nearly exponential with a decay time of $\tau^{1/2}$ are still valid for understanding the backscatter autocorrelation function. For foams, the characteristic time scale τ is the average time between bubble rearrangements at a point in the sample. If rearrangements of size r occur at a rate R per unit volume, then $\tau \approx 1/(Rr^3)$.

One complication with studying foams that does not exist in studying particulate suspensions is their nonergodicity. Because foams have heterogeneous, slow moving microstructures, averaging data over time for one location in the foam is not necessarily equivalent to averaging over the entire sample. This is a breakdown of the ergodicity assumption that was implicitly made in deriving Equations 4.0.1-4.0.9. Many experimental methods have been invented to spatially average data collection over a greater area of the sample. These include rotating or translating the sample, placing a second cuvette of known dynamics in front of the sample to randomize the light scattering, and to use a CCD camera to record a great number of speckles at the same time [79, 90]. In this report, transmission data from a CCD camera are compared to that using a photodiode.

Experiments and Results

To demonstrate that the home-built DWS setup is capable of studying foams, the Gillette Foamy Regular shaving cream experiments performed by Durian et al. were reproduced.

Since future experiments are planned for foams that are not easily removed from their container, a special disposable cuvette was developed to contain the foam samples. Here, a spacer was machined from acrylic to provide a known standoff distance for two 5 cm x 3 cm glass slides. Since pressure affects the development of most foams, a bead of grease is placed around the edges of the glass slides to prevent air escaping at the edges. Mold release can be applied to the inner surface of the spacer to reuse this part, whereas the glass slides are replaceable. This setup is illustrated in Figure 4.6.

Both transmission and backscatter intensity measurements were recorded at intervals over five hours. Backscatter intensity was recorded using an APD photodiode, whereas transmission measurements were taken both with an APD photodiode and a Phantom high speed camera (v9.1). Speckle patterns were initially averaged over a data collection period of ten seconds for each data point. The data collection time was adjusted as the foam aged. Camera videos were recorded at $4,000$ pictures per second with a 240μs exposure time. Videos were processed following the procedure of Viasnoff et al. [90]. Screenshots of the transmission speckle pattern recorded by the Phantom camera are shown in Figure 4.7.

Figure 4.8 shows the average transmission intensity over the data collection period of ten seconds determined both by the photodiode and also the average grayscale value in the camera images. Both the camera and the photodiode give analogous results. It is likely that the photodiode captures multiple speckles on one detector. To relate the average transmission intensity T to the bubble diameter d, the proportionality constant a would first have to be determined by optical microscopy. However, the qualitative behavior of the bubble coarsening can still be observed. Initially, for the first 20 minutes, the transmission intensity does not change significantly. After 20 minutes, the bubbles coarsen with time, the light does not need to travel through as many interfaces to transverse the cuvette, and the light intensity increases. This behavior is similar to what was reported by Durian et al. for the same system (Figure 4.8). Both data sets display a power law behavior in the bubble

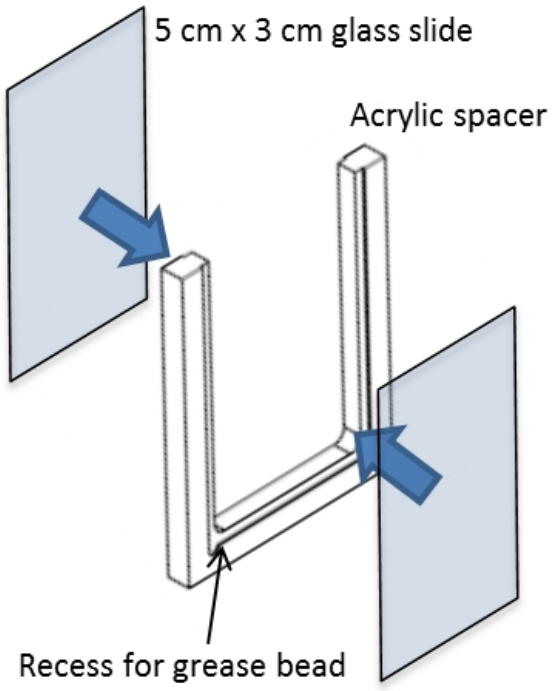

Figure 4.9. Specialized large cuvette developed to contain foam

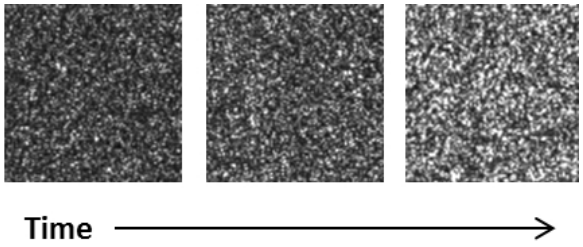

Figure 4.10. Example speckle patterns recorded by the Phantom camera

size over time. Here, $d \sim t^{0.41}$, whereas the previously published data reported $d \sim t^{0.45}$.

The bubble size evolution can independently be determined through the dynamic speckle data. Both the transmission and backscatter autocorrelation functions for the speckle intensity over time were calculated to find the parameters τ and $\Gamma = \tau(l^*/L)$. The backscatter data shows that over time the bubble rearrangement rate slows, also with power law behavior. By comparing τ and Γ, it is found that $d \sim t^{0.48}$, which is within the acceptable error of the measurement. Depending on the diffusion mechanism of air between bubbles, foam

coarsening rates range from $d \sim t^{0.33}$ - $t^{0.5}$.

The diffusing wave spectroscopy setup was able to find bubble size and coarsening rates as this simple foam aged over time. The measurements are uniquely interesting because they are characteristic of the entire sample instead of just near a cuvette wall. DWS measurements of more complex foams that rupture or drain would also be possible in the future. To improve the setup, it is desired to create a mechanism for heating the foam to various curing temperatures. Also, because in the previous study three measurements were taken of two unknowns, the coarsening rate and the bubble size, it may be possible to introduce another unknown, the refractive index of the foam liquid. In this way, curing foams could be studied.

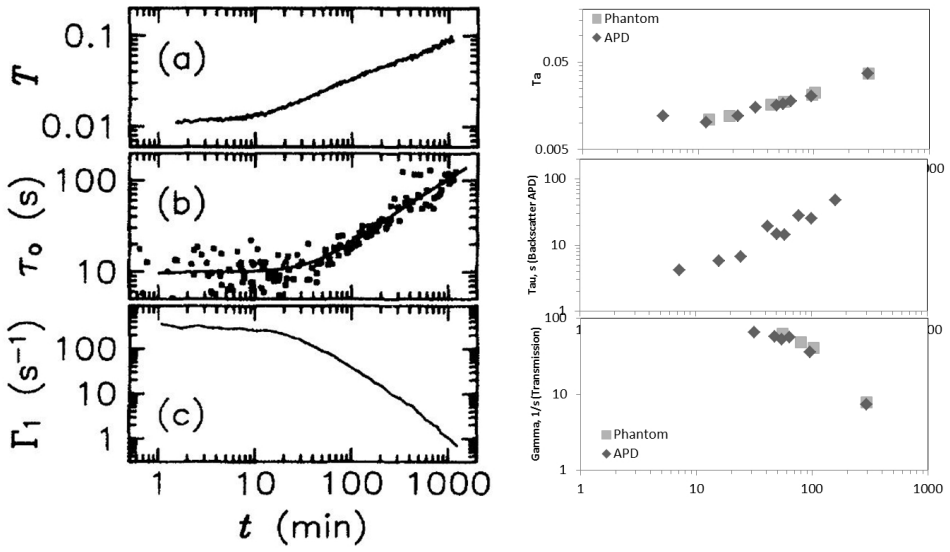

Figure 4.11. Gillette Foamy Regular DWS data versus foam age, comparing published data (Durian et al., 1991a) (left) to data from this report (right). (Top): Average static light transmission through a sample (Middle): Time scale ?, as determined through backscattering measurements. (Bottom): Transmission ACF decay time $\Gamma = (L/l^*)^2/\tau$

Chapter 5

Thermal Conduction in Particulate Materials

To this point it may have been difficult to stretch the imagination to see how generalized stochastic models can be relevant for general transport in heterogeneous materials. In this final chapter we begin to address this concern directly. We show how inhomogeneities in material microstructure introduce fluctuations at the meso-scale that in some limits are reminiscent of thermodynamic fluctuations within otherwise macroscopically homogeneous thermodynamic systems. These fluctuations due to random microstructures also provide a means of characterizing the aleatory uncertainty in material properties at the mesoscale.

Introduction

Heterogeneous materials such as carbon particle composites and ceramics play an important role in many energy related applications including electrodes for energy storage devices and catalytic devices for regulation of emissions from the combustion of fossil fuels. The key to better performing devices is detailed prediction and control of the bulk behavior of the component materials whether in terms of transport through the material during its end use or transport of the materials during the manufacturing process. Accordingly, numerical modeling and simulation plays a vital role in elucidating basic physical phenomena at a level of detail that is challenging to achieve experimentally, but that is complementary to such efforts. Hence, the task is to develop mathematical models and numerical algorithms that more faithfully represent the inhomogeneous structure and the physical processes that occur in this class of materials.

In particular, the nature of "conduction" (thermal, electrical, etc.) in heterogeneous materials is of fundamental importance. Assuming that classical diffusion is sufficient to describe the basic transport process, the challenge here is to accurately solve the diffusion equation on a complex, random microstructure with varying material properties. In the simplest case there may be two materials, e.g., solid particles of equivalent size and shape and identical material properties randomly dispersed in a second material of differing properties. Various theoretical approaches to this problem have been taken to determine the effective conductivity of the bulk material, or at least place upper or lower bounds on its

value (e.g., [99, 98, 104, 103, 105]). In addition, various modeling and simulation approaches have been taken to calculate effective properties of such systems (e.g., [111, 101]). For many applications, what is required for numerical simulations is a generalizable, robust, efficient, scalable, verifiable and validatable approach. Traditionally, for macroscale engineering design problems, computational continuum mechanics via the Finite Element Method (FEM) has provided just such an approach. In this chapter we report on a method to extend macroscale, continuum FEM to a mesoscale, heterogeneous material; we assess the performance of a technique to introduce and couple discrete particulate and continuous phases within a continuum FEM without requiring complicated and expensive body-fitted meshing routines.

Methods based on continuum mechanics approaches where particles are resolved discretely and the full thermal conduction problem is considered are widely discussed in the literature. Interest in these generalizable approaches is understandable since many systems are composed of irregular shaped particles and complex fluid matrix materials for which simultaneous solution of multiple, coupled macroscale balance equations is required. To improve the performance of coupled discrete-particle and continuum approaches the key is to introduce discontinuities accurately and efficiently in the continuum fields, e.g. [92, 93, 94, 95, 110]. Recently, a new approach termed a Conformal Decomposition Finite Element Method (CDFEM) was developed for this class of problems [91]. In CDFEM, a background, non-conformal mesh is decomposed into elements that conform to the particle interfaces. The particle interfaces are described with implicit functions, such as a level set. Nodes are added where the background mesh intersects the implicit surfaces. In this way, the approximation space is enriched, much like so-called eXtended Finite Element Methods (XFEM) [96, 97]. In fact, the discrete space introduced in CDFEM contains the space used in XFEM with Heaviside enrichment, since the XFEM space can be recovered by adding constraints on the nodes added in the conformal decomposition [91]. This property implies that the CDFEM accuracy is no less than that afforded by XFEM with Heaviside enrichment [102]. When applied to problems with Dirichlet boundary conditions, CDFEM is very similar to the recently proposed immersed finite element method [108, 109]. Both methods decompose the background mesh into conformal elements.

Previous work demonstrated CDFEM for static interfaces and showed that optimal rates of convergence were obtained for multiple fluid dynamics problems [91]. In the following, CDFEM is verified against known results for thermal conduction in particle packs and used to elucidate the role of fluctuations in conduction due to microstructural inhomogeneities.

Method

We consider ordered and random dispersions of mono-sized particles for various packing fractions below the close-packed limit. The results for ordered dispersions are obtained on unit cells in Simple Cubic (SC), Face-Centered Cubic (FCC), and Body-centered Cubic (BCC) arrangements. We create the random configurations of particles by performing a

Brownian dynamics (BD) simulation of purely repulsive colloidal spheres [46]. Particles are initially placed randomly without overlap in a periodic simulation domain with initial velocities drawn from a Maxwell-Boltzmann distribution consistent with a given temperature. The initial volume fraction of particles $\phi_2 = 0.1$. Subsequently, the simulation domain is shrunk to obtain the desired final volume fraction $0.1 < \phi_2 < 0.55$. The particles are then equilibrated for a million time steps; sufficient to ensure a well equilibrated sample. The inter-particle potential is purely repulsive and sufficient to prevent contact between spheres [47]; resulting in a fully dispersed suspension (i.e., non-contacting particles). A non-percolating contact network is an implicit assumption of the theories to which results shall be compared [101]. Snapshots of the particle configurations are then taken every time step for $\sim 100 - 1000$ time steps. This gives many particle configurations for statistical analysis at each volume fraction considered. In effect, if the BD simulation is considered to be a process for manufacturing particle dispersions we can begin to quantify the distribution of effective bulk properties that are characteristic of this dynamical process.

The equation solved on the particle dispersions is the steady-state heat equation or Laplace equation

$$\sigma_i \nabla^2 T_i(\mathbf{r}, t) = 0, \tag{5.0.1}$$

where $i = 1$ labels the interstitial region and $i = 2$ the particles. This equation is solved in the entire domain $\Omega = \Omega_1 \cup \Omega_2$ ($\Omega_2 = \cup_{j=1}^{N_p} \Omega_{part,j}$). At the interfaces of materials 1 and 2

$$\begin{aligned} T_1 &= T_2 \\ \sigma_1 \nabla T_1 &= \sigma_2 \nabla T_2, \end{aligned} \tag{5.0.2}$$

which corresponds to a "do-nothing" boundary condition.

We discretize the governing equation on a length scale smaller than the particle diameter ($d/\Delta x \sim 10$, typically) using a standard Galerkin Finite Element Method. We solve the resulting equations numerically via the Sierra–Aria [106] code developed and maintained at Sandia National Laboratories. The key to this direct numerical simulation approach is the manner in which a mesh conformal to the complex geometry of the random particle dispersion is created from a background structured mesh. To achieve this, a level set function is associated with each particle in the dispersion. Where the level set function changes sign is an interface between the particle and the interstitial or matrix material. Where this interface crosses an element of an initial structured mesh, the element is cut and decomposed as shown schematically in Figure 5.1. New nodes and corresponding degrees of freedom are introduced at the interface. This method performs well even though elements can be created with high aspect ratios [91, 102]; however, this is still a matter of ongoing analysis.

In order to determine the effective conductivity, a temperature gradient is established in the z-direction by applying a unit temperature on one of the z boundaries and zero

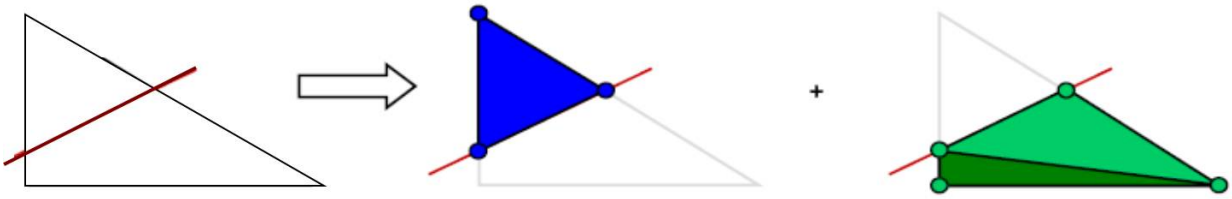

Figure 5.1. Schematic of conformal mesh decomposition algorithm due to interface intersecting element.

temperature on the other while periodic boundary conditions are applied in the remaining two directions. After solving the equations detailed above, the area-averaged flux through a plane perpendicular to the z-axis is found by

$$j_z = \frac{1}{A}\int_A \sigma_i \hat{\mathbf{n}}_z \cdot \nabla \mathbf{T}_i, \tag{5.0.3}$$

where $\hat{\mathbf{n}}_z$ is the unit normal of the plane in the z-direction. It was verified that this flux is relatively independent of the location of the plane, which is what would be expected for an isotropic dispersion of particles. With this flux calculated, the effective conductivity can be found as [111]

$$\sigma_e = \frac{j_z L}{\Delta T}, \tag{5.0.4}$$

where L is the thickness of system in the z-direction and the difference between the temperatures on the two z boundary planes is set to $\Delta T = 1$.

The following section details the simulation results.

Results

Verification of the technique described in the preceding section is accomplished by comparing the effective conductivity calculated from numerical simulations with rigorous analytical lower bound and approximations to the effective conductivity found in the literature [104, 100, 101]. Specific results on unit cells for order packs and random dispersion follow in the next subsections.

Ordered Dispersions

The systems considered here are unit cells so that only a minimal number of particles need to be resolved in the simulations. Once the particle configuration is given, the simulation is performed and the effective conductivity is determined as outlined above. In Figure 5.2 the effective conductivity, normalized by the conductivity of the matrix material, is plotted as a function of packing fraction for SC, FCC, and BCC unit cells. In this case, the ratio of the conductivities of the particle material to the matrix material $\alpha = 10000 \approx \infty$. Also plotted for comparison are the theoretical results of [104]. As can be seen, the comparison is very good even at the higher volume fractions where one might expect the poor quality elements that result from the CDFEM would have a greater impact on the calculations.

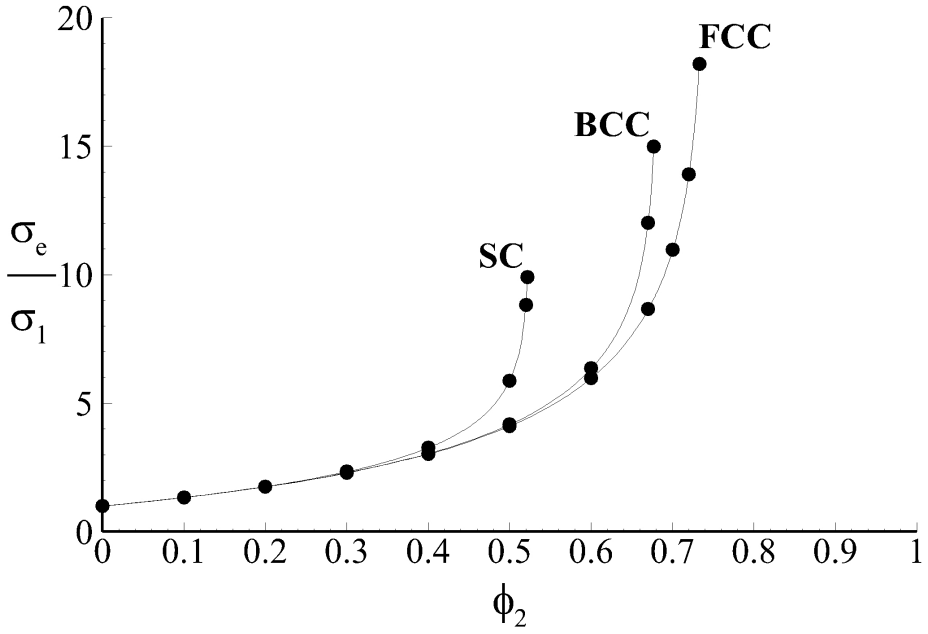

Figure 5.2. Theoretical (solid lines) and FEM simulations (points) of σ_{eff}/σ_1 for a simple cubic lattice with conductivity ratio $\alpha = \sigma_2/\sigma_1 = \infty$.

In the following subsection we consider systems of many particles in random configurations.

Random Dispersions

As described above, the random particle configurations considered were taken from BD simulations of mono-disperse, purely repulsive, soft spheres. The simulation domain was cubic of dimension $L = 10d$, where d is the particle diameter. The total number of particles

then varied with the volume fraction; however, there were typically $O(10^2)$ particles in a simulation. Also, the particle configurations are taken from the BD simulation every time step for 100 or 1000 time steps giving the potential to investigate the distribution of effective conductivities. Figure 5.3 shows typical results from the steady-state thermal conductivity simulations for volume fractions $\phi_2 = 0.3$ and 0.4 with $\alpha \approx \infty$. The color scale indicates the magnitude of the heat flux and the arrows indicate the direction. As can be seen, the heat flux tends to be greatest in regions of near contact between spheres due to their greater conductivity (the matrix is relatively insulating). These regions appear in chains of particles. As the volume fraction increases, some indication of increasing density and length of chains can be seen, but still no clear percolating structures are seen.

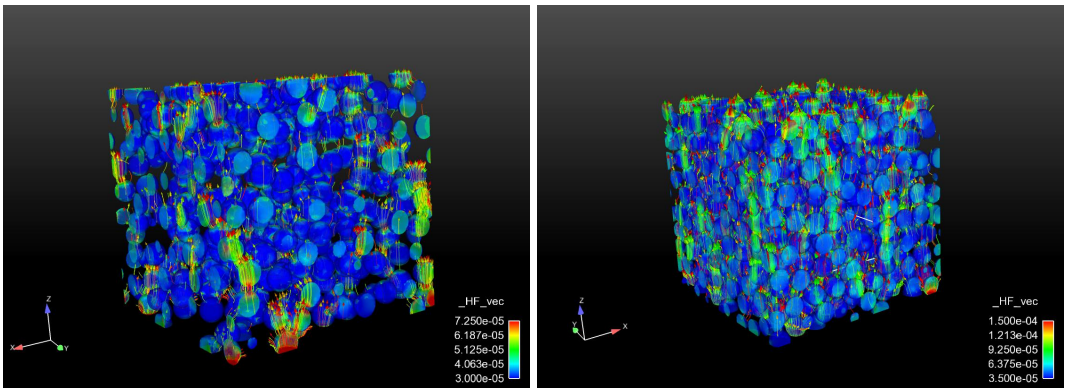

Figure 5.3. Simulation image of thermal conduction through random dispersions of $O(10^2)$ mono-disperse particles (a) $\phi_2 = 0.2$ (b) $\phi_2 = 0.4$. Color scale indicates magnitude of heat flux and arrow indicate direction of largest fraction of heat flux vectors (scaled and colored for emphasis).

In Figure 5.4a the quantitative results of the simulations are shown. Average effective conductivities for the particle configurations at each volume fraction are plotted and compared to the rigorous lower bound as well as an approximation based on assumptions about the particle microstructure [100]. Again, good agreement is obtained particularly below $\phi_2 \leq 0.45$. Although the value of the effective conductivity at the highest volume fraction $\phi_2 = 0.55$ compares well also, some care should be taken for this case. For these mono-disperse hard-sphere like systems an ordering transition is encountered at $\phi_2 \approx 0.45$. Hence, at $\phi_2 = 0.55$ significant ordering effects are present (compare value here with that of FCC in Figure 5.2).

In addition to average values of the effective conductivity, since multiple configurations consistent with Brownian motion of the particles in thermal equilibrium for each volume fraction are possessed, the distribution of conductivities for each volume fraction can be plotted. In Figure 5.4b the distribution of conductivities for $\phi_2 = 0.3$ is shown. Note that the distribution is not symmetric with a longer tail to larger effective conductivities. Similar

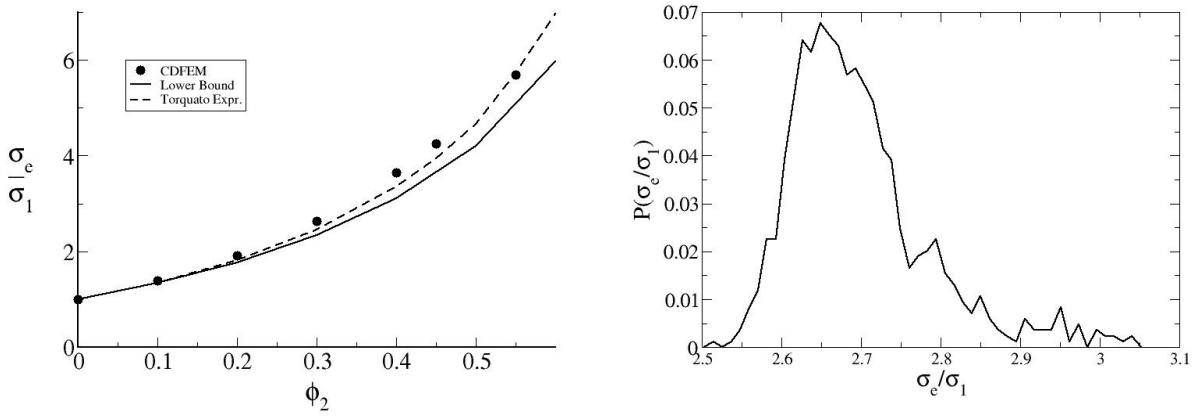

Figure 5.4. (a) Theoretical and FEM model predictions of σ_{eff}/σ_1 for a simple cubic lattice with conductivity ratio $\alpha = \sigma_2/\sigma_1 = \infty$; (b) Distribution of effective conductivities for volume fraction $\phi_2 = 0.3$.

results (particularly the asymmetric form of the distribution) have been seen before in two-dimensional and three-dimensional simulations for general conduction [112, 113, 114] type problems. For two-dimensional systems the width of the distribution has been shown, not surprisingly, to decrease as a function of system size [112, 113] and converge to a homogeneous macroscopic value in a manner reminiscent of thermodynamic fluctuation theory [115]. With respect to the last citation, note the role that a diffusion-like equation plays in the convergence of fluctuations to the thermodynamic (macroscopic, deterministic, homogeneous) limit.

Other interesting connections to these non-Gaussian, asymmetric distributions are found in extreme value statistics, generalized extreme value statistics and sums of correlated random variables, as well as fluctuations of global observables in complex correlated systems particularly finite-sized critical systems. However, we emphasize that a formal verification/convergence study remains to be performed on these systems, particularly for questions related to the thermal flux. To gain more insight into the nature of the statistics of the distribution of bulk conductivities we plot the increments of the conductivities.

Figure 5.6 shows the increments of the thermal conductivities (i.e., the change in thermal conductivity from one configuration taken from the BD simulation to the next $\Delta\sigma_e = \sigma_e(t + \Delta t) - \sigma_e(t)$). What is interesting to note here is the qualitative feature of sharp spikes in the increments which are of greater magnitude than the majority of the fluctuations. This is different from standard "white-noise" type fluctuations and gives an indication of the "volatility" in the effective conductivity perhaps due to the formation and break-up of conducting clusters of particles which produce configuration with relatively high bulk conductivity.

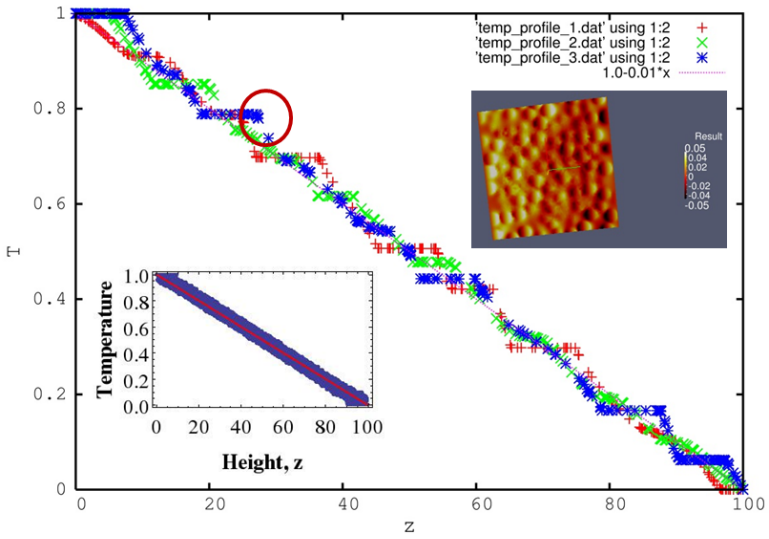

Figure 5.5. thermal fluctuation

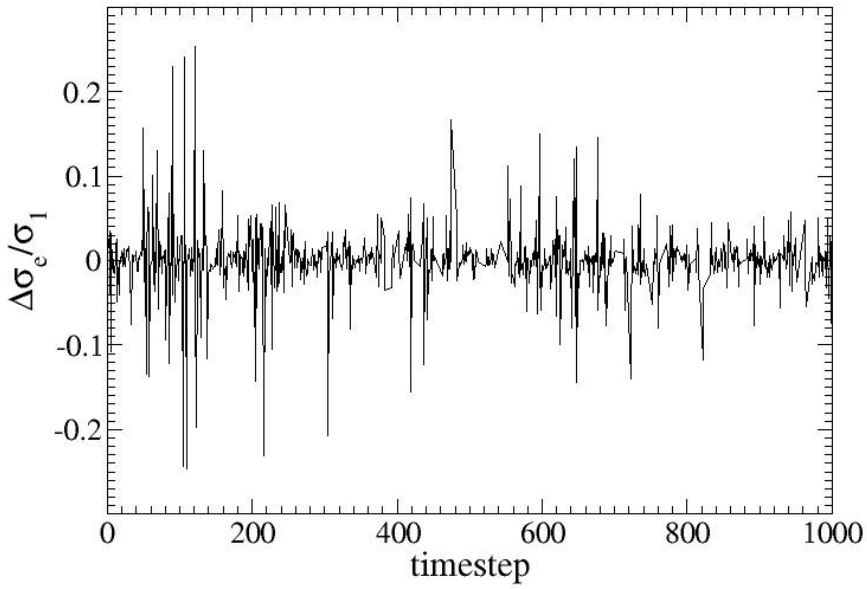

Figure 5.6. Increments of the effective thermal conductivity between successive snapshots taken from BD simulation of particles at $\phi_2 = 0.3$.

Yet another way to analyze the effective conductivity data is to histogram the change in thermal conductivity from one time step to the next. Interestingly, this gives a distribution that is relatively symmetric, but that appears to have tails that are broader than Gaussian; although more data and analysis is needed to obtain better statistics.

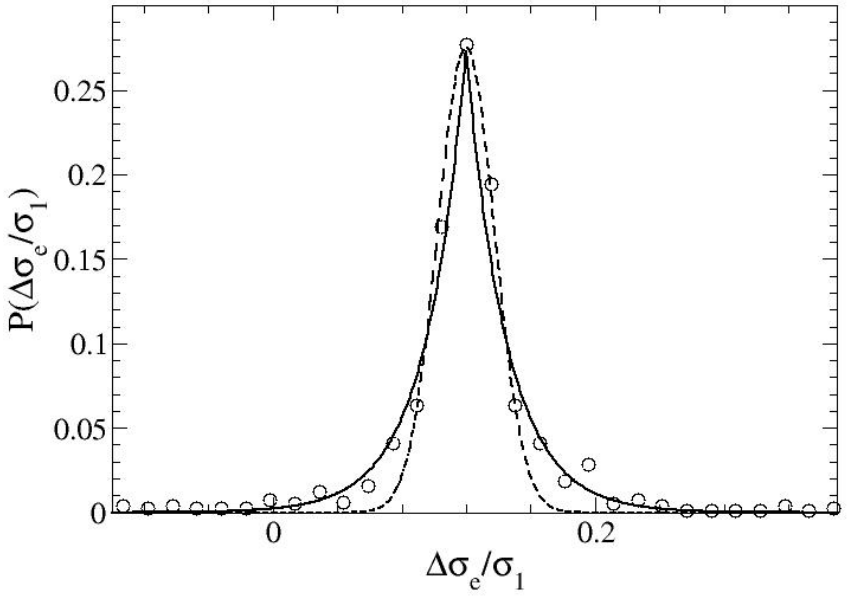

Figure 5.7. Distribution of increments in the effective thermal conductivity between successive snapshots taken from BD simulation of particles at $\phi_2 = 0.3$. For guides to the eye: solid line is an exponential distribution, which dashed is Gaussian.

Inhomogeneity and Fluctuations

In the previous section we considered the statistical information contained in the ensemble of configurations generated by a nominal manufacturing process. Here, for this nonequilibrium system, we are interested in the fluctuations in the temperature within a representative configuration. In a homogeneous system, for the boundary conditions given here, a linear temperature profile would result. In these inhomogeneous, system the temperature profiles are still linear on average with a slope equal to the bulk effective conductivity which is different from the conductivity of the constituent material. Examples of these temperature profiles can be seen in Figure 5.8.

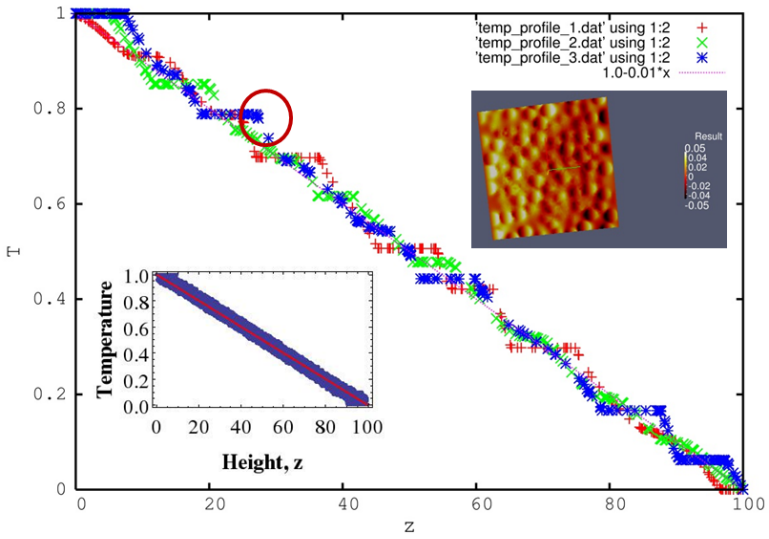

Figure 5.8. Temperature of three linear slices in the z-direction and $y - 0$, $x \pm L/4$. Lower right inset: temperature profile of all nodes plotted against z-coordinate

In Figure 5.9 the fluctuations ($\delta t = T - \langle T \rangle$) in the temperature of the nodes relative to the homogeneous, linear temperate profile. Also plotted are best fits of Gaussian distributions to the data. To first order a Gaussian distribution is not a terrible approximation; however some discrepancies can be seen in the tails. This may be due to sampling bias in that most of the nodes in the system are found near the interface of the particles and the matrix and are not uniformly distributed throughout the system.

Relevance to Manufacturing Process and Uncertainty Quantification

Finally, we show in Figure 5.10 the so-called exceedance probability for the effective conductivities. This is equivalent to the survival function or the complementary cumulative distribution function of the distribution of effective conductivities shown in Figure 5.8. Comparison is also made to Gaussian-type statistics as well as Gumbel statistics. Note the heavy (relative to Gaussian), exponential tail in the exceedance probability. The difference between the two statistics indicates an over population of large values of the bulk conductivity relative to Gaussian. This could have a significant impact on performance of a component and may indicate the need to better control the manufacturing process and hence microstructure to reduce the frequency of undesirable properties. Also, seen in Figure 5.10 are the data for three different volume fractions (20%, 20%, 40%) collapsed onto each other by appropriate rescaling. This is intriguing and brings to mind other work on the universality of fluctuations

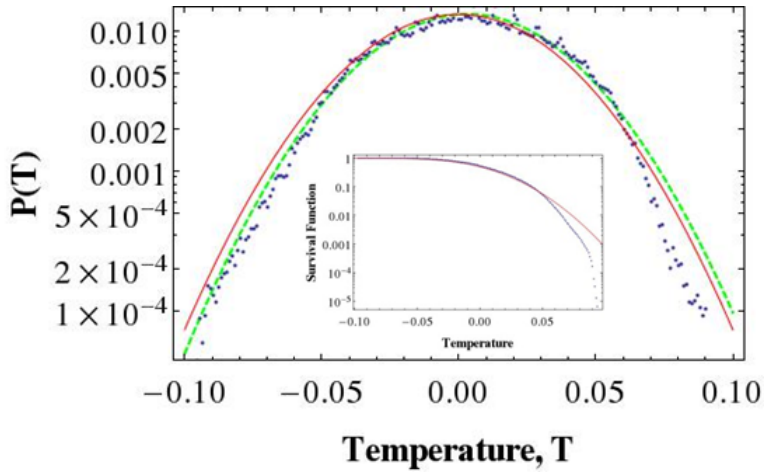

Figure 5.9. Histogram of fluctuations in temperature due to inhomogeneous microstructure compared to Gaussian (red and green-dashed lines). Inset: Survival function (complementary cumulative distribution) of fluctuation compared to Gaussian.

in correlated systems [116], but must remain a subject for future work.

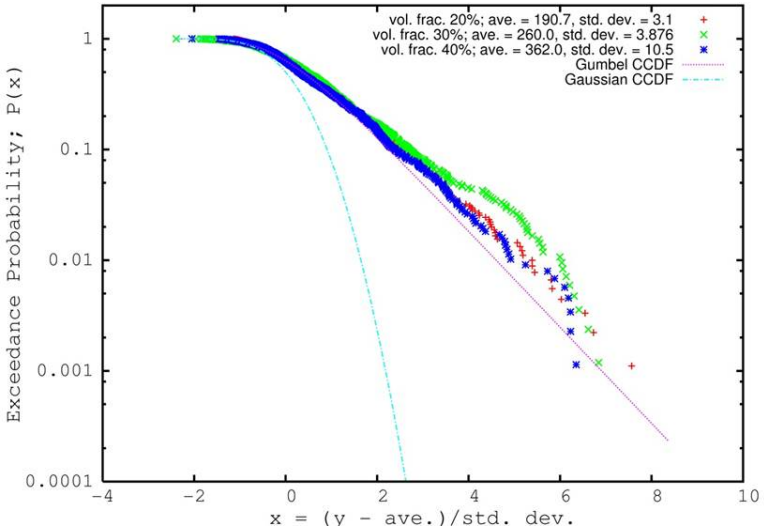

Figure 5.10. thermal UQ

Chapter 6

Conclusions and Outlook

In this work we have explored a number of issues related to transport in heterogeneous systems. In Chapter 2 we considered models based on contraction of the underlying stochastic processes that suggested models capable of bridging multiple scales in complex, disordered materials. We found the non-Fickian behavior was related to non-stationarity of the processes. In addition, for systems with correlations due to transient inhomogeneities, it was shown that the non-stationary processes were also non-Gaussian. Continuing work along these lines is investigating continuous-time random walk models for conduction in particulate systems in connection with the results of work described in Chapter 5.

The effect of inhomogeneities on diffusive processes was explored in Chapter 3. We found that an external field could be added to the diffusion equation to account for deviation from the homogeneous case. This external field was shown to be the equilibrium solvation force related to the excess chemical potential. Given this thermodynamic basis, the relevance to multispecies diffusion systems in dense simple fluids (i.e., metals) was discussed. This is a potentially fruitful direction for future work.

Chapter 4 reported on efforts to build and test an experimental apparatus to measure the constitutive relation associated with non-Fickian discussed in Chapter 2. Future efforts to deploy this technique in a number of complex, soft matter systems are also underway.

In Chapter 5 a numerical simulation technique for the calculation of effective conductivities in particulate heterogeneous media was briefly discussed. Simulation results compared well with theoretical results for mono-sized dispersions. Additionally, the statistical information obtained from the multiple particle configurations suggested a stochastic approach to model the variation of properties due to the dynamical processes used to create the configurations. With this information in hand uncertainty quantification of component performance based on effective material properties may be given a firm basis in terms of the physical processes involved in manufacturing.

In summary, we've only scratched the surface of a broad area of research. However, we believe we have developed and deployed capabilities that have highlighted some fundamental issues related to transport in complex, disordered materials. We believe these tools and techniques will continue to add value to discovery research efforts in this field.

References

[1] A. Einstein, The theory of the Opsalescence of homogeneous fluids and liquid mixtures near the critical state, *Annalen der Physik*, Vol. 33, p. 1275, 1910.

[2] G. Ruppeiner, Riemannian geometry in thermodynamic fluctuation theory, *Reivew of Modern Physics*, Vol. 67, pp. 605–659, 1995.

[3] A. Einstein, On the movement of small particles suspended in stationary liquids required by the molecular-kinetic theory of heat, *Annalen der Physik*, Vol. 17, p. 549, 1905. bibitemlangevin P. Langevin, On the theory of brownian motion, *C.R. Acad. Sci. (Paris)*, Vol 146, pp. 530–533, 1908.

[4] P. Glansdorff and I. Prigogine, *Thermodynamic Theory of Structure, Stability, and Fluctuations*, Wiley Interscience, London, UK, 1971.

[5] C. Gardiner, *Stochastic Methods: A Handbook for the Natural and Social Sciences*, Springer, Germany, 2009.

[6] J. Klafter and I.M. Sokolov, *First Steps in Random Walks: From Tools to Applications*, Oxford University Press, Oxford, UK, 2011.

[7] G.F. Lawler, *Random Walk and the Heat Equation*, Vol. 55, Sudent Mathematical Library, American Mathematical Society, 2010.

[8] Mark M. Meerschaert and Alla Sikorskii, *Stochastic Models for Fractional Calculus*, Vol. 43, De Gruyter Studies in Mathematics, Walter de Gruyter, Berlin/Boston, 2012.

[9] D. Applebaum, *Lévy Processes and Stochastic Calculus*, Vol. 116, Cambridge Studies in Advanced Mathematics, Cambridge, UK2009.

[10] J.R. Norris, *Markov Chains*, Cambridge University Press, Cambridge, UK, 1997.

[11] E.W. Montroll and G.H. Weiss, Random walks on lattices. II, *Journal of Mathematical Physics*, Vol. 6, pp. 167–181, 1965.

[12] Jean-Philippe Bouchaud and Antoine Georges, Anomalous diffusion in disordered media: Statistical mechanisms, models and physical applications, in *Physics Reports* Vol. 195, No. 4-5, pp. 127–293, 1990.

[13] V.M. Kenkre, E.W. Montroll and M.F. Shlesinger, Generalized master equations for continuous-time random walks, *Journal of Statistical Physics*, Vol. 9, pp, 45–50, 1973.

[14] M. Sahimi, B.D. Hughes, L.E. Scriven and T.H. Davis, Stochastic transport in disordered systems, *Journal of Chemical Physics*, Vol. 78, pp. 6849–6864.

[15] S. Kirkpatrick, Percolation and Conduction, *Reviews of Modern Physics*, Vol. 45, pp. 574–588.

[16] G. Didier, S.A. McKinley, D.B. Hill, J. Fricks, Statistical challenges in microrheology, in *Journal of Time Series Analysis* Vol. 33, No. 5, pp. 724–743, 2012.

[17] I.M. Sokolov, Models of anomalous diffusion in crowded environments, in *Soft Matter*, Vol. 8, No. 35, pp. 9043–9052, 2012.

[18] R. Klages and G. Radons and I.M. Sokolov eds., *Anomalous Transport: Foundations and Applications*, Wiley-Vch Verlag GmbH, Germany, 2008.

[19] Felix Höfling and Thomas Franosch, Anomalous transport in the crowded world of biological cells, in in *Reports on Progress in Physics*, Vol. 76, No. 4, p. 046602, 2013.

[20] H. Risken, *The Fokker-Planck Equation: Methods of Solution and Applications*, Springer-Verlag, Berlin, Germany, 1984.

[21] R. Zwangzig, *Nonequilibrium Statistical Mechanics*, Oxford University Press, Oxford, UK, 2001.

[22] B.B. Mandelbrot and J.W. van Ness, Fractional brownian motion, fractional noise applications, in *SIAM Review*, Vol. 10, pp. 422–437, 1968.

[23] Y. Gefen, A. Aharony and S. Alexander, Anomalous diffusion on percolating clusters, in *Physical Review Letters*, Vol. 50, pp. 77–80, 1983.

[24] M. San Miguel and J.M. Sancho, A colored-noise approach to brownian motion in position space. Corrections to the smoluchowski equation, in *Journal of Statistical Physics*, Vol. 22, pp. 605–624, 1980.

[25] K. Razi Navqi and S. Waldenstrom, Brownian motion description of heat conduction by phonons, in *Physical Review Letters*, Vol. 95, p. 065901, 2005.

[26] K.E. Bassler, G.H. Gunaratne and J.L. McCauley, Markov processes, Hurst exponents, and nonlinear diffusion equations: with applications to finance, in *Physica A*, Vol. 369, pp. 343–353, 2006.

[27] L. Nottale, Scale-relativity and quantization of the universe I. Theoretical framework, in *Astronomy and Astrophysics*, Vol. 327, pp. 867–889, 1997.

[28] G.H. Vineyard, Scattering of slow neutrons by a liquid, in *Physical Review*, Vol. 110, pp. 999–1010, 1958.

[29] V.V. Novikov, Physical properties of fractal structures, in *Advances in Chemical Physics*, Vol. 133, pp. 93-284, 2006.

[30] G. Chen, Ballistic-diffusive heat-conduction equations, in *Physical Review Letters*, Vol. 86, pp. 2297–2300, 2001.

[31] P.C. Hemmer, On a generalization of smoluchowski's diffusion equation, in *Physica A*, Vol. 27, pp. 79, 1961.

[32] Y.M. Ali and L.C. Zhang, Relativistic heat conduction, in *International Journal of Heat and Mass Transfer*, Vol. 48, pp. 2397–2406.

[33] R. Metzler and J. Klafter, The random walker's guide to anomalous diffusion: a fractional dynamics approach, in *Physics Reports*, Vol. 339, pp. 1–77, 2000.

[34] C. Tsallis and D.J. Bukman, Anomalous diffusion in the presence of external fources: exact time-dependent solutions and their thermostatistical basis, in *Physical Review E*, Vol. 54, pp. R2197–R2200, 1996.

[35] C. Tsallis et al., Statistical-Mechanical Foundation of the ubiquity of Levy distributions in nature, in *Physical Review Letters*, Vol. 75, pp. 3589–3591, 1995.

[36] F. Baudoin and L. Coutin, Operators associated with a stochastic differential equation driven by fractional Brownian motions, in *Stochastic Processes and their Applications*, Vol. 117, pp. 550-574, 2007.

[37] A.J. Archer and R. Evans, Dynamical density functional theory and its application to spinodal decomposition, in *Journal of Chemical Physics*, Vol. 121, pp. 4246–4254, 2004. bibitemarcher A.J. Archer, Dynamical density functional theory for molecular and colloidal fluids: a microscopic approach to fluid mechanics, in *Journal of Chemical Physics*, Vol. 130, p. 014509, 2009.

[38] A.D. Baczewski and S.D. Bond, Numerical integration of the extended variable generalized Langevin equation with a positive Prony representable memory kernel, in *Journal of Chemical Physics*, Vol. 139, p. 044107, 2013.

[39] B.U. Felderhof, Transient flow caused by a sudden impulse or twist applied to a sphere immersed in a viscous incompressible fluid, in *Physics of Fluids*, Vol. 19, p. 073102, 2007.

[40] R. Kupferman, Fractional kinetics in Kac-Zwanzig heat bath models, in *Journal of Statistical Physics*, Vol. 114, pp. 291–325.

[41] R. Gorenflo and F. Mainardi, Fractional Calculus: Integral and differential equations of fractional order, in *CISM Courses and Lectures*, Vol. 378, pp. 223-276, Springer-Verlag, Berlin, 1997

[42] F. Mainardi, Fractional Calculus: Some basic problems in continuum and statistical mechanics, in *CISM Courses and Lectures*, Vol. 378, pp. 291-348, Springer-Verlag, Berlin, 1997

[43] S.C. Kou, Stochastic modeling in nanoscale biophysics: subdiffusion within proteins, in *The Annals of Applied Statistics*, Vol. 2, pp. 501-535, 2008.

[44] B.U. Felderhof, Backtracking of a sphere slowing down in a viscous compressible fluid, in *Journal of Chemical Physics*, Vol. 123, p. 044902, 2005.

[45] M. Parmar, A. Haselbacher and S. Balachandar, Generalized Basset-Boussinesq-Oseen equation for unsteady forces on a sphere in a compressible flow, in *Physical Review Letters*, Vol. 106, p. 084501, 2011.

[46] P. R. Schunk et al., Performance of mesoscale modeling methods for predicting rheological properties of charged polystyrene/water suspensions, in *Journal of Rheology*, Vol. 56, pp. 353–384, 2012.

[47] R. Everaers and M. R. Ejtehadi, Interaction potentials for soft and hard ellipsoids, in *Physical Review E*, Vol. 67, pp. 041710-1–8, 2003.

[48] A. Kumar and J.J.L. Higdon, Origins of the anomalous stress behavior in charged colloidal suspensions under shear, in *Physical Reiview E*, Vol. 82, p. 051401, 2010.

[49] P. Chaudhuri, L. Berthier, and W. Kob, Universal nature of particle displacements close to glass and jamming transitions, in *Physical Review Letters*, Vol. 99, p. 060604, 2007.

[50] C. Beck, Generalized statistical mechanics for superstatistical systems, in *Philosophical Transactions of the Royal Society A*, Vol. 369, pp. 453–465, 2011. S.R. Challa and F. van Swol, Molecular simulations of lubrication and solvation forces, in *Physical Review E*, Vol. 73, p. 016306, 2006.

[51] R. M. Mazo, *Brownian Motion : Fluctuations, Dynamics, and Applications*, Oxford University Press, Oxford, UK, 2002.

[52] J.R. Henderson and F. van Swol, in *Molecular Physics*, Vol. 51, pp. 991–1010, 1984.

[53] D.M. Heyes, M.J. Cass, J.G. Powles and W.A.B. Evans, in *Journal of Physical Chemistry B*, Vol. 111, pp. 1455–1464, 2007.

[54] P. Protopapas, H.C. Andersen, and N.A.D. Parlee, Theory of transport in liquid metals. I. Calculation of self-diffusion coefficients, in *Journal Chemical Physics*, Vol. 59, pp. 15–25, 1973.

[55] D. Ben-Amotz and D.R. Herschbach, Estimation of Effective Diameters for Molecular Fluids, in *Journal of Physical Chemistry*, Vol. 94, pp. 1038–1047, 1973.

[56] P. Protopapas, H.C. Andersen, and N.A.D. Parlee, Theory of transport in liquid metals. II. Calculation of shear viscosity coefficients, in *Chemical Physics*, Vol. 8, pp. 17–26, 1975.

[57] B.J. Alder, D.M. Gass, and T.E. Wainwright, Studies in Molecular Dynamics. VIII. The Transport Coefficients for a Hard-Sphere Fluid, in *Journal Chemical Physics*, Vol. 59, pp. 15–25, 1973.

[58] Y. Rosenfeld, in *Physical Review Letters*, Vol. 63, p. 980, 1989.

[59] D.J. Evans and G.P. Morriss, *Statistical Mechanics of Nonequilibrium Liquids*, Academic Press, London, UK, 1990.

[60] D.K. Enskog, *Svenska Vetenskapsaded. Handl*, Vol. 63, No. 4 1922.

[61] S. Chapman and T.G. Cowling, *The Mathematical Theory of Nonuniform Gases*, 2nd ed., Cambridge University Press, Cambridge, UK, 1922.

[62] M.K. Tham and K.E. Gubbins, Kinetic Theory of Multicomponent Dense Fluid Mixtures of Rigid Spheres, in *Journal of Chemical Physics*, Vol. 55, pp. 268–279, 1971.

[63] Lopez de Haro, E.G.D. Cohen and J.M. Kincaid, Kinetic Theory of Multicomponent Dense Fluid Mixtures of Rigid Spheres, in *Journal of Chemical Physics*, Vol. 78, p. 2746, 1983.

[64] J.J. Erpenbeck, Transport coefficients of hard-sphere mixtures: Theory and Monte Carlo molecular dynamics calculations for an isotopic mixture, in *Physical Review A*, Vol. 39, pp. 4718–4731, 1989.

[65] X. Liu, T.J.H. Vlugt and A. Bardow, in *Ind. Eng. Chem. Res.*, Vol. 50, pp. 10350–10358, 2011.

[66] Arrhenius, in Z. Physik. Chem., Vol. 1, p. 285, 1887.

[67] L. Grunberg and A.H. Nissan, Mixture Law for Viscosity, in *Nature*, Vol. 164, pp. 799–800, 1949.

[68] S. Fraden and G. Maret, Multiple light scattering from concentrated, interacting suspensions, in *Physical Review Letters*, Vol. 65, p. 512, 1990.

[69] S.J. Nilsen and A.P. Gast, The influence of structure on diffusion in screened Coulombic suspensions, in *Journal Chemical Physics*, Vol. 101, pp. 4975-4985, 1994.

[70] S. Romer, C. Urban, H. Bissig, A. Stradner, F. Scheffold and P. Schurtenberger, Dynamics of concentrated colloidal suspensions: diffusion, aggregation and gelation, in *Philos. Trans. R. Soc. Lond. Ser. Math. and Phys. Eng. Sci.*, Vol. 359, pp. 977-984, 2001.

[71] D.A. Weitz, X.J. Zhu, D.J. Durian, H. Gang and D.J. Pine, Diffusing-wave spectroscopy: The technique and some applications, in *Physica Scripta*, Vol. T49B, pp. 610-621, 1993.

[72] D.J. Durian, D.A. Weitz and D.J. Pine, Scaling behavior in shaving cream, in *Physical Review E*, Vol. 44, pp. R7902-R7905, 1991a.

[73] D.J. Durian, D.A. Weitz and D.J. Pine, Multiple Light-Scattering Probes of Foam Structure and Dynamics, in *Science*, Vol. 252, pp. 686-688, 1991b.

[74] J. Galvan-Miyoshi, J. Delgado and R. Castillo, Diffusing wave spectroscopy in Maxwellian fluids, in *European Physical Journal E*, Vol. 26, pp. 369-377, 2008.

[75] E. Sarmiento-Gomez, D. Lopez-Diaz, and R. Castillo, Microrheology and characteristic lengths in wormlike micelles made of a zwitterionic surfactant and SDS in brine, in *Journal of Physical Chemistry B*, Vol. 114, pp. 12193-12202, 2010.

[76] Z. Gaygadzhiev, M. Corredig and M. Alexander, Diffusing Wave Spectroscopy Study of the Colloidal Interactions Occurring between Casein Micelles and Emulsion Droplets: Comparison to Hard-Sphere Behavior, in *Langmuir*, Vol. 24, pp. 3794-3800, 2008.

[77] A.J. Liu, S. Ramaswamy, T.G. Mason, H. Gang and D.A. Weitz, Anomalous Viscous Loss in Emulsions, *Physical Review Letters*, Vol. 76, pp. 3017-3020, 1996.

[78] S. Marze, M. Choimet and L. Foucat, In vitro digestion of emulsions: diffusion and particle size distribution using diffusing wave spectroscopy and diffusion using nuclear magnetic resonance, in *Soft Matter*, Vol. 8, pp. 10994-11004, 2012.

[79] F. Scheffold and P. Schurtenberger, Light Scattering Probes of Viscoelastic Fluids and Solids, in *Soft Materials*, Vol. 1, p. 139, 2003.

[80] D.A. Weitz, D.J. Pine, P.N. Pusey and R.J.A. Tough, Nondiffusive Brownian motion studied by diffusing-wave spectroscopy, in *Physical Review Letters*, Vol. 63, pp. 1747-1750, 1989.

[81] D.A. Weitz and D.J. Pine, Diffusing-wave spectroscopy, in *Dynamic Light Scattering*, W. Brown, ed., pp. 652720, Clarendon Press, Oxford, UK, 1993.

[82] J.B. Segur and H.E. Oberstar, Viscosity of Glycerol and Its Aqueous Solutions, in *Ind. Eng. Chem.*, Vol. 43, pp. 2117-2120, 1951.

[83] N.-S. Cheng, Formula for the Viscosity of a Glycerol-Water Mixture. in *Ind. Eng. Chem. Res.*, Vol. 47, pp. 3285-3288, 2008.

[84] Bogush, G.H., Tracy, M.A., Zukoski IV, C.F., 1988. Preparation of monodisperse silica particles: Control of size and mass fraction. J. Non-Cryst. Solids 104, 95106.

[85] J.C. Crocker and D.G. Grier, Methods of Digital Video Microscopy for Colloidal Studies, in *Journal Colloid Interface Science*, Vol. 179, pp. 298-310, 1996.

[86] D. Blair and E. Dufresne, *MATLAB Particle Tracking Routine*, 2008.

[87] D.J. Durian, Bubble-scale model of foam mechanics: Melting, nonlinear behavior, and avalanches. in *Physical Review E*, Vol. 55, pp. 1739-1751, 1997.

[88] D.J. Durian, Foam Mechanics at the Bubble Scale, in *Physical Review Letters*, Vol. 75, pp. 4780-4783, 1995.

[89] A.D. Gopal and D.J. Durian, Fast thermal dynamics in aqueous foams, in *Journal of the Optical Society America*, Vol. 14, pp. 150-155, 1997.

[90] V. Viasnoff, F. Lequeux, and D.J. Pine, Multispeckle diffusing-wave spectroscopy: a tool to study slow relaxation and time-dependent dynamics, arXiv:cond-mat/0203396, 2002.

[91] D. R. Noble, E. P. Newren, and J. B. Lechman, A conformal decomposition finite element method for modeling stationary fluid interface problems, in *International Journal for Numerical Methods in Fluids* Vol. 63, pp. 725–742, 2009.

[92] R. Glowinski et al., A fictitious domain approach to the direct numerical simulation of incompressible fluid flow past moving rigid bodies: Application to particulate flow, in *Journal of Computational Physics*, Vol. 162, pp. 363–426, 2001.

[93] C. S. Peskin, The Immersed Boundary Method, in *Acta Numerica*, pp. 1–39, 2002.

[94] E. A. Fadlun, R. Verzicco, and J. Mohd-Yusof, Combined immersed-boundary finite-difference methods for three-dimensional complex flow simulations, in *Journal Computational Physics* Vol. 161, 35–60, 2000.

[95] P. Singh, T.I. Hesla and D.D. Joseph, Distributed Lagrange multiplier method for particulate flows with collisions, in *International Journal of Multiphase Flow*, Vol. 29, pp. 495–509, 2003.

[96] T. Belytschko and T. Black, Elastic crack growth in finite elements with minimal remeshing, in *International Journal for Numerical Methods in Engineering*, Vol. 45, 601–620, 1999.

[97] T. Belytschko, N. Moes, S. Usui, and C. Parimi, Arbitrary discontinuities in finite elements, in *International Journal of Numerical Methods in Engineering*, Vol. 50, pp. 993–1013, 2001.

[98] M. Beran, Statistical continuum theories, in *Journal of Rheology*, Vol. 9, pp. 339–355, 1965.

[99] M. Hori, Statistical theory of effective electrical, thermal, and magnetic properties of random heterogeneous materials. I. Perturbation expansions for the effective permittivity of cell materials, in *Journal of Mathematical Physics*, Vol. 14, pp. 514–523, 1973.

[100] C. A. Miller and S. Torquato, Effective conductivity of hard-sphere dispersions, in *Journal of Applied Physics*, Vol. 68, pp. 5486–5493, 1990.

[101] C. Kim and S. Torquato, Effective conductivity of suspensions of spheres by Brownian motions simulation, in *Journal of Applied Physics*, Vol. 69, pp. 2280–2289, 1991.

[102] Z. T. Lin and X. Wu, New cartesian grid methods for interface problems using the finite element formulation, in *Numer. Math.*, Vol. 96, pp. 61–98, 2003.

[103] R. C. McPhedran and D. R. McKenzie, The conductivity of lattices of spheres. I. The simple cubic lattice, in *Proceedings of the Royal Society A*, Vol. 359, pp. 45–63, 1978.

[104] D. R. McKenzie, R.C. McPhedran and G.H. Derrick, The conductivity of lattice sphere. II. The body centered and face centered cubic lattices, in *Proceedings of the Royal Society A*, Vol. 362, pp. 211–232, 1978.

[105] G. W. Milton, Bounds on the complex permittivity of a two-component composite material,in *Journal of Applied Physics*, Vol. 52, pp. 5826-5293, 1981.

[106] P. K. Notz et al., *Aria 1.5: User Manual, SAND2007-2734*, Sandia National Laboratories, Albuquerque, 2007.

[107] T. P. Fries and A. Zilian, On the time integration in the XFEM, in *International Journal of Numerical Methods in Engineering*, Vol. 79, pp. 69–93, 2009.

[108] F. Ilinca and J. F. Hetu, A finite element immersed boundary method for fluid flow around moving objects, in *Comp. & Fluids*, Vol. 39, pp. 1656–1671, 2010.

[109] F. Illinca and J. F. Hetu, A finite element immersed boundary method for fluid flow around rigid objects, in *International Journal for Numerical Methods in Fluids* Vol. 65, 856–875, 2011.

[110] G. J. Wagner, The extended finite element method for rigid particles in Stokes flow,in *International Journal for Numerical Methods in Engineering*, Vol. 51, pp. 293–313, 2001.

[111] N. Zamel et al., Extimating effective thermal conductivity in carbon paper diffusion media, in *Chemical Engineering Science*, Vol. 65, pp. 3994–4006, 2010.

[112] M. Ostoja-Starzewski and X. Wang, Stochastic finite elements as a bridge between random material microstructure and global response, in *Computer Methods in Applied Mechanics and Engineering*, Vol. 168, pp. 35–49, 1999.

[113] M. Ostoja-Starzewski, Microstructural disorder, mesoscale finite elements and macroscopic response, in *Proceedings of the Royal Society of London A*, Vol. 455, pp. 3189–3199, 1999.

[114] M. Ostoja-Starzewski, Material spatial randomness: From statistical to representative volume element, in *Probabilistic Engineering Mechanics*, Vol. 21, pp. 112–132, 2006.

[115] G. Ruppeiner, Riemannian geometry in thermodynamic fluctuation theory, in *Reviews of Modern Physics*, Vol. 67, pp. 605–659, 1995.

[116] S.T. Bramwell, et al., Universal fluctuations in correlated systems, *Physical Reveiw Letters*, Vol. 84, pp. 3744–3747, 2000.

Appendix A

Numerical Integration of the Extended Variable Generalized Langevin Equation with a Positive Prony Representable Memory Kernel

Andrew D. Baczewski[1, a)] and Stephen D. Bond[1]

Multiphysics Simulation Technologies Department, Sandia National Laboratories, Albuquerque, NM 87185, USA

Generalized Langevin dynamics (GLD) arise in the modeling of a number of systems, ranging from structured fluids that exhibit a viscoelastic mechanical response, to biological systems, and other media that exhibit anomalous diffusive phenomena. Molecular dynamics (MD) simulations that include GLD in conjunction with external and/or pairwise forces require the development of numerical integrators that are efficient, stable, and have known convergence properties. In this article, we derive a family of extended variable integrators for the Generalized Langevin equation (GLE) with a positive Prony series memory kernel. Using stability and error analysis, we identify a superlative choice of parameters and implement the corresponding numerical algorithm in the LAMMPS MD software package. Salient features of the algorithm include exact conservation of the first and second moments of the equilibrium velocity distribution in some important cases, stable behavior in the limit of conventional Langevin dynamics, and the use of a convolution-free formalism that obviates the need for explicit storage of the time history of particle velocities. Capability is demonstrated with respect to accuracy in numerous canonical examples, stability in certain limits, and an exemplary application in which the effect of a harmonic confining potential is mapped onto a memory kernel.

The following article appeared in J. Chem. Phys. 139, 044107 (2013) and may be be found at http://jcp.aip.org/resource/1/jcpsa6/v139/i4/p044107_s1

[a)]Electronic mail: adbacze@sandia.gov; During the preparation of this manuscript, author was also a graduate student in the Department of Electrical and Computer Engineering and the Department of Physics and Astronomy at Michigan State University, East Lansing, MI 48824.

I. INTRODUCTION

Langevin dynamics[1] is a modeling technique, in which the motion of a set of massive bodies in the presence of a bath of smaller solvent particles is directly integrated, while the dynamics of the solvent are "averaged out". This approximation may lead to a dramatic reduction in computational cost compared to "explicit solvent" methods, since dynamics of the solvent particles no longer need to be fully resolved. With Langevin dynamics, the effect of the solvent is reduced to an instantaneous drag force and a random delta-correlated force felt by the massive bodies. This framework has been applied in a variety of scenarios, including implicit solvents,[2,3] Brownian dynamics,[4] dynamic thermostats,[5] and the stabilization of time integrators.[6]

In spite of the numerous successes of conventional Langevin dynamics it has long been recognized that there are physically compelling scenarios in which the underlying assumptions break down, necessitating a more general treatment.[3,7] To this end, generalized Langevin dynamics (GLD) permits the modeling of systems in which the inertial gap separating the massive bodies from the smaller solvent particles is reduced. Here the assumptions of an instantaneous drag force and a delta-correlated random force become insufficient, leading to the introduction of a temporally non-local drag and a random force with non-trivial correlations. GLD has historically been applied to numerous problems over the years,[8–11] with a number of new applications inspiring a resurgence of interest, including microrheology,[12–15] biological systems,[16–18] nuclear quantum effects,[19–21] and other situations in which anomalous diffusion arises.[22]

To facilitate computational exploration of some of these applications, a number of authors have developed numerical integration schemes for the generalized Langevin equation (GLE), either in isolation or in conjunction with extra terms accounting for external or pairwise forces as would be required in a molecular dynamics (MD) simulation. These schemes must deal with a number of complications if they are to remain computationally efficient and accurate.

- The retarded drag force takes the form of a convolution of the velocity with a memory kernel. This requires the storage of the velocity history, and the numerical evaluation of a convolution at each time step, which can become computationally expensive.

- The generation of a random force with non-trivial correlations may also require the storage of a sequence of random numbers, and some additional computational expense incurred at each time step.

Numerous methods exist that circumvent either one or both of these difficulties.[8,23–30] Each has a

different computational cost, implementation complexity, order of convergence, and specific features, e.g., some are restricted to single exponential memory kernels, require linear algebra, etc. To this end, it is difficult to distinguish any individual method as being optimal, especially given the broad range of applications to which GLD may be applied.

Motivated by the aforementioned applications and previous work in numerical integrators, we have developed a new family of time integration schemes for the GLE in the presence of conservative forces, and implemented it in a public domain MD code, LAMMPS.[31] Our primary impetus was to enable the development of reduced order models for nanocolloidal suspensions, among a variety of other applications outlined above. Previous computational studies of these systems using explicit solvents have demonstrated and resolved a number of associated computational challenges.[32] Our method enables a complementary framework for the modeling of these types of systems using implicit solvents that can include memory effects. Otherwise, to date the GLE has only been solved in the presence of a number of canonically tractable external potentials and memory kernels.[16,33,34] Integration into the LAMMPS framework, provides a number of capabilities. LAMMPS includes a broad array of external, bonded, and non-bonded potentials, yielding the possibility for the numerical exploration of more complex systems than have been previously studied. Finally, LAMMPS provides a highly scalable parallel platform for studying N-body dynamics. Consequently, extremely large sample statistics are readily accessible even in the case of interacting particles, for which parallelism is an otherwise non-trivial problem.

In this paper, details germane to both the development of our time integration scheme, as well as specifics of its implementation are presented. The time integration scheme to be discussed is based upon a two-parameter family of methods specialized to an extended variable formulation of the GLE. Some of the salient advantages of our formulation and the final time integration scheme are:

- Generalizability to a wide array of memory kernels representable by a positive Prony series, such as power laws.
- Efficiency afforded by an extended variable formulation that obviates the explicit evaluation of time convolutions.
- Inexpensive treatment of correlated random forces, free of linear algebra, requiring only one random force evaluation per extended variable per timestep.
- Exact conservation of the first and second moments of either the integrated velocity distribu-

tion or position distribution, for harmonically confined and free particles.

- Numerically stable approach to the Langevin limit of the GLE.
- Simplicity of implementation into an existing Verlet MD framework.

The specialization to Prony-representable memory kernels is worth noting, as there is a growing body of literature concerning this form of the GLE.[14,35,36] A number of results have been presented that establish the mathematical well-posedness of this extended variable GLE including a term accounting for smooth conservative forces, as may arise in MD.[36] These results include proofs of ergodicity and exponential convergence to a measure, as well as a discussion of the Langevin limit of the GLE in which the parameters of the extended system generate conventional Langevin dynamics.

One somewhat unique feature of our framework is that we are analyzing the GLE using methods from stochastic calculus. In particular, we focus on weak convergence in the construction our method, i.e., error in representing the moments of the stationary distribution or the distribution itself. The optimal parametrization of our two-parameter family of methods will be defined in terms of achieving accuracy with respect to this type of convergence. In particular, the optimal method that has been implemented achieves exactness in the first and second moments of the integrated velocity distribution for harmonically confined and free particles. Few authors have considered this type of analysis for even conventional Langevin integrators, with a notable exception being Wang and Skeel,[37] who have carried out weak error analysis for a number of integrators used in conventional Langevin dynamics. To the best of our knowledge, this is the first time that such a weak analysis has been carried out for a GLE integrator. We hope that these considerations will contribute to a better understanding of existing and future methods.

The remainder of this paper is structured as follows:

- **Section II A** introduces the mathematical details of the GLE.
- **Section II B** presents the extended variable formulation and its benefits.
- **Section II C** develops the theory associated with integrating the extended variable GLE in terms of a two-parameter family of methods.
- **Section II D** provides details of the error analysis that establishes the 'optimal' method among this family.
- **Section II E** discusses the extension of our method to a multi-stage splitting framework.

- **Section III** summarizes details of the implementation in LAMMPS.
- **Section IV** presents a number of results that establish accuracy in numerous limits/scenarios, including demonstration of utility in constructing reduced order models.

II. MATHEMATICAL DETAILS

A. Statement of the Problem

The GLE for N_p particles moving in d-dimensions can be written as

$$M dV(t) = F^c\left(X(t)\right) dt - \int_0^t \Gamma(t-s) V(s) ds dt + F^r(t) dt, \tag{1a}$$

$$dX(t) = V(t) dt, \tag{1b}$$

with initial conditions $X(0) = X_0$ and $V(0) = V_0$. Here, $F^c : \mathbb{R}^{dN_p} \to \mathbb{R}^{dN_p}$ is a conservative force, F^r is a random force, M is a diagonal mass matrix, and Γ is a memory kernel. The solution to this stochastic integro-differential equation is a trajectory, which describes the positions $X : \mathbb{R}^+ \to \mathbb{R}^{dN_p}$ and velocities $V : \mathbb{R}^+ \to \mathbb{R}^{dN_p}$ of the particles as a function of time, $t \geq 0$. The second term on the right-hand side of Equation 1a accounts for the temporally non-local drag force, and the third term accounts for the correlated random force. The nature of both forces are characterized by the memory kernel, $\Gamma : \mathbb{R}^+ \to \mathbb{R}$, consistent with the Fluctuation-Dissipation theorem (FDT).[3,38] The FDT states that equilibration to a temperature, T, requires that the two-time correlation of $F^r(t)$ and $\Gamma(t)$ be related as follows:

$$\langle F_i^r(t+s) F_j^r(t) \rangle = \mathrm{k}_B \mathrm{T}\, \Gamma(s) \delta_{ij}, \quad s \geq 0. \tag{2}$$

Here, δ_{ij} is the Kronecker delta, and k_B is Boltzmann's constant.

In the context of an MD simulation, we are interested in solving Equation 1 for both $X(t)$ and $V(t)$ at a set of N_t uniformly spaced discrete points in time. To this end, we seek to construct a solution scheme that is mindful of the following complications:

- Calculation of the temporally non-local drag force requires a convolution with $\Gamma(t)$, and thusly the storage of some subset of the time history of $V(t)$.
- Numerical evaluation of $F^r(t)$ requires the generation of a sequence of correlated random numbers, as specified in Equation 2.

- As Equation 1 is a stochastic differential equation (SDE), we are not concerned with issues of local or global error, but rather that the integrated solution converges in distribution.

To circumvent the first two complications, we work with an extended variable formalism[14,20,39,40] in which we assume that $\Gamma(t)$ is representable as a Prony series:

$$\Gamma(t) = \sum_{k=1}^{N_k} \frac{c_k}{\tau_k} \exp\left[-\frac{t}{\tau_k}\right], \quad t \geq 0. \tag{3}$$

As will be demonstrated in Section II B, this form of the memory kernel will allow us to map the non-Markovian form of the GLE in Equation 1 onto a higher-dimensional Markovian problem with dN_k extended variables per particle. The third complication is resolved in Sections II C and II D, in which a family of integrators is derived, and then 'optimal' parameters are selected based upon an error analysis of the moments of the integrated velocity.

B. Extended Variable Formalism

We introduce the extended variable formalism in two stages. First, we define a set of extended variables that allow for an effectively convolution-free reformulation of Equation 1. Then, we demonstrate that the non-trivial temporal correlations required of $F^r(t)$ can be effected through coupling to an auxiliary set of Ornstein-Uhlenbeck (OU) processes.

We begin by defining the extended variable, $Z_{i,k}(t)$, associated with the kth Prony mode's action on the ith component of $X(t)$ and $V(t)$:

$$Z_{i,k}(t) = -\int_0^t \frac{c_k}{\tau_k} \exp\left[-\frac{(t-s)}{\tau_k}\right] V_i(s) ds \tag{4}$$

Component-wise, Equation 1 can now be rewritten as:

$$m_i dV_i(t) = F_i^c\left(X(t)\right) dt + \sum_{k=1}^{N_k} Z_{i,k}(t) dt + F_i^r(t) dt, \tag{5a}$$

$$dX_i(t) = V_i(t) dt. \tag{5b}$$

Rather than relying upon the integral form of Equation 4 to update the value of $Z_{i,k}(t)$, we consider the total differential of $Z_{i,k}(t)$ to generate an equation of motion that takes the form of a simple SDE:

$$dZ_{i,k}(t) = -\frac{1}{\tau_k} Z_{i,k}(t) dt - \frac{c_k}{\tau_k} V_i(t) dt \tag{6}$$

Now, the system of Equations 5 and 6 can be resolved for $X_i(t)$, $V_i(t)$, and $Z_{i,k}(t)$ without requiring the explicit evaluation of a convolution integral.

Next, we seek a means of constructing random forces that obey the FDT, as in Equation 2. To this end, we consider the following SDE:

$$dF_{i,k}(t) = -\frac{1}{\tau_k}F_{i,k}(t)dt + \frac{1}{\tau_k}\sqrt{2\mathrm{k}_B\mathrm{T}c_k}dW_{i,k}(t) \tag{7}$$

If $W_{i,k}$ is a standard Wiener process, this SDE defines an Ornstein-Uhlenbeck (OU) process, $F_{i,k}(t)$. Using established properties of the OU process,[41] we can see that $F_{i,k}(t)$ has mean zero and two-time correlation:

$$\langle F_{i,k}(t+s)F_{i,k}(t)\rangle = \mathrm{k}_B\mathrm{T}\frac{c_k}{\tau_k}\exp\left[-\frac{1}{\tau_k}s\right], \quad s \geq 0 \tag{8}$$

It is then clear, that the random force in Equation 1 can be rewritten as:

$$F_i^r(t) = \sum_{k=1}^{N_k} F_{i,k}(t) \tag{9}$$

Here each individual contribution is generated by a standard OU process, the discrete-time version of which is the AR(1) process. While we are still essentially forced to generate a sequence of correlated random numbers, mapping onto a set of AR(1) processes has the advantage of requiring the retention of but a single prior value in generating each subsequent value. Further, standard Gaussian random number generators can be employed.

Combining both results, the final extended variable GLE can be expressed in terms of the composite variable, $S_{i,k}(t) = Z_{i,k}(t) + F_{i,k}(t)$:

$$m_i dV_i(t) = F_i^c\left(X(t)\right)dt + \sum_{k=1}^{N_k} S_{i,k}dt \tag{10a}$$

$$dX_i(t) = V_i(t)dt \tag{10b}$$

$$dS_{i,k}(t) = -\frac{1}{\tau_k}S_{i,k}(t)dt - \frac{c_k}{\tau_k}V_i(t)dt + \frac{1}{\tau_k}\sqrt{2\mathrm{k}_B\mathrm{T}c_k}dW_{i,k}(t) \tag{10c}$$

It is for this system of equations that we will construct a numerical integration scheme in Section II C.

It is worth noting that other authors have rigorously shown that this extended variable form of the GLE converges to the Langevin equation in the limit of small τ_k.[36] Informally, this can be seen by multplying the $S_{i,k}$ equation by τ_k, and taking the limit as τ_k goes to zero, which results in

$$S_{i,k}(t)dt = -c_k V_i(t)dt + \sqrt{2\mathrm{k}_B\mathrm{T}c_k}dW_{i,k}(t).$$

Inserting this expression into the equation for V_i, we obtain

$$m_i dV_i(t) = F_i^c\left(X(t)\right)dt - \left(\sum_{k=1}^{N_k} c_k\right) V_i(t)dt + \sqrt{2\mathrm{k}_B\mathrm{T}}\sum_{k=1}^{N_k}\sqrt{c_k}dW_{i,k}(t),$$
$$dX_i(t) = V_i(t)dt,$$

which is a conventional Langevin equation. We have been careful to preserve this limit in our numerical integration scheme, and will explicitly demonstrate this theoretically and numerically.

C. Numerical Integration of the Extended GLE

We consider a family of numerical integration schemes for the system in Equation 10 assuming a uniform timestep, Δt. Notation is adopted such that $X_i(n\Delta t) = X_i^n$ for $n \in \mathbb{N}$. Given the values of X_i^n, V_i^n, and $S_{i,k}^n$, we update to the $(n+1)$th time step using the following splitting method:

1. *Advance V_i by a half step:*

$$V_i^{n+1/2} = V_i^n + \frac{\Delta t}{2m_i}F_i^c\left(X^n\right) + \frac{\Delta t}{2m_i}\sum_{k=1}^{N_k} S_{i,k}^n \tag{11}$$

2. *Advance X_i by a full step:*

$$X_i^{n+1} = X_i^n + \Delta t V_i^{n+1/2} \tag{12}$$

3. *Advance $S_{i,k}$ by a full step:*

$$S_{i,k}^{n+1} = \theta_k S_{i,k}^n - \left(1-\theta_k\right)c_k V_i^{n+1/2} + \alpha_k\sqrt{2\mathrm{k}_B\mathrm{T}c_k}B_{i,k}^n \tag{13}$$

4. *Advance V_i by a half step:*

$$V_i^{n+1} = V_i^{n+1/2} + \frac{\Delta t}{2m_i}F_i^c\left(X^{n+1}\right) + \frac{\Delta t}{2m_i}\sum_{k=1}^{N_k} S_{i,k}^{n+1} \tag{14}$$

Here, each $B_{i,k}^n$ is drawn from an independent Gaussian distribution of mean zero and variance unity. The real-valued θ_k and α_k can be varied to obtain different methods. For consistency, we require that

$$\theta_k = 1 - \frac{\Delta t}{\tau_k} + \mathcal{O}(\Delta t^2), \quad \text{and} \quad \alpha_k = \frac{\sqrt{\Delta t}}{\tau_k} + \mathcal{O}(\Delta t).$$

For the remainder of this article, we restrict our attention three different methods, each of which corresponds to a different choice for θ_k and α_k.

- **Method 1:** Using the Euler-Maruyama scheme to update $S_{i,k}$ is equivalent to using

$$\theta_k := 1 - \frac{\Delta t}{\tau_k} \quad \text{and} \quad \alpha_k := \frac{\sqrt{\Delta t}}{\tau_k}$$

- **Method 2:** If V_i is held constant, the equation for $S_{i,k}$ can be solved exactly. Using this approach is equivalent to setting

$$\theta_k := \exp(-\Delta t/\tau_k) \quad \text{and} \quad \alpha_k := \sqrt{\frac{(1-\theta_k^2)}{2\tau_k}}$$

- **Method 3:** Both methods 1 and 2 are unstable as τ_k goes to zero. To improve the stability when τ_k is small, we consider the following modified version of method 2:

$$\theta_k := \exp(-\Delta t/\tau_k) \quad \text{and} \quad \alpha_k := \sqrt{\frac{(1-\theta_k)^2}{\Delta t}}$$

Note that all three methods satisfy the consistency condition, and are equivalent to the Störmer-Verlet-leapfrog method[42] when $c_k = 0$ and $S_{i,k}(0) = 0$.

D. Error and Stability Analysis

To help guide our choice of method, we compute the moments of the stationary distribution for a one-dimensional harmonic potential (natural frequency ω) and a single mode memory kernel (weight c and time scale τ). A similar approach has been used for the classical Langevin equation.[37,43] The extended variable GLE for this system converges to a distribution of the form

$$\rho(X,V,S) = \frac{1}{Z}\exp\left[-(mV^2 + m\omega^2X^2 + \frac{\tau}{c}S^2)/2\mathrm{k}_B\mathrm{T}\right]$$

Where Z is the usual normalization constant. From this, we can derive the analytic first and second moments

$$\langle V\rangle = 0, \quad \langle X\rangle = 0, \quad \text{and} \quad \langle S\rangle = 0.$$

$$\langle XV\rangle = 0, \quad \langle VS\rangle = 0, \quad \text{and} \quad \langle XS\rangle = 0.$$

$$\langle V^2\rangle = \frac{\mathrm{k}_B\mathrm{T}}{m}, \quad \langle X^2\rangle = \frac{\mathrm{k}_B\mathrm{T}}{m\omega^2}, \quad \text{and} \quad \langle S^2\rangle = \frac{c\mathrm{k}_B\mathrm{T}}{\tau}.$$

Next, we consider the discrete-time process generated by our numerical integrators, and show that the moments of its stationary distribution converge to the analytic ones in Δt.

$$\begin{aligned}
V^{n+1/2} &= V^n - \frac{\Delta t}{2}\omega^2 X^n + \frac{\Delta t}{2m}S^n \\
X^{n+1} &= X^n + \Delta t\, V^{n+1/2} \\
S^{n+1} &= \theta\, S^n - (1-\theta)c\, V^{n+1/2} + \alpha\sqrt{2\mathrm{k}_B\mathrm{T}c}\, B^n \\
V^{n+1} &= V^{n+1/2} - \frac{\Delta t}{2}\omega^2 X^{n+1} + \frac{\Delta t}{2m}S^{n+1}
\end{aligned}$$

The stationary distribution of this process is defined by the time independence of its first moments

$$\langle X^{n+1}\rangle = \langle X^n\rangle, \quad \langle V^{n+1}\rangle = \langle V^n\rangle, \quad \text{and} \quad \langle S^{n+1}\rangle = \langle S^n\rangle$$

Enforcing these identities, it can be shown that

$$\langle V^n\rangle = 0, \quad \langle X^n\rangle = 0, \quad \text{and} \quad \langle S^n\rangle = 0.$$

Hence, the first moments are correctly computed by the numerical method for any choice of θ and α. Computing the second moments, we obtain

$$\langle X^n V^n\rangle = 0, \quad \langle V^n S^n\rangle = 0, \quad \langle X^n S^n\rangle = \frac{2\Delta t^2\alpha^2 c\,\mathrm{k}_B\mathrm{T}}{2c\Delta t(1-\theta)^2 - m(1-\theta^2)(4-(\omega\Delta t)^2)},$$

$$\langle (V^n)^2\rangle = \frac{\mathrm{k}_B\mathrm{T}}{m}\frac{\Delta t\alpha^2}{(1-\theta)^2}, \quad \langle (X^n)^2\rangle = \frac{\mathrm{k}_B\mathrm{T}}{m\omega^2}\frac{\Delta t\alpha^2(2c\Delta t(1-\theta)^2 - 4m(1-\theta^2))}{(1-\theta)^2(2c\Delta t(1-\theta)^2 - m(1-\theta^2)(4-(\omega\Delta t)^2))},$$

$$\text{and} \quad \langle (S^n)^2\rangle = \frac{c\,\mathrm{k}_B\mathrm{T}}{\tau}\frac{2\tau\alpha^2 m(4-(\omega\Delta t)^2)}{m(1-\theta^2)(4-(\omega\Delta t)^2) - 2c\Delta t(1-\theta)^2}$$

From this analysis, we conclude that we obtain the correct second moment for V for any method with $\Delta t\alpha^2 = (1-\theta)^2$. Now, applying the particular values of θ and α, and expanding in powers of Δt, we obtain the following.

- **Method 1:**

$$\langle (V^n)^2\rangle = \frac{\mathrm{k}_B\mathrm{T}}{m}, \quad \langle (X^n)^2\rangle = \frac{\mathrm{k}_B\mathrm{T}}{m\omega^2}\left(1 + \frac{(\omega\Delta t)^2}{4}\right) + \mathcal{O}(\Delta t^4),$$

$$\langle X^n S^n\rangle = \frac{\Delta t^2\, c\,\mathrm{k}_B\mathrm{T}}{4m\tau} + \mathcal{O}(\Delta t^3), \quad \text{and} \quad \langle (S^n)^2\rangle = \frac{c\,\mathrm{k}_B\mathrm{T}}{\tau}\left(1 + \frac{\Delta t}{2\tau}\right) + \mathcal{O}(\Delta t^2)$$

- **Method 2:**

$$\langle (V^n)^2\rangle = \frac{\mathrm{k}_B\mathrm{T}}{m}\left(1 + \frac{\Delta t^2}{12\tau^2}\right) + \mathcal{O}(\Delta t^4), \quad \langle (X^n)^2\rangle = \frac{\mathrm{k}_B\mathrm{T}}{m\omega^2}\left(1 + \frac{(1+3(\omega\tau)^2)\Delta t^2}{12\tau^2}\right) + \mathcal{O}(\Delta t^4),$$

$$\langle X^n S^n\rangle = \frac{\Delta t^2\, c\,\mathrm{k}_B\mathrm{T}}{4m\tau} + \mathcal{O}(\Delta t^4), \quad \text{and} \quad \langle (S^n)^2\rangle = \frac{c\,\mathrm{k}_B\mathrm{T}}{\tau}\left(1 + \frac{c\Delta t^2}{4m\tau}\right) + \mathcal{O}(\Delta t^4)$$

- **Method 3:**

$$\langle (V^n)^2\rangle = \frac{\mathrm{k}_B\mathrm{T}}{m}, \quad \langle (X^n)^2\rangle = \frac{\mathrm{k}_B\mathrm{T}}{m\omega^2}\left(1 + \frac{(\omega\Delta t)^2}{4}\right) + \mathcal{O}(\Delta t^4),$$

$$\langle X^n S^n\rangle = \frac{\Delta t^2\, c\,\mathrm{k}_B\mathrm{T}}{4m\tau} + \mathcal{O}(\Delta t^4), \quad \text{and} \quad \langle (S^n)^2\rangle = \frac{c\,\mathrm{k}_B\mathrm{T}}{\tau}\left(1 + \frac{(3c\tau - m)\Delta t^2}{12m\tau^2}\right) + \mathcal{O}(\Delta t^4)$$

For methods 1 and 3, we obtain the exact variance for V, independent of Δt, since they both satisfy $\Delta t \alpha^2 = (1-\theta)^2$. For method 2, the error in the variance of V is second-order in Δt. All three methods overestimate the variance of X, with an error which is second-order in Δt. The error in the variance of S is first-order for method 1, and second-order for methods 2 and 3.

It is possible to choose θ and α to obtain the exact variance for X, but this would require using a different value for θ and α for each value of ω. This is not useful in our framework, since the method is applied to problems with general nonlinear interaction forces.

We would like our numerical method to be stable for a wide range of values for τ_k. As we mentioned in Section II B, the GLE converges to the conventional Langevin equation as τ_k goes to zero, and we would like our numerical method to have a similar property. For fixed Δt, both methods 1 and 2 are unstable (α_k is unbounded) as τ_k goes to zero. However, method 3 does not suffer from the same problem, with θ_k converging to zero and α_k bounded.

From this analysis, we conclude that method 3 is the best choice for implementation. Prior to providing implementation details, however, we briefly consider a simple multistage extension that can capture the exact first and second moments of position and velocity simultaneously at the expense of introducing a numerical correlation between them.

E. Multistage Splitting

Inspired by the work of Leimkuhler and Matthews,[43] we consider a generalization of the splitting method considered in Section II C in which the position and velocity updates are further split,

$$
\begin{aligned}
V_i^{n+1/4} &= V_i^n + \frac{\Delta t}{2m_i} F_i^c\left(X^n\right) + (1-\xi)\frac{\Delta t}{2m_i}\sum_{k=1}^{N_k} S_{i,k}^n \\
X_i^{n+1/2} &= X_i^n + \frac{\Delta t}{2} V_i^{n+1/4} \\
V_i^{n+1/2} &= V_i^{n+1/4} + \xi\frac{\Delta t}{2m_i}\sum_{k=1}^{N_k} S_{i,k}^n \\
S_{i,k}^{n+1} &= \theta_k S_{i,k}^n - (1-\theta_k)\, c_k V_i^{n+1/2} + \alpha_k\sqrt{2\mathrm{k_B T} c_k}\, B_{i,k}^n \\
V_i^{n+3/4} &= V_i^{n+1/2} + \xi\frac{\Delta t}{2m_i}\sum_{k=1}^{N_k} S_{i,k}^{n+1} \\
X_i^{n+1} &= X_i^{n+1/2} + \frac{\Delta t}{2} V_i^{n+3/4} \\
V_i^{n+1} &= V_i^{n+3/4} + \frac{\Delta t}{2m_i} F_i^c\left(X^{n+1}\right) + (1-\xi)\frac{\Delta t}{2m_i}\sum_{k=1}^{N_k} S_{i,k}^{n+1}
\end{aligned}
$$

In the special case that $\xi = 0$, we have $V_i^{n+1/4} = V_i^{n+1/2} = V_i^{n+3/4}$, the two updates of X can be combined, and we recover our original splitting method.

Repeating the analysis in Section II D for the harmonic oscillator with a single memory term, we find

$$\langle (V^n)^2 \rangle = \frac{\mathrm{k}_B\mathrm{T}}{m} \frac{\Delta t \alpha^2 (4 - (\Delta t\omega)^2 \xi)}{4(1-\theta)^2}, \quad \langle X^n V^n \rangle = 0, \quad \langle V^n S^n \rangle = 0,$$

$$\langle (X^n)^2 \rangle = \frac{\mathrm{k}_B\mathrm{T}}{m\omega^2} \frac{\Delta t \alpha^2 (c\Delta t(1-\theta)^2(4-(\omega\Delta t)^2\xi^2) - 2m(1-\theta^2)(4-(\omega\Delta t)^2\xi))}{(1-\theta)^2(c\Delta t(1-\theta)^2(4-(\omega\Delta t)^2\xi) - 2m(1-\theta^2)(4-(\omega\Delta t)^2))},$$

$$\langle X^n S^n \rangle = \frac{4\Delta t^2 \alpha^2 (1-\xi) c\,\mathrm{k}_B\mathrm{T}}{c\Delta t(1-\theta)^2(4-(\omega\Delta t)^2\xi) - 2m(1-\theta^2)(4-(\omega\Delta t)^2)},$$

$$\text{and} \quad \langle (S^n)^2 \rangle = \frac{c\,\mathrm{k}_B\mathrm{T}}{\tau} \frac{4\tau\alpha^2 m(4-(\omega\Delta t)^2)}{2m(1-\theta^2)(4-(\omega\Delta t)^2) - c\Delta t(1-\theta)^2(4-(\omega\Delta t)^2\xi)}.$$

In the special case that $\xi = 1$, we can simplify these expressions to obtain

$$\langle (V^n)^2 \rangle = \frac{\mathrm{k}_B\mathrm{T}}{m} \frac{\Delta t \alpha^2 (4 - (\Delta t\omega)^2)}{4(1-\theta)^2}, \qquad \langle (X^n)^2 \rangle = \frac{\mathrm{k}_B\mathrm{T}}{m\omega^2} \frac{\Delta t \alpha^2}{(1-\theta)^2}, \quad \langle X^n V^n \rangle = 0,$$

$$\langle X^n S^n \rangle = 0, \quad \langle V^n S^n \rangle = 0, \quad \text{and} \quad \langle (S^n)^2 \rangle = \frac{c\,\mathrm{k}_B\mathrm{T}}{\tau} \frac{4\tau\alpha^2 m}{2m(1-\theta^2) - c\Delta t(1-\theta)^2}.$$

From this analysis, we conclude that we obtain the correct second moment for X for any method with $\xi = 1$ and $\Delta t\alpha^2 = (1-\theta)^2$. To guarantee the correct second moment for V, the choice of θ and α becomes ω dependent. As was discussed in the previous section, the parameters prescribed by methods 1 and 3 using the original splitting have a similar behavior but with the roles of X and V reversed.

It is then tempting to formulate a method that exactly preserves the second moments of both X and V at the same time. It turns out that this is possible by simply shifting where we observe V, using either $V_i^{n+1/4}$ or $V_i^{n+3/4}$ in the multistage splitting method above. For example, consider the following asymmetric method, with $\xi = 1$,

$$\begin{aligned}
X_i^{n+1/2} &= X_i^n + \frac{\Delta t}{2} V_i^n \\
V_i^{n+1/2} &= V_i^n + \frac{\Delta t}{2m_i} \sum_{k=1}^{N_k} S_{i,k}^n \\
S_{i,k}^{n+1} &= \theta_k S_{i,k}^n - (1-\theta_k)\, c_k V_i^{n+1/2} + \alpha_k \sqrt{2\mathrm{k}_B\mathrm{T} c_k} B_{i,k}^n \\
V_i^{n+3/4} &= V_i^{n+1/2} + \frac{\Delta t}{2m_i} \sum_{k=1}^{N_k} S_{i,k}^{n+1} \\
X_i^{n+1} &= X_i^{n+1/2} + \frac{\Delta t}{2} V_i^{n+3/4} \\
V_i^{n+1} &= V_i^{n+3/4} + \frac{\Delta t}{m_i} F_i^c\left(X^{n+1}\right)
\end{aligned}$$

For this method we obtain,

$$\langle (V^n)^2 \rangle = \frac{\mathrm{k}_B\mathrm{T}}{m}\frac{\Delta t\alpha^2}{(1-\theta)^2}, \qquad \langle (X^n)^2 \rangle = \frac{\mathrm{k}_B\mathrm{T}}{m\omega^2}\frac{\Delta t\alpha^2}{(1-\theta)^2}, \quad \langle X^n V^n \rangle = \frac{-\Delta t^2\alpha^2\mathrm{k}_B\mathrm{T}}{2m(1-\theta)^2},$$

$$\langle X^n S^n \rangle = 0, \quad \langle V^n S^n \rangle = 0, \quad \text{and} \quad \langle (S^n)^2 \rangle = \frac{c\,\mathrm{k}_B\mathrm{T}}{\tau}\frac{4\tau\alpha^2 m}{2m(1-\theta^2) - c\Delta t(1-\theta)^2}.$$

If we use a method with $\Delta t\alpha^2 = (1-\theta)^2$, we find that we obtain the exact moments for X and V, but we have introduced an $\mathcal{O}(\Delta t)$ correlation between X and V. This is in contrast to the symmetric methods where this correlation is identically zero.

III. IMPLEMENTATION DETAILS

Method 3, as detailed in Section II D has been implemented in the LAMMPS software package. It can be applied in conjunction with all conservative force fields supported by LAMMPS. There are a number of details of our implementation worth remarking on concerning random number generation, initial conditions on the extended variables, and the conservation of total linear momentum.

The numerical integration scheme requires the generation of Gaussian random numbers, by way of $B^n_{i,k}$ in Equation 13. By default, all random numbers are drawn from a uniform distribution with the same mean and variance as the formally required Gaussian distribution. This distribution is chosen to avoid the generation of numbers that are arbitrarily large, or more accurately, arbitrarily close to the floating point limit. The generation of such large numbers may lead to rare motions that result in the loss of atoms from a periodic simulation box, even at low temperatures. Atom loss occurs if, within a single time step, the change in one or more of an atom's position coordinates is updated to a value that results in it being placed outside of the simulation box after periodic boundary conditions are applied. A uniform distribution can be used to guarantee that this will not happen for a given temperature and time step. However, for the sake of mathematical rigor, the option remains at compile-time to enable the use of the proper Gaussian distribution with the caveat that such spurious motions may occur. Should the use of this random number generator produce a trajectory in which atom loss occurs, a simple practical correction may be to use a different seed and/or a different time step in a subsequent simulation. It is worth noting that the choice of a uniform random number distribution has been rigorously justified by Dünweg and Paul[44] for a number of canonical random processes, including one described by a conventional Langevin equation. We anticipate that a similar result may hold for the extended variable GLE presented in this manuscript.

With respect to the initialization of the extended variables, it is frequently the case in MD that initial conditions are drawn from the equilibrium distribution at some initial temperature. Details of the equilibrium distribution for the extended system are presented in Section 2 of an article by Ottobre and Pavliotis.[36] In our implementation, we provide the option to initialize the extended variables either based upon this distribution, or with zero initial conditions (i.e., the extended system at zero temperature). As it is typically more relevant for MD simulations, the former is enabled by default and used in the generation of the results in this paper.

Conservation of the total linear momentum of a system is frequently a desirable feature for MD trajectories. For deterministic forces, this can be guaranteed to high precision through the subtraction of the velocity of the center of mass from all particles at a single time step. In the presence of random forces such as those arising in GLD, a similar adjustment must be made at each time step to prevent the center of mass from undergoing a random acceleration. While it is not enabled by default, our implementation provides such a mechanism that can be activated. When active, the average of the forces acting on all extended variables is subtracted from each individual extended variable at each time step. While this is a computationally inexpensive adjustment, it may not be essential for all simulations.

IV. RESULTS

Throughout this section, results will be presented, primarily in terms of the integrated velocity autocorrelation function (VAF). This quantity is calculated using "block averaging" and "subsampling" of the integrated trajectories for computational convenience.[45] Error bars are derived from the standard deviation associated with a set of independently generated trajectories.

We begin by presenting results that validate our time integration scheme for a GLE in the absence of a conservative force with a single mode Prony series kernel. In this case, the GLE is analytically soluble.[46] We consider the normalized VAF as a metric for comparison. For a kernel of the form

$$\Gamma(t) = \frac{c}{\tau} \exp\left[\frac{-t}{\tau}\right], \quad t \geq 0, \tag{15}$$

the normalized VAF takes the following form:

$$\frac{\langle V(t)V(0)\rangle}{\langle V(0)V(0)\rangle} = \begin{cases} \exp\left[\frac{-t}{2\tau}\right]\left(\cos(\Omega t) + \frac{1}{2\tau\Omega}\sin(\Omega t)\right) & \text{for } \Omega \neq 0 \\ \exp\left[\frac{-t}{2\tau}\right]\left(1 + \frac{t}{2\tau}\right) & \text{for } \Omega = 0 \end{cases}, \quad \Omega = \sqrt{c/\tau - 1/4\tau^2}. \tag{16}$$

Making an analogy with the canonical damped harmonic oscillator, we consider three scenarios, i.

underdamped (real Ω), ii. critically damped ($\Omega = 0$), and iii. overdamped (imaginary Ω). In Figure 1, we demonstrate that we can recover all three regimes using our integrator.

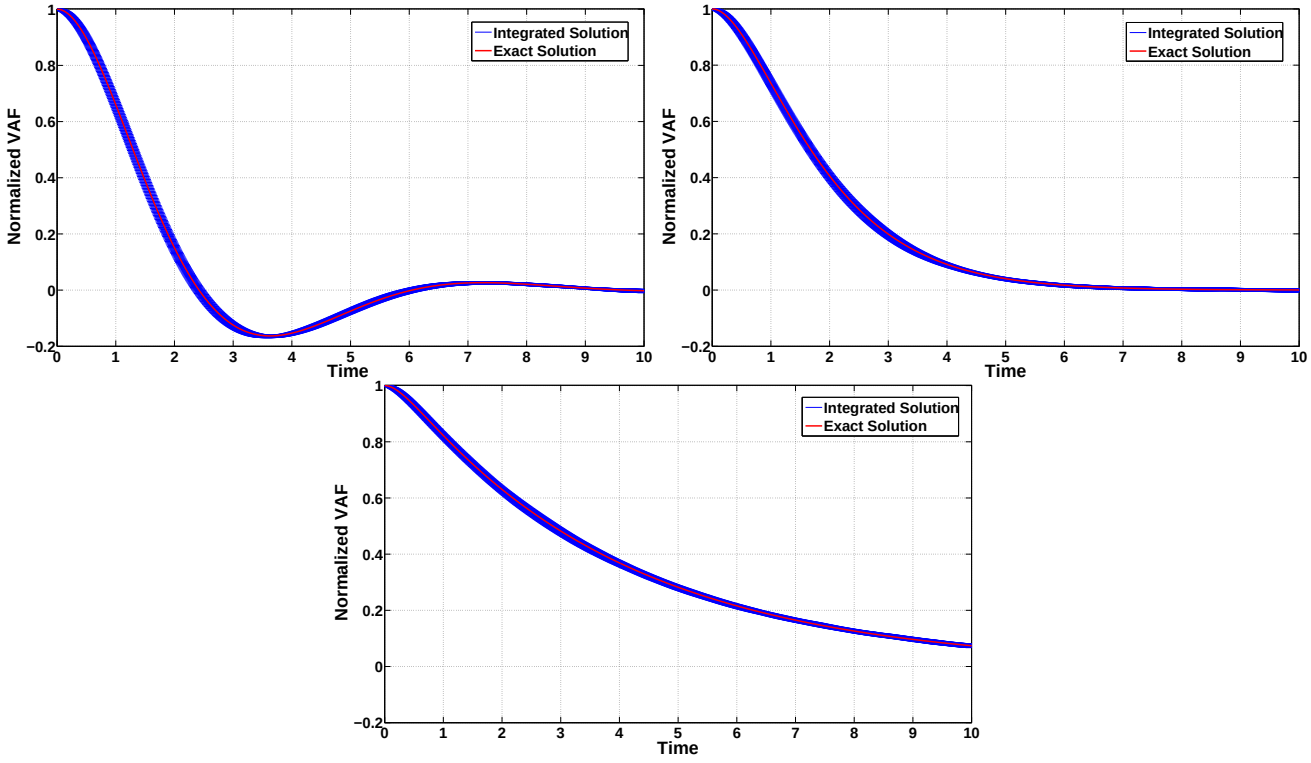

FIG. 1. Normalized VAF for a single Prony series mode in the i.) underdamped ($c = 1$, $\tau = 1$), ii.) critically damped ($c = 0.5$, $\tau = 0.5$), and iii.) overdamped limits ($c = 0.25$, $\tau = 0.25$). A time step of $\Delta t = 0.01$ is used for all runs, and error bars are drawn based upon a sample of 10,000 walkers over 10 independent runs.

To validate our integration scheme in the presence of a conservative force, we next consider GLD with an external potential. The analytic solution of the GLE with a power law memory kernel and a harmonic confining potential has been derived by other authors.[33] In the cited work, the GLE is solved in the Laplace domain, yielding correlation functions given in terms of a series of Mittag-Leffler functions and their derivatives. Here, we apply our integration scheme to a Prony series fit of the power law kernel and demonstrate that our results are in good agreement with the exact result over a finite time interval. The GLE that we intend to model has the form:

$$dV(t) = -\omega_0^2 X(t)dt - \int_0^t \frac{\gamma_\lambda}{\Gamma(1-\lambda)}(t-s)^{-\lambda}V(s)dsdt + M^{-1}F^r(t)dt, \quad 0 < \lambda < 1 \tag{17}$$

We begin by constructing a Prony series representation of the memory kernel. As it exhibits a power law decay in the Laplace domain, as well, a Prony series representation will have strong

contributions from modes decaying over a continuum of time scales. To this end, rather than relying on a non-linear fitting procedure to choose values for τ_k, we assume logarithmically spaced values from $\Delta t/10$ to $10N_t\Delta t$. By assuming the form of each exponential, the Prony series fit reduces to a simple linear least squares problem, that we solve using uniformly spaced data over an interval that is two decades longer than the actual simulation. In Figure 2, the Prony series fit of the memory kernel for $\lambda = 0.5$ is compared to its exact value.

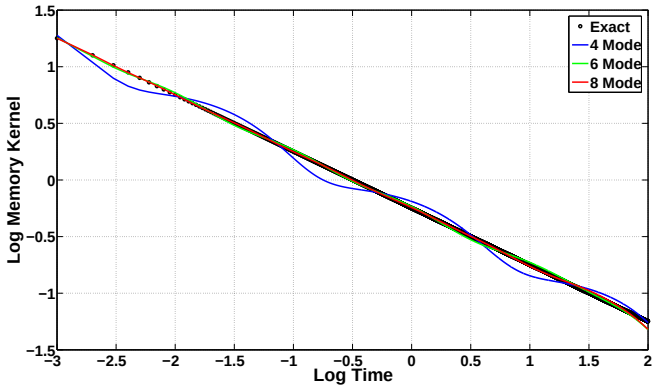

FIG. 2. A Prony series fit of the power law memory kernel in Equation 17 for $\gamma_\lambda = 1$, $\lambda = 0.5$ with an increasing number of modes.

Here, the maximum relative error is $\sim 10\%$, while it is $\sim 1\%$ for $N_k = 8$. In Figure 3, the normalized VAF computed via numerical integration of the extended GLE with a variable number of modes is shown compared to the exact result for some of the parameters utilized in an article by Despósito and Viñales.[33] It seems evident that the accuracy of the integrated velocity distribution improves relative to the exact velocity distribution as the number of terms in the Prony series fit increases. This is quantified in Figure 4, in which the pointwise absolute error in the integrated VAF is illustrated.

Next, we demonstrate that our implementation is robust in certain limits of the GLE - particularly the Langevin and zero coefficient limits. As our implementation is available in a public domain code with a large user base, developing a numerical method that is robust to a wide array of inputs is essential. For the zero coefficient limit we consider a harmonically confined particle experiencing a single mode Prony series memory kernel of the following form:

$$dV(t) = -\omega_0^2 X(t)dt - \int_0^t \frac{c}{\tau} e^{-(t-s)/\tau} V(s)dsdt + M^{-1}F^r(t)dt, \quad 0 < \lambda < 1 \tag{18}$$

The initial conditions on X and V are drawn from a thermal distribution at $T = 1$. In the limit that $c \to 0$, we expect the integrated normalized VAF to approach that of a set of deterministic

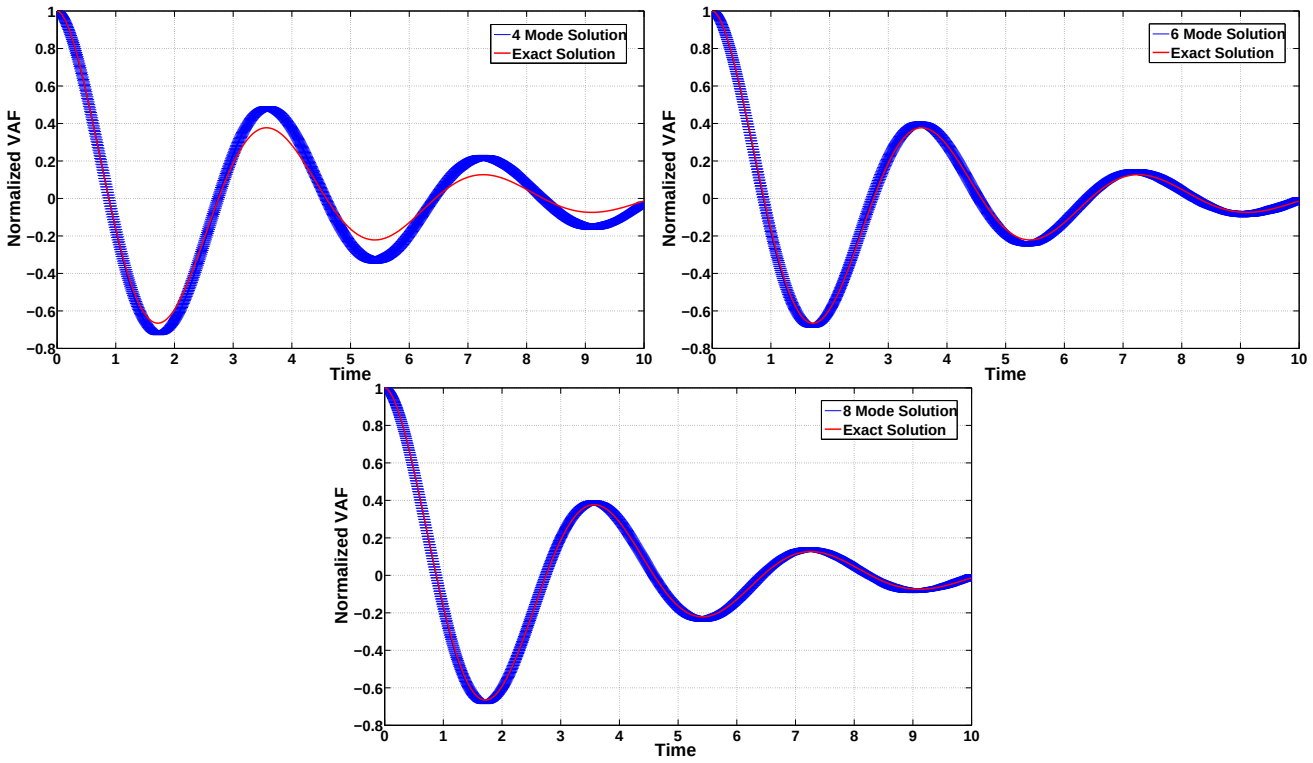

FIG. 3. Comparison of numerically integrated results to the exact solution of Equation 17 for $\gamma_\lambda = 1$, $\lambda = 0.5$, and $\omega_0 = 1.4$. A time step of $\Delta t = 0.01$ is used, and error bars are drawn based upon a sample of 10,000 walkers over 10 independent runs with $\Delta t = 0.01$.

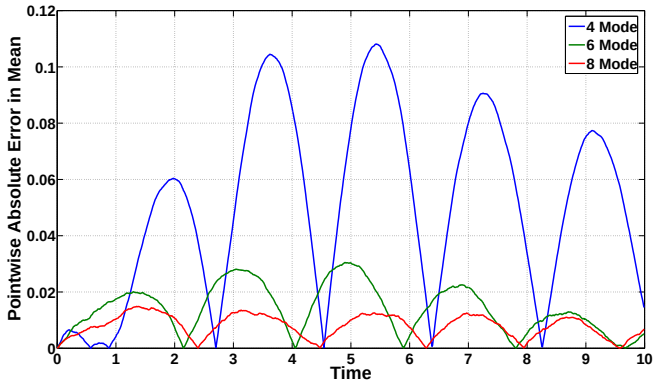

FIG. 4. Pointwise absolute error in the normalized velocity autocorrelation function for the same conditions as Figure 3. Error is computed with respect to the mean of VAFs computed from 10 independent runs.

harmonic oscillators. The initial conditions on X and V are drawn from a thermal distribution at $T = 1$, giving the integrated result some variance, even in the Newtonian/deterministic limit. In Figure 5, that this limit is smoothly and stably approached is illustrated.

In the exact $c = 0$ limit, oscillations in the VAF occur at the natural frequency of the confining

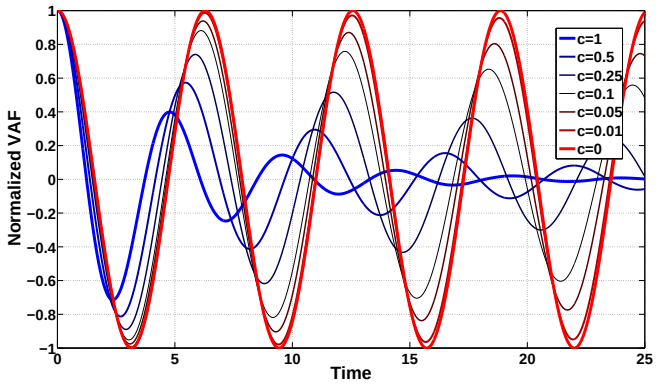

FIG. 5. Illustration of the smooth/stable manner in which the proposed integrator approaches the $c = 0$ (Newtonian) limit from $c = 1$ for a single Prony mode with $\tau = 1$. The particle is harmonically confined with $\omega_0 = 1$, and the expected period of oscillation is restored for $c = 0$.

potential, $\omega_0 = 1$, whereas for non-zero c, these oscillations are damped in proportion to c, as one may expect on the basis of intuition. The Langevin limit is illustrated next. To this end, we utilize the same single mode Prony series memory kernel, but remove the confining potential (i.e., $\omega_0 = 0$). We have done so to ensure that the Langevin limit yields an Ornstein-Uhlenbeck process. In Figure 6, we illustrate that this limit is also smoothly and stably approached.

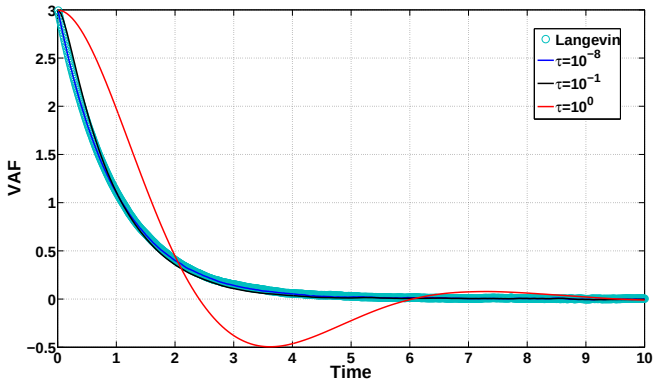

FIG. 6. Illustration of the smooth/stable manner in which the proposed integrator approaches the $\tau = 0$ (Langevin) limit from $\tau = 1$ for a single Prony mode. The particle is subject to no conservative forces, so the resultant dynamics correspond to an Ornstein-Uhlenbeck process. The 'exact' Langevin limit was integrated using *fix langevin* in LAMMPS.

The result for the Langevin limit itself was integrated using the existing *fix langevin* command in LAMMPS. For $\tau = 10^0$, the GLE yields results that differ from the Langevin limit as one might expect on the basis of the previous results. However, even for $\tau = 10^{-1}$, the GLE yields results that are close to that of the Langevin limit, as the resultant numerical method retains some GLE-like

behavior. However, for $\tau = 10^{-8}$ and $\Delta t = 0.01$, the parameter $\theta = \exp[-10^6]$, is below machine epsilon. As mentioned in Section II D, this results in a method that is indistinguishable from conventional Langevin dynamics, and consequently, the integrated dynamics are indistinguishable. This result demonstrates that the method is robust, even if the user 'accidentally' crosses into a Langevin-like regime. We again emphasize that methods 1 and 2, considered earlier, will not stably approach this limit.

To demonstrate capability in reduced order modeling, we next invert the VAF associated with a set of trajectories generated in the presence of a conservative force, to construct a memory kernel that will reproduce the same dynamics without such a force. In other words, we seek an effective memory kernel, $\Gamma_{eff}(t)$, such that a simplified GLE of the form:

$$dV(t) = -\int_0^t \Gamma_{eff}(t-s)V(s)dsdt + M^{-1}F^r(t)dt \tag{19}$$

reproduces the VAF of a GLE of the more general form given in Equation 1.

The starting point for this procedure is the observation that for Equation 19, the VAF and memory kernel have the following relationship in the Laplace domain:[13]

$$\langle \widetilde{V}(\sigma)V(0)\rangle = \frac{\mathrm{k}_B\mathrm{T}}{m\sigma + \widetilde{\Gamma}_{eff}(\sigma)}. \tag{20}$$

Here, tildes indicate that the associated time domain quantities have been Laplace transformed, with transform domain variable σ. Given $\langle \widetilde{V}(\sigma)V(0)\rangle$ for some process whose VAF we wish to reproduce via integration of Equation 19, $\widetilde{\Gamma}_{eff}(\sigma)$ can be resolved algebraically, and its time domain form can be found via an inverse Laplace transform:

$$\Gamma_{eff}(t) = \mathcal{L}^{-1}\left\{\frac{\mathrm{k}_B\mathrm{T}}{\langle \widetilde{V}(\sigma)V(0)\rangle} - m\sigma\right\}(t) \tag{21}$$

This effective memory kernel can then be fit to a Prony series, and Equation 19 can be integrated using the numerical method developed in this manuscript. In Figure 7, we demonstrate that we can use this inversion procedure to take the exact VAF generated by Equation 17, and compute a $\Gamma_{eff}(t)$ for Equation 19 that reproduces it:

Here, the parameters utilized in Equation 17 were $\omega_0 = 0.5$ and $\lambda = 0.9$, and the associated analytic VAF was fit to a three term Prony series. This initial fit was done to realize a simpler form of the Laplace domain VAF, which was inserted into Equation 21. The resultant $\Gamma_{eff}(t)$ was also fit to a three term Prony series. It is interesting to note that one term of this fit reduced to a conventional Langevin term (i.e., one that was proportional to $\delta(t)$ rather than $\exp[-t/\tau]$)

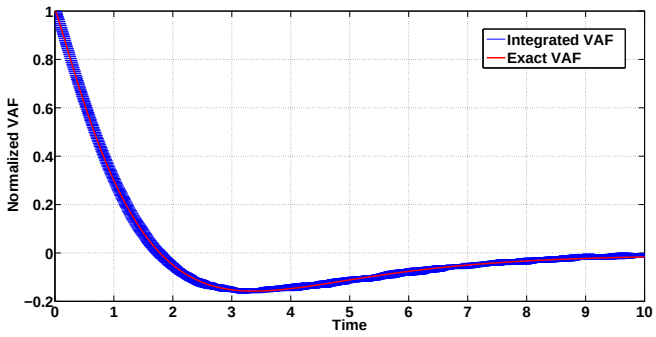

FIG. 7. Illustration of the result of the kernel fitting procedure described in Section IV. Note that while the exact VAF evolves under the influence of a harmonic confining potential (Equation 17), the integrated VAF is spawned by a GLE free of any conservative forces (Equation 19). The effect of the force is included in the construction of $\Gamma_{eff}(t)$.

highlighting the utility of our method's reproduction of the Langevin limit. This Prony series representation of $\Gamma_{eff}(t)$ was used in Equation 19, which was numerically integrated to yield the integrated VAF result in Figure 7.

This result is especially interesting as it demonstrates capability for effecting a confining potential, on a finite timescale, exclusively through the GLE drag/random forces. This same fitting procedure could be used to remove inter-particle interactions, albeit with some loss of dynamical information, and will be discussed in more detail in future work.

It is important to note that while the dynamics of a confined particle are reproduced in the absence of an explicit confining force, this is only the case over the interval for which the memory kernel is reconstructed. Outside of this interval, the asymptotic behavior of the Prony series memory kernel will give rise to unbounded diffusive motion. While the expected discrepancies in the dynamics are difficult to notice in the VAF, as both the analytic and reconstructed quantities decay to zero, it is very evident in the mean-squared displacement (MSD). Here the asymptotic exponential behavior of the Prony series memory kernel necessarily leads to asymptotic diffusive motion signaled by a linear MSD. In contrast, the analytic memory kernel with the confining force will generate an MSD that remains bounded. This is illustrated in Figure 8. Here, the fit VAF is integrated to yield the MSD for the Prony series model, and compared with the exact MSD over both the interval of the fit, and beyond. This example illustrates the importance of choosing an appropriate interval for fitting memory kernels to achieve the appropriate limiting behavior in one's dynamics.

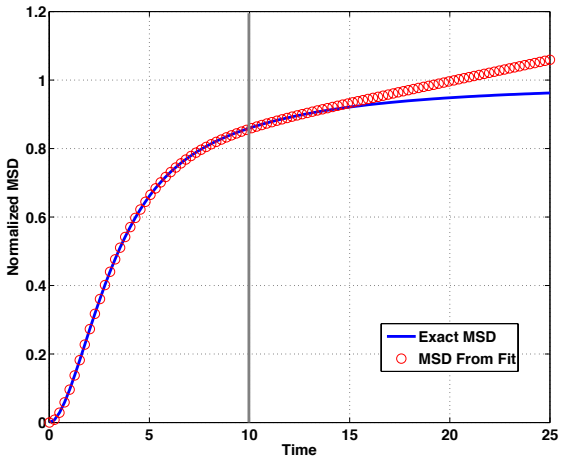

FIG. 8. Comparison of the exact normalized MSD and the MSD generated from integrating the VAF fit. The exact MSD is normalized such that its asymptotic limit is 1, and the same normalization is applied to the MSD integrated from the fit. The grey line indicates the upper bound of the interval over which the VAF fit was constructed.

V. CONCLUSIONS

A family of numerical integration schemes for GLD have been presented. These schemes are based upon an extended variable formulation of the GLE in which the memory kernel is rendered as a positive Prony series. In certain limits, it can be shown that a specific instance of this family of integrators exactly conserves the first and second moments of the integrated velocity distribution, and stably approaches the Langevin limit. To this end, we identify this parametrization as optimal, and have implemented it in the MD code, LAMMPS. Numerical experiments indicate that this implementation is robust for a number of canonical problems, as well as certain pathologies in the memory kernel. An exemplary application to reduced order modeling illustrates potential uses of this module for MD practitioners. Future work will further develop the VAF fitting procedure in the context of statistical inference methods, and present extensions of the numerical integrator to mixed sign and complex memory kernels.

VI. ACKNOWLEDGEMENTS

The authors would like to acknowledge Jason Bernstein, Paul Crozier, John Fricks, Jeremy Lechman, Rich Lehoucq, Scott McKinley, and Steve Plimpton for numerous fruitful discussions and feedback. Sandia National Laboratories is a multi-program laboratory managed and operated by Sandia

Corporation, a wholly owned subsidiary of Lockheed Martin Corporation, for the U.S. Department of Energys National Nuclear Security Administration under contract DE-AC04-94AL85000.

REFERENCES

[1]W. T. Coffey, Y. P. Kalmykov, and J. T. Waldron, *The Langevin Equation With Applications to Stochastic Problems in Physics, Chemistry, and Electrical Engineering* (World Scientific, 2004)

[2]G. E. Uhlenbeck and L. S. Ornstein, Phys. Rev. **36**, 823 (1930)

[3]R. Kubo, Rep. Prog. Phys. **29**, 255 (1966)

[4]D. L. Ermak and J. A. McCammon, J. Chem. Phys. **69**, 1352 (1978)

[5]T. Schneider and E. Stoll, Phys. Rev. B **17**, 1302 (1978)

[6]J. A. Izaguirre, D. P. Caterello, J. M. Wozniak, and R. D. Skeel, J. Chem. Phys. **114**, 2090 (2001)

[7]H. Mori, Prog. Theo. Phys. **33**, 423 (1965)

[8]J. Doll and D. Dion, J. Chem. Phys. **65**, 3762 (1976)

[9]M. Shugard, J. Tully, and A. Nitzan, J. Chem. Phys. **66**, 2534 (1977)

[10]S. Toxvaerd, J. Chem. Phys. **86**, 3667 (1987)

[11]K. Schweizer, J. Chem. Phys. **91**, 5802 (1989)

[12]T. G. Mason and D. A. Weitz, Phys. Rev. Lett. **74**, 1250 (1995)

[13]T. G. Mason, H. Gang, and D. A. Weitz, J. Opt. Soc. Am. A **14**, 139 (1997)

[14]J. Fricks, L. Yao, T. C. Elston, and M. G. Forest, SIAM J. Appl. Math. **69**, 1277 (2009)

[15]G. Didier, S. A. McKinley, D. B. Hill, and J. Fricks, J. Time Series Analysis **33**, 724 (2012)

[16]S. C. Kou and X. S. Xie, Phys. Rev. Lett. **93**, 180603 (2004)

[17]W. Min, G. Luo, B. J. Cherayil, S. C. Kou, and X. S. Xie, Phys. Rev. Lett. **94**, 198302 (2005)

[18]D. Gordon, V. Krishnamurthy, and S. Chung, J. Chem. Phys. **131**, 134102 (2009)

[19]M. Ceriotti, G. Bussi, and M. Parrinello, Phys. Rev. Lett. **102**, 020601 (2009)

[20]M. Ceriotti, G. Bussi, and M. Parrinello, Phys. Rev. Lett. **103**, 030603 (2009)

[21]M. Ceriotti and D.E.. Manolopoulos, Phys. Rev. Lett. **109**, 100604 (2012)

[22]I. Sokolov, Soft Matter **8**, 9043 (2012)

[23]G. Ciccotti and J. Ryckaert, Mol. Phys. **40**, 141 (1980)

[24]M. Berkowitz, J. Morgan, and J. McCammon, J. Chem. Phys. **78**, 3256 (1983)

[25]E. Guàrdia and J. Padró, J. Chem. Phys. **83**, 1917 (1985)

[26]J. Straub, M. Borkovec, and B. Berne, J. Chem. Phys. **84**, 1788 (1986)

[27]D. Smith and C. Harris, J. Chem. Phys. **92**, 1304 (1990)

[28]L. Nilsson and J. Padró, Mol. Phys. **71**, 355 (1990)

[29]S. Wan, C. Wang, and Y. Shi, Mol. Phys. **93**, 901 (1998)

[30]D. Gordon, V. Krishnamurthy, and S. Chung, Mol. Phys. **106**, 1353 (2008)

[31]S. Plimpton, J. Comp. Phys. **117**, 1 (1995), available at http://lammps.sandia.gov

[32]P. in 't Veld, S.J. Plimpton, and G.S. Grest, Comp. Phys. Comm. **179**, 320 (2008)

[33]M. A. Despósito and A. D. Viñales, Phys. Rev. E **80**, 021111 (2009)

[34]A. D. Viñales and M. A. Despósito, Phys. Rev. E **73**, 016111 (2006)

[35]S. McKinley, L. Yao, and F. Gregory, J. Rheology **53**, 1487 (2009)

[36]M. Ottobre and G. A. Pavliotis, Nonlinearity **24**, 1629 (2011)

[37]W. Wang and R. D. Skeel, Molecular Physics **101**, 2149 (2003)

[38]H. B. Callen and T. A. Welton, Phys. Rev **83**, 34 (1951)

[39]H. Mori, Prog. Theo. Phys. **34**, 399 (1965)

[40]R. Kupferman, J. Stat. Phys. **114**, 291 (2004)

[41]P. E. Kloeden and E. Platen, *Numerical Solution of Stochastic Differential Equations* (Springer, 1999)

[42]E. Hairer, C. Lubich, and G. Wanner, Acta Numerica **12**, 399 (2003)

[43]B. Leimkuhler and C. Matthews, Applied Mathematics Research eXpress **2013**, 34 (2013)

[44]B. Dünweg and W. Paul, International Journal of Modern Physics C **2**, 817 (1991)

[45]M. Allen and D. Tildesley, *Computer Simulation of Liquids* (Oxford University Press, 1987)

[46]B. J. Berne, J. P. Boon, and S. A. Rice, J. Chem. Phys. **45**, 1086 (1966)

Appendix B

B.0.1 An Approximation for a Slowly-Varying Field

In this we derive the equilibrium condition for a system of particles in a slowly varying field c.f. [**?**]. In what follows below we will distinguish between the fluid viewed as pure fluid, and the fluid considered as a binary mixture of two labeled species, A and B. To denote the latter we will explicitly use subscripts (i, A, or B, as appropriate) to indicate a density or (total or excess) chemical potential of a certain species. If no subscripts are present, we refer to a property of the pure fluid.

We start with the PDT in equation 3.0.22,

$$\begin{aligned} \beta\mu &= ln\rho(\mathbf{r}) - ln < e^{-\beta(U_t(\mathbf{r})} > + V_{ext}(\mathbf{r}) && \text{(B.0.1)} \\ &\equiv ln\rho(\mathbf{r}) + \beta\tilde{\mu}^{ex}(\mathbf{r}) + V_{ext}(\mathbf{r}) && \text{(B.0.2)} \end{aligned}$$

where we have simplified the notation by writing $\tilde{\mu}^{ex}(\mathbf{r})$ for the test-particle insertion term. This notation is suggested by the observation that in the absence of an external field that term becomes indeed the excess chemical potential. However, at this stage we are merely simplifying the notion, and the last line of equation B.0.2 simply defines the meaning of $\mu^{ex}(\mathbf{r})$. Specializing to an external field that just varies in the z-direction

$$\beta\mu = ln\rho(z) + \beta\tilde{\mu}^{ex}(z) + V_{ext}(z) \qquad \text{(B.0.3)}$$

If the local density is slowly varying, i.e., if the gradient of $\rho(z)$ is small, we can use the approximation,

$$\beta\tilde{\mu}^{ex}(z) \approx \beta\mu^{ex}(\rho(z)) \qquad \text{(B.0.4)}$$

That, is the test-particle insertion term is approximated by the bulk excess chemical potential of a fluid with a bulk density equal to the local density at position z, $\rho(z)$). Thus,

$$\beta\mu \approx ln\rho(z) + \beta\mu^{ex}(\rho(z)) + V_{ext}(z) \qquad \text{(B.0.5)}$$

The constancy of μ at equilibrium implies

$$\begin{aligned}
0 &= \frac{\partial ln\rho(z)}{\partial z} + \frac{\partial \beta\mu^{ex}(\rho(z))}{\partial z} - F_{ext}(z) \\
&= \frac{\partial ln\rho(z)}{\partial z} + \frac{\partial \beta\mu^{ex}(\rho(z))}{\partial \rho(z)}\frac{\partial \rho(z)}{\partial z} - F_{ext}(z) \\
&= \frac{\partial ln\rho(z)}{\partial z} + \frac{1}{\rho(z)}\frac{\partial \beta p^{ex}(\rho(z))}{\partial \rho(z)}\frac{\partial \rho(z)}{\partial z} - F_{ext}(z) \\
&= \frac{\partial ln\rho(z)}{\partial z}\left(1 + \frac{\partial \beta p^{ex}(\rho(z))}{\partial \rho(z)}\right) - F_{ext}(z) \\
&= \frac{\partial ln\rho(z)}{\partial z}\frac{\partial \beta p(\rho(z))}{\partial \rho(z)} - F_{ext}(z) \qquad \text{(B.0.6)}
\end{aligned}$$

where F_{ext} denotes the gradient of the one-body external field V_{ext}. Examples of the applicability of the above equation include a fluid, or a Brownian suspension in a gravitational field. Equation B.0.6 is equation (7.70) of Dhont's monograph [**?**].

If the local density gradient is not sufficiently small it may be beneficial to define a coarse-grained or weighted density, $\bar{\rho}(z)$, and the modified expression for equilibrium becomes

$$0 = \frac{\partial ln\rho(z)}{\partial z}\frac{\partial \beta p(\bar{\rho}(z))}{\partial \bar{\rho}(z)}\frac{\partial \bar{\rho}(z)}{\partial \rho(z)} - F_{ext}(z) \qquad \text{(B.0.7)}$$

To make contact with our earlier expression, we turn to the color diffusion problem. The equilibrium condition for species i is, or a slowly varying density profile:

$$\begin{aligned}
0 &= \frac{\partial ln\rho_i(z)}{\partial z} + \frac{\partial \beta\mu^{ex}(\rho(z))}{\partial z} - F_{i,ext}(z) \quad ; i = A, B \\
&= \frac{\partial ln\rho_i(z)}{\partial z} + \frac{\partial ln\rho(z)}{\partial z}\frac{\partial \beta p^{ex}(\rho(z))}{\partial \rho(z)} - F_{i,ext}(z) \\
&= \frac{\partial ln(\rho_i(z)/\rho(z))}{\partial z} + \frac{\partial ln\rho(z)}{\partial z}\frac{\partial \beta p(\rho(z))}{\partial \rho(z)} - F_{ext}(z) \\
&= \frac{\partial lnx_i(z)}{\partial z} + \frac{\partial ln\rho(z)}{\partial z}\frac{\partial \beta p(\rho(z))}{\partial \rho(z)} - F_{ext}(z) \qquad \text{(B.0.8)}
\end{aligned}$$

We stress the distinction between ρ_i and $\rho = \rho_A + \rho_B$. Thus, the excess chemical potential term is expressed entirely in terms of the pure hard sphere profile.

In a nonequilibrium situation the imbalance in the force terms on the right hand side leads to a flux of the form;

$$j_i = -D(\rho(z,t)) \left(\frac{\partial ln\rho_i(z)}{\partial z} + \frac{\partial ln\rho(z)}{\partial z} \frac{\partial \beta p^{ex}(\rho(z))}{\partial \rho(z)} - F_{i,ext}(z) \right) \rho_i(z,t) \quad ; i = A, B \tag{B.0.9}$$

Specializing to a diffusion coefficient that is the bulk diffusion, $D(\rho_b)$, we can re-arrange this expression, as before, to give,

$$\begin{aligned} \frac{j_i}{D\rho_i} + \frac{\partial ln\rho_i(z)}{\partial z} &= \frac{\partial ln\rho(z)}{\partial z} \frac{\partial \beta p^{ex}(\rho(z))}{\partial \rho(z)} - F_{i,ext}(z) \quad ; i = A, B \\ &= \frac{\tilde{K}(z)}{kT} - F_{i,ext}(z) \quad ; i = A, B \end{aligned} \tag{B.0.10}$$

B.0.2 Color Diffusion in a Slowly-Varying External Field

Next, we will consider the problem of color diffusion in the presence of a one-body external field, e.g., gravity, that acts identically on each species. For each component (as well as for the pure system) we have the equilibrium condition

$$\beta\mu_i = ln\rho_i(z) + \beta\tilde{\mu}^{ex}(z) + V_{ext}(z) \quad ; i = A, B \tag{B.0.11}$$

Again, we stress that for our system of labeled species the configurational contribution to the chemical potential is independent of the the type of species. Taking the derivative with respect to position we have, at equilibrium,

$$0 = \frac{\partial ln\rho_i(z)}{\partial z} + \frac{\partial \beta\tilde{\mu}^{ex}(z)}{\partial z} - F_{ext}(z) \quad ; i = A, B \tag{B.0.12}$$

[As an aside: this expression also holds for the pure system, i.e. without subscripts. It lets us identify the solvation force as in the case without a slowly-varying field. In particular,

simulations show that the z-component of the solvation force (the sum of all the forces due to the surrounding fluid) is :

$$F^z_{solv}(z) = \frac{\partial ln\rho_(z)}{\partial z} - F_{ext}(z) \quad \text{(B.0.13)}$$

$$= -\frac{\partial \beta\tilde{\mu}^{ex}(z)}{\partial z} \quad \text{(B.0.14)}$$

]

Similarly, if the system is not balanced there will be a flux given by,

$$j_i = D(z)\left(\frac{\partial ln\rho_i(z)}{\partial z} + \frac{\partial \beta\tilde{\mu}^{ex}(z)}{\partial z} - F_{ext}(z)\right)\rho_i(z) \quad ; i = A, B \quad \text{(B.0.15)}$$

or

$$-\frac{j_i}{D(z)\rho_i(z)} = \left(\frac{\partial ln\rho_i(z)}{\partial z} + \frac{\partial \beta\tilde{\mu}^{ex}(z)}{\partial z} - F_{ext}(z)\right) \quad ; i = A, B$$

$$= \frac{\partial ln\rho_i(z)}{\partial z}\bigg\|_V - \frac{\partial ln\rho(z)}{\partial z}\bigg\|_V \quad ; i = A, B \quad \text{(B.0.16)}$$

where we used equation B.0.12 to express the configurational contribution in terms of the pure sphere profile. Notice that the external field has dropped out of the expression. It is interesting to note that the form of the above equation is the same as it is in the absence of the the one-body external field. However, both derivatives on the right hand side are taken for a system in an external field, V_{ext}, a fact that we have highlighted by subscripting the derivative.

The presence of the external can significantly change the density profiles. Thus, in the case of a constant force (i.e., "gravity"), F_{ext}, the profile can become quite asymmetric. Regions well away from the hard walls, exhibit a sloping profile, albeit no oscillations. In other words, although the overall pure hard sphere system is equilibrium, and hence has constant chemical potential, μ, the so-called intrinsic chemical potential varies with position z. The intrinsic chemical potential is defined as:

$$\mu_{int}(z) \equiv \mu - V_{ext}(z) \quad \text{(B.0.17)}$$

The intrinsic chemical potential is a useful concept in the presence of a *slowly* varying field. For example, the atmosphere has slowly varying properties with elevation from the Earth's surface. Specifically, in gravity the intrinsic chemical potential decreases with elevation, according to

$$\mu_{int}(z) \;=\; \mu - mg(z - z_0) \tag{B.0.18}$$

where m denotes the mass and g is the gravitational acceleration. The position z_0 is a reference position. Thus, a fluid in a gravitational field has an intrinsic chemical potential that varies linearly with distance from the reference point. Combined with a bulk equation of state that links the chemical potential with the bulk density (i.e., some relation $\mu(\rho)$), equation B.0.18 constitutes an implicit equation for the local density, $\rho(z)$.

We note that, in a situation where we have a fluid confined by two parallel hard walls in the presence of gravity, the intrinsic chemical potential is a linear function throughout the entire volume, including the inhomogeneous region.

Locally, on a length scale much smaller than the gravitational length (which is of order a kilometer), the atmosphere appears to have uniform properties. To describe that region of the atmosphere one assumes that the fluid is of one intrinsic chemical potential, $\mu_{int}(z)$ at the local z. Whereas in the absence of V_{ext}, we were able to provide an excellent description of the flux by selecting a *constant* D, one cannot expect this to hold true for the more general case. It is natural to use a D that depends on on the slowly varying density, in order to rely on a relationship for the bulk fluid, $D(\rho)$ or $D(\mu)$. We do *not* seek a $D(\rho(z))$ that depends on the local density, as that would re-create physical problems in inhomogeneous interfacial regions, with a D varying wildly and rapidly on a molecular length scale. It is, in fact, only the slowly-varying part of the density, that marks the entire profile, that we seek to capture in a density dependent D.

From the discussion above it is clear that the way in which we can best phrase this is with the help of $\mu_{int}(z)$. Namely, we propose to use $D = D(\mu_{int}(z))$. This has the desired properties, namely that when $V_{ext}(z)$ vanishes it reduces to a constant D, as before; and since, at equilibrium, $\mu_{int}(z)$ varies like $V_{ext}(z)$ (because μ is a constant), it captures the thermodynamic state of the local fluid. In fact, it is the only definition that appears to make sense.

In practice, one can use Widom's insertion method to determine $\mu_{int}(z)$ at some point z. Since we know $V_{ext}(z)$ we can then, from equation B.0.17, determine the intrinsic chemical potential at all other values of z. Alternatively, we can determine $\rho(z)$, well away from the wall, where it is slowly-varying, and use as an estimate: $\mu_{int}(z) \approx \mu(\rho(z))$, and apply a bulk equation of state (i.e., a functional relationship $\mu(\rho)$).

For sufficiently small, and slowly-varying, $V_{ext}(z)$ a profile that is fairly close to linear may result. In such a case an estimate of the variation of D over the extent of the box can be obtained from a simple fit of the smooth parts of the profile, extrapolating it toward the inhomogeneous interfacial regions.

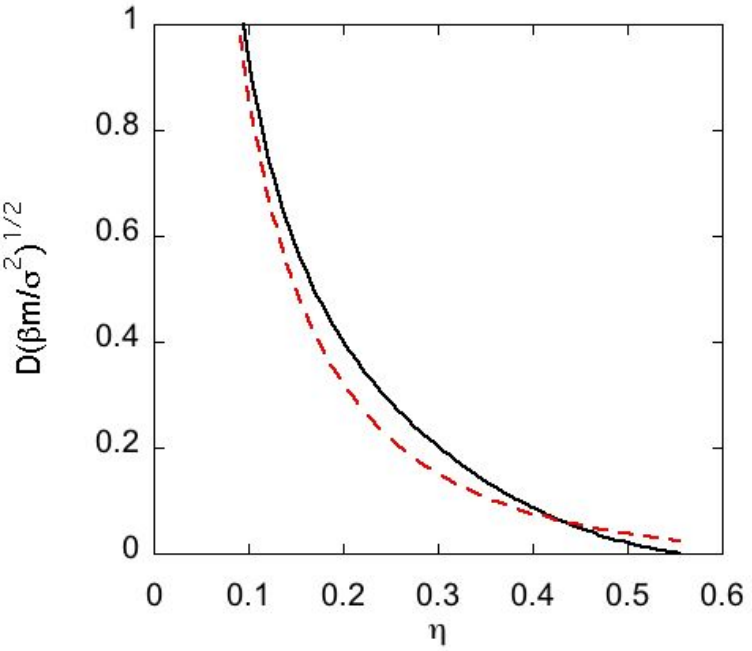

Figure B.1. The self-diffusion coefficient for hard spheres as a function of packing fraction. The solid black curve represents the fit by Heyes et al. For comparison, the Enskog approximation, which becomes exact in the low density limit, is shown as a red dashed line.

B.0.3 Color Diffusion in a Slowly-Varying External Field: an alternate derivation

As an alternative starting point we can consider Fick's first law for an ideal mixture. We recall that for our system of labeled hard spheres the local chemical potential of species i is given by (c.f. Equation 3.0.13)

$$\beta\mu_i(z) = lnx_i(z) + \beta\mu \tag{B.0.19}$$

where the mole fraction $x_i \equiv \rho_i/\rho$. This expression applies whether there is an external field or not. Hence, Fick's first law for the flux of species $i = A, B$ states that

$$j_i = -D_i(z)\rho_i\frac{\partial\beta\mu_i}{\partial z} \tag{B.0.20}$$

$$= -D_i(z)\frac{\partial\rho_i}{\partial z} - D_i\rho_i\frac{\partial ln\rho}{\partial z} \tag{B.0.21}$$

given that the total local density, ρ, is also a function of z. Note that if ρ is a constant, this equation reduces to the simplest form of Fick's first law, $j = -D\partial\rho_i/\partial z$, as it should. Equation B.0.21 applies in the inhomogeneous region caused by the presence of the hard wall, but it is also applies away from the walls if there is a slowly-varying field present.

The above equation can be rearranged to read,

$$-\frac{j_i}{D(z)\rho_i(z)} = \frac{\partial ln\rho_i(z)}{\partial z} - \frac{\partial ln\rho(z)}{\partial z} \quad ; i = A, B \tag{B.0.22}$$

which is equation B.0.16.

Equation B.0.21 can be readily used to determine the flux j_i once the steady-state profiles $\rho_i(z)$ and $\rho(z)$ are established. As discussed earlier, $D(z)$ should be approximated by $D(\mu_{int}(z))$. An example of a test of the constancy of the fluxes is shown in figure B.2 below, where we have used the data shown in figure 3.3. The onersion rate is a function of the reaction rate as well. One way to implement this is introduce a probability $p_{A\to B}$ that controls the conversion of A into B once a particle of species A hits the wall. The conversion rate (per unit area and per unit time), R, is related to the density of species A at the left hand wall by:

$$R_{AB} = p_{A\to B}\frac{\rho_A(0)}{\rho_A(0) + \rho_B(0)}c_w \tag{B.0.23}$$

$$= p_{A\to B}\frac{\rho_A(0)}{\beta p}c_w \tag{B.0.24}$$

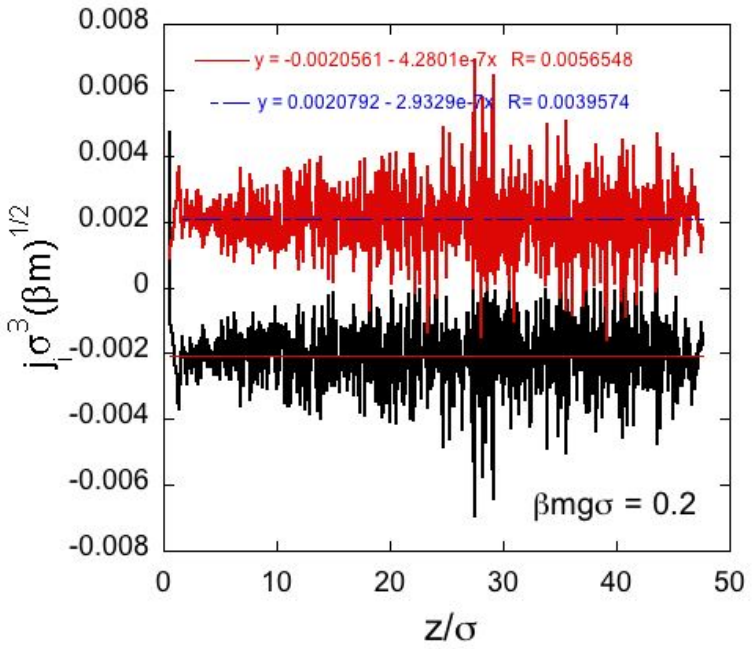

Figure B.2. The fluxes, j_A (black) and j_B (red) for a case of color diffusion between two reactive planar hard walls in the presence of gravitational field. Flux j_A is negative, as it diffuses in the negative direction (i.e., to the left), in the direction of gravity. Flux j_B is in the opposite direction, toward the righthand side wall. The strength of the constant force is given by $mg = 0.2kT/\sigma$. The data clearly shows that, although there is significant scatter, the fluxes are constant throughout the box, and the average value is in agreement with the conversion rate measured at each wall, and $j_A = -j_B$. The scatter is larger in the center of the box, as both derivatives on the right hand side of equation B.0.21 are nearly zero.

where we have used the contact theorem (that the sum of the densities at the wall equals the pressure) and that the wall collision rate per unit area is related to the collision rate by $c_w = \beta p/(2\pi)^{1/2}$.

DISTRIBUTION:

1 MS 0899 Technical Library, 9536 (electronic copy)
1 MS 0359 D. Chavez, LDRD Office, 1911

Sandia National Laboratories